2021

IMPACT OF HEMODYNAMIC VORTEX SPATIAL AND TEMPORAL CHARACTERISTICS ON ANALYSIS OF INTRACRANIAL ANEURYSMS

Kevin W. Sunderland
Michigan Technological University, kwsunder@mtu.edu

IMPACT OF HEMODYNAMIC VORTEX SPATIAL AND TEMPORAL CHARACTERISTICS ON ANALYSIS OF INTRACRANIAL ANEURYSMS

By

Kevin William Sunderland

A DISSERTATION

Submitted in partial fulfillment of the requirements for the degree of

DOCTOR OF PHILOSOPHY

In Biomedical Engineering

MICHIGAN TECHNOLOGICAL UNIVERSITY

2021

This dissertation has been approved in partial fulfillment of the requirements for the Degree of DOCTOR OF PHILOSOPHY in Biomedical Engineering.

Department of Biomedical Engineering

Dissertation Co-advisor: *Dr. Jingfeng Jiang*

Dissertation Co-advisor: *Dr. Feng Zhao*

Committee Member: *Dr. Sean Krikpatrick*

Committee Member: *Dr. Gowtham Shankara*

Committee Member: *Dr. Min Wang*

Department Chair: *Dr. Sean Kirkpatrick*

Contents

List of Figures

List of Tables

Preface

The proceeding dissertation is composed of my research to acheive a PhD degree in Biomedical Engineering at Michigan Technological University. Chapters 2, 3, 4, and 5 have been published previously. Research work in chapters 2-5 in this dissertation were overseen by Dr. Jingfeng Jiang, while the work in chapter 6 was overseen by Dr. Feng Zhao. The majority of the materials presented in Chapter 2 are reproduced from a previously published article in Computational and Mathematical Models in Medicine by the Hindawi Publishing Corporation [319]: Copyright © 2016 Kevin Sunderland et al. Whereas the utilization of the developed method for vortex identification was first published in Medical Engineering and Physics by Elsevier [321]. The article published by the Hindawi Publishing Corporation is an open access article was distributed under the Creative Commons Attribution License, which permits unrestricted use, distribution, and reproduction in any medium, provided the original work is properly cited. As 1^{st} author, my contributions were in running simulations, processing and analysing results, and drafting/editing the manuscript. Dr. Jiang oversaw and directed these activities, contributed to the creation of computational code for analysis, and drafting/editing of the resulting manuscript. Christopher Haferman aided in running and analyzing simulation data, and Dr. Gouthami Chintalapani aided in the collection of medical imaging data and editing of the manuscript. The materials presented in Chapter 3 have been reproduced from a previously published

article in Medical Engineering and Physics by Elsevier [321]: Volume 74, December 2019, Pages 129-136. As 1^{st} author, my contributions were code development, running of simulations, analysis of the results and drafting of the resulting manuscript. Dr. Jiang oversaw and directed these activities and contributed to the drafting and editing of the resulting manuscript. The materials presented in Chapter 4 of this dissertation are reproduced from a previously published work with permission from Journal of Biomechanical Engineering by The American Socieity of Mechanical Engineers [320]: 2019 May 29. doi: 10.1115/1.4043868. As 1^{st} author, my contributions to the work were in generation of computational models from medical imaging data, running the simulations, development of relevant analytic code development, analysis of all experimental data, and drafting and editing the resulting manuscript. Dr. Jiang oversaw and directed these activities and also contributed to the drafting and editing of the resulting manuscript. Whereas Dr. Qinghai Huang and Dr. Charlie Strother provided medical imaging data and aided in editing of the manuscript. The materials presented in Chapter 5 of this dissertation are reproduced from a previously published work in *Acta Neurologica Scandinavica* [322]: 2020, DOI 10.1007/s00701-020-04616-y. Documentation of the copyright transfer agreement which permits this reuse is presented in Appendix C. As 1^{st} author, my contributions were in the simulation and analysis of experimental data, development of computational code for analysis, processing and statistical analysis of results, and drafting the resulting manuscript. Dr. Jiang oversaw and directed these activities and also contributed to the drafting and

editing of the manuscript. Dr. Wang aided in the development of statistical analysis code and interpretation of results, Drs Aditya Pandey, Joseph Gemmete and Qinghai Huang performed collection of patient data, assisted in interpretation of data, and editing of the manuscript. While Austin Goudge contributed to data analysis. The materials presented in Chapter 6 are original findings that have yet to be be submitted to a scientific journal for review. My contribution to this work was in the development of the research plan, development of research equipment (flow chamber), performance of flow experiment, collection and processing of cellular data, and data analysis. Vicki Jia and Dr. Weilue Hue aided cell culture and interpretation of data, while Dr. Zhao oversaw and directed these activities and contributed to the drafting and editing of this chapter.

Acknowledgments

What a journey it has been in putting together this dissertation and achieving my PhD. The people who supported me along this constantly winding path have numerous and invaluable in my success. I am so fortunate for all their help and want to take a moment to thank them.

First, thank you to my advisors and dissertation committee members, without all of your guidance I would not have succeeded. Dr. Jingfeng Jiang and Dr. Feng Zhao whom served as wonderful advisors, pushing me both scientifically and professionally. As well as Dr. Sean Krikpatrick, Dr. Min Wang, and Dr. Gowtham Shankara, my committee members whom were instrumental in helping me reach this goal.

To my friends and family: thank you all for putting up with me being a distracted and rambling mess at times, and for the (occasionally) delayed remembrance of birthdays and special events. I am forever grateful for your patience with me, all of your unending support and faith, and letting me ramble on about my work. With all this behind me I hope to have more time to spend with you all.

Finally, I would be remiss if I didn't give thanks to Dr. Autumn Schumacher. Thank you for taking a gamble on a hopeful up-and-coming scientist right out of college, helping guide me to where I am at today.

List of Abbreviations

ACA	Anterior Communicating Artery
AFI	Aneurysm Formation Indicator
AUROC	Area Under the Reciever Operator Characteristic
CAD	Computer Aided Design
CFD	Computational Fluid Dynamics
DICOM	Digital Imaging and Communications in Medicine
DVO	Degree of Volume Overlap
EC	Endothelial Cell
ELISA	Enzyme-Linked Immunosorbent Assay
GON	Gradient Oscillatory Number
IA	Intracranial Aneurysm
ICA	Internal Carotid Artery
MCA	Middle Cerebral Artery
MLR	Multiple Logistic Regression
NVS	Normalized Vortex Surface
OSI	Oscillatory Shear Index
PC-MRI	Phase Contrast Magnetic Resonance Imaging
PDMS	Polydimethylsiloxane

PPFC	Parallel Plate Flow Chamber
ROC	Receiver Operator Characteristic
STA-WSS	Spatiotemporaly Averaged Wall Shear Stress
STL	Stereolithography
TA-WSS	Temporally Averaged Wall Shear Stress
TA-WSSMax	Temporally Averaged Wall Shear Stress Maximum
TA-WSSMin	Temporally Averaged Wall Shear Stress Minimum
VCAM-1	Vascular cell adhesion protein 1
VE-Cadherin	Vascular Endothelial Cadherin
VMTK	Vascular Modeling Toolkit
vSMC	Vascular Smooth Muscle Cell
VTK	Visualization Toolkit
VtV	Vortex Volume to Aneurysm Volume
WSS	Wall Shear Stress
WSSG	Wall Shear Stress Gradient
λ_2	Lambda$_2$

Abstract

Subarachnoid hemorrhage is a potentially devastating pathological condition in which bleeding occurs into the space surrounding the brain. One of the prominent sources of subarachnoid hemorrhage are intracranial aneurysms (IA): degenerative, irregular expansions of area(s) of the cerebral vasculature. In the event of IA rupture, the resultant subarachnoid hemorrhage ends in patient mortality occurring in 50% of cases, with survivors enduring significant neurological damage with physical or cognitive impairment. The seriousness of IA rupture drives a degree of clinical interest in understanding these conditions that promote both the development and possible rupture of the vascular malformations. Current metrics for the assessment of this pathology rely on measuring the geometric characteristics of a patient's vessel and/or IA, as well as the hemodynamic stressors existing along the vessel wall. Comparatively less focus has been granted toward understanding the characteristics of much of the bulk-flow within the vasculature and how it may play a role in IAs. Specifically, swirling hemodynamic flow (vortices) have been suggested as a condition which exacerbates vascular changes leading to IAs, yet quantified measurements of the spatial and temporal characteristics of vortices remain overlooked.

This dissertation studies the role of the spatial and temporal characteristics of vortex flow and how it plays a role on IA pathology. Its chapters are a collection of five (5)

works into this matter. First, established methods for the identification of vortices was investigated, and a novel method for vortex identification and quantification of their characteristics was developed to overcome the limitations of previous methods. Second, the developed method for vortex identification/quantification was then applied to a simulation study to improve predictive models aimed at predicting areas of IA development from those unlikely to suffer this pathology. Third, assessing how the simulated repair of one IA impacts changes to hemodynamic conditions within other nearby un-repaired IAs in a multiple IA system. Fourth, it was determined if vortex identification/quantification improved predictive models aimed at differentiation ruptured from unruptured IAs. Fifth, impart vortical flow of differing characteristics onto cultured vascular cells to determine if vortex stability imparts varied levels of cellular changes.

Chapter 1

Introduction

Subarachnoid hemorrhage is a potentially devastating pathological condition in which bleeding occurs into the space surrounding the brain. One of the prominent sources of subarachnoid hemorrhage are intracranial aneurysms (IA): degenerative, irregular expansions of areas in the cerebral arterial system which occur in an estimated 3-5% of the global population [130, 276, 348] with an estimated 0.15% - 0.7% of the global population suffer the rupture of an IA each year [148]. In the event of IA rupture, patient mortality occurs within 45-50% cases, with survivors enduring significant neurological damage and physical or cognitive impairment [211, 348]. From a clinical perspective, improved medical imaging techniques have increased the detection of IAs, and novel surgical methods have helped to reduce the instances of IA

rupture [186, 236]. Yet surgical interventions are not without inherent risks as complications cause similar neurological damage as a ruptured IA [56, 208, 222]. Current interventions focus on occluding blood flow into an IA through clipping or coiling. IA clipping involves opening the skull to place a titanium clip around the opening (ostium) of an IA, isolating it from the vascular flow. Yet a meta-analysis of studies between 1990 and 2011 showed this surgical methodology carried with it a 1.7% and 6.7% mortality and morbidity rate respectively [189]. A more recent method to prevent IA rupture is through coiling and stenting: the implantation of flexible wires (coils) inside an IA to create an artificial thrombosis within the IA sac, with the vascular stent supporting the weakened vasculature. Treatment of IAs with coiling has been shown to have an 80-85% success rate [236], yet carries with it complication risks: coil slippage, incomplete occlusion, or coil compaction which can further increase the risk of IA rupture [146, 208]. Surgical treatments to prevent identified IAs from rupture also carry significant economic costs: surgical repair (without complications) of IAs in the United States in 2012 cost an estimated $25,000 per patient, with surgical complications resulting in a marked increase in costs estimated between $35,000 - $70,000 [39]. While this cost can be impacted by the length of hospital stay, hospital size and IA locale [29], the cost to patients is significant. Additionally, a continued economic burden is placed upon patients and their caregivers if long-term rehabilitation or home care is required post-surgery. Improved understanding of the development and possible rupture of IAs could spur novel treatment methodologies

as well as aiding clinicians in determining the ideal treatment options to maximize patient outcomes.

1.0.1 Hemodynamic Factors of Aneurysm Development

The development of IAs are thought to be triggered in part by alterations to arterial cells due to the hemodynamic environment. Broadly speaking, the inner-most intima layer of cerebral arterial vessels consists of a monolayer of endothelial cells (EC) encapsulating the vessel lumen (internal space of a vessel) and are directly exposed to blood flow. This layer serves a dual purpose: hemodynamic mechanosensors which transduce fluid force into biochemical signals for cellular cascades [46, 92], and a selective permeability layer to govern the passage of biomacromolecules into arterial tissue [31, 121, 242, 275]. The tunica media (middle layer) of arterial vessels contains vascular smooth muscle cells (vSMC), elastic tissue, and collagen which regulate vessel contraction and dilation in response to hemodynamic forces/blood pressure, and help to maintain the biomechanical integrity of the vessel wall [37, 230]. Tangential fluid stressors along the vascular wall, wall shear stress (WSS), are known to impact vessel health, acting as a biological trigger for eliciting changes in the phenotype and genetic/protein expression of EC and vSMCs[19, 21, 43, 52, 89, 192, 281, 342]. Low WSS ($\leq$2dynes/cm^2) is associated with atherosclerotic changes to the vessel wall [50], whereas high WSS conditions are associated with local thinning of the wall

[228]. In addition to WSS intensity, fluctuations in both WSS gradients [91], as well as directionality [218, 297] have been linked with possible IA development. This assessment of WSS and its derivatives have been utilized to determine areas of likely aneurysm development, yet vary in both study outcomes and the predictive metrics utilized [45]. A possible limitation of such studies is that they tend to only assess the near-wall hemodynamic environment while overlooking the bulk flow patterns within the vasculature.

1.0.2 Current Rupture Prediction Metrics

When dealing with an identified IA, the disparity between their estimated rupture rate, risk of surgical complications, and possible unintended alterations to the hemodynamic environment post-surgery must be taken into account by clinicians. The need to properly weigh these concerns has led to significant interest in elucidating metrics indicative of IA rupture. Proper identification of IAs at high risk of rupture could significantly benefit-risk stratification, aiding clinical decision making and improving patient health outcomes, while also limiting the occurrence of (potentially) unneeded surgery.

Research has shown an array of risk factors exist which may signal IA rupture risk [87, 187, 259, 311] with said factors generally separated into three categories:

– IA morphological characteristics

– Vascular hemodynamics

– Patient health factors

Morphological factors such as IA size (volume), shape, aspect ratio, etc. have been identified across a plethora of studies as helpful in the assessment of IA rupture potential [93, 147, 264]. However, many of these parameters vary in both their predictive strength and to which parameters are "best" applied to models [15, 40, 164]. As per example, IAs >10mm in size are often associated with high rupture risk, with IAs >25mm thought to be at the greatest rupture risk. This prevailing thought leads the majority of large IAs to undergo surgical treatment even though not all large IAs rupture [234, 364, 372]. The inverse is seen in the assessment of small IAs (<4mm) of which are thought to be at minimal rupture risk. The perceived low risk could exclude many small IAs from surgical treatments, yet such IAs have been shown to be at a not-insignificant risk of rupture [93]. While geometric analysis of a patient's IAs and surrounding arterial geometry give much needed insight to clinical treatment planning, such information on its own would leave many IAs improperly assessed concerning their risk of rupture.

Assessment of WSS characteristics are a further avenue investigated to determine conditions symptomatic of IA rupture [49, 88, 164, 372]. Arterial cells are shown to

maintain healthy physiological characteristics while exposed to laminar hemodynamic patterns: flow following smooth paths, with minimal overlap between flow layers, and WSS between 5 and 30 dynes/cm^2 (varies by area of the vasculature). Yet in a similar manner to IA development, studies are in conflict if lower [38, 233, 392] or higher [89, 299] WSS values have greater impact on IA rupture. It has even been suggested that both sides of WSS extrema impact possible rupture via eliciting differing cellular changes[228, 308]. This duality of both high and low WSS impacting IA rupture may make determining their usefulness towards rupture prediction arduous. In a manner similar to IA development, fluctuations in WSS gradients and changes in WSS directionality are theorized to impact IA rupture, yet studies carry their own disagreements in prediction strengths [115, 307, 346, 370, 387]. The focus on WSS-based measurements also overlook the complex bulk flow characteristics that exist within the IA sac (Fig. 1.1)

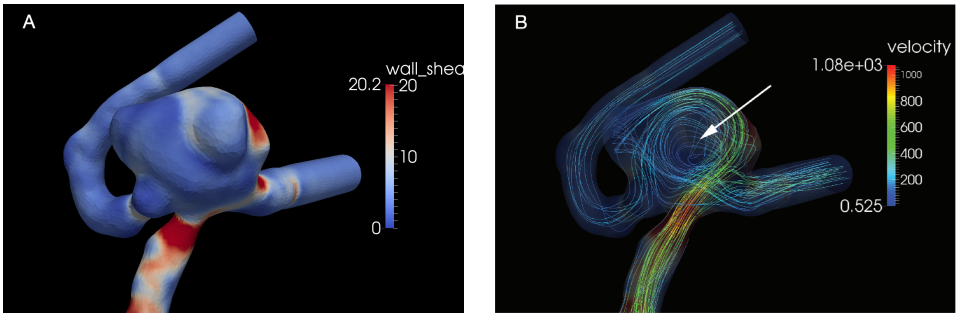

Figure 1.1: The wall shear stress (N/mm^2) distribution on the IA wall(A) and blood flow pattern inside the IA, visualized via velocity streamlines (mm/sec)(B). Solely analyzing WSS overlooks the disturbed/swirling flow patterns (white arrow) that are generated in the IA sac.

Combining the assessment of IA morphological characteristics, WSS and patient medical information have been applied in a number of studies toward predicting the risk of IA rupture. Yet the chosen indices and the resultant strength of models can vary significantly between studies. A sample of recent investigations (2017-2019) and their respective chosen metrics and prediction outcomes can be seen in Table 1.1.

This disparity between study outcomes for both IA development and rupture prediction suggest that novel assessment methods are needed to improve the understanding of characteristics indicative of this pathology.

1.0.3 Hemodynamic Swirling Flow: Vortices

Early investigations into the nature of IAs uncovered the non-random distribution of areas likely to develop IAs: vessel bifurcations and areas of significant arterial curvature (Fig 1.2). Within these locales, patterns of disturbed, swirling bulk flow (vortices) exists, antithetical to physiologic laminar flow.

The presence of hemodynamic vortices have been correlated with a number of arterial cellular changes indicative of IA development and rupture: altered cellular morphology, mechanotransducive signaling [24, 149], protein expression [21, 50, 67, 107, 240, 246], and ability to maintain a selective permeability layer [209]. Changes to vSMC have also been noted in areas of hemodynamic vortices, leading to reduced vessel

Table 1.1
Recent articles for IA rupture prediction

Author-Year	Parameters for Analysis	Aneurysm Location(s)	Ruptured IAs	Unruptured IAs	AUC orAccuracy
Qin et al., 2017[270]	W, H, L, NW, Age, AR, Dmax, HW, BF, WSS, LSA, EL	MCA	36	31	0.931
Bijlenga et al., 2017[36]	S, Age, Hyp, Race, SAH	MCA, ICA, ACA/PcomA/-Post	598	243	0.681-0.756
Detmer et al., 2018[85]	Age, Gender, S, OSIm, NSI	ACA, AcoM, BA, ICA, MCA, PCom, VA	66	183	0.82
Kocur et al., 2019[183]	S, H, W, NS, AR, BF, H/W, SR, Aθ	AcoM, ICA, MCA, Post	146	285	0.55-0.64
Wang et al., 2019[355]	R, DD, NW, W, D, Dia, AR, DW, BF, SR, Fθ, LDθ, SDθ,	AcoM	214	147	0.846
Varble et al., 2018[346]	Age, SR, AR, UI, EL, NSI, WSS, OSI, WSSG, RRT, LSA, MWSS, PLc, EL	ACA, ICA, MCA, PcoM, Post	102 (Train) 14 (Test)	311 (Train) 115 (Test)	0.767
Jiang et al., 2018[163]	L, H, AR, SR, UI, EI, Dθ, NSI, NWSSa, WSSm, WSSa, NWSSa, NWSSm, WSSG, LSA, OSI, RRT, Pm, Pa, NPa, NPm	ACA, AcoM, ICA, MCA, PcoM	167	167	0.81

Anterior communicating artery (AcoM), Anterior communicating artery (ACA), Internal carotid artery (ICA), Middle cerebral artery (MCA), Posterior communicating artery (PcoM), Posterior inferior cerebral artery (Post), Aneurysm angle (Aθ), Area (A), Aspect Ratio (AR), Bottleneck factor (BF), depth/width (DW), Diameter (D), Energy Loss (EL), Flow angle (Fθ), Height (H), Hypertension (Hyp), Irregular shape (IR), Large daughter artery angle (LDθ), Lateral angle ratio (LAR), Length (L), Low wall shear area (LSA), Mean diameter (MD), Mean wall shear stress (MWSS), Non-sphericity index (NSI), Normalized pressure average (NPa), Normalized pressure max (NPm), Normalized wall shear stress area (NWSSa), Normalized wall shear stress mean (NWSSm), Oscillatory shear index(max) (OSIm), Pressure average (Pa), Pressure loss(coefficient) (PLc), Pressure max (Pm), Relative residence time (RRT), Size ratio (SR), Small daughter artery angle (SDθ), Surface (S), Temporally averaged WSS (TAWSS), Undulation Index (UI), Vessel angle (Vθ), Width (W), Wall shear stress (WSS), Wall shear stress gradient (WSSG), Wormsley number (WN), Wall shear stress mean (WSSm).

contractility and mechanical integrity, conditions indicative of IA development and rupture [170, 259]. Prolonged disturbed flow conditions are also linked to increased cellular death (apoptosis) of EC and vSMCs, further weakening the vascular wall and exacerbating this pathology [86, 177, 198].

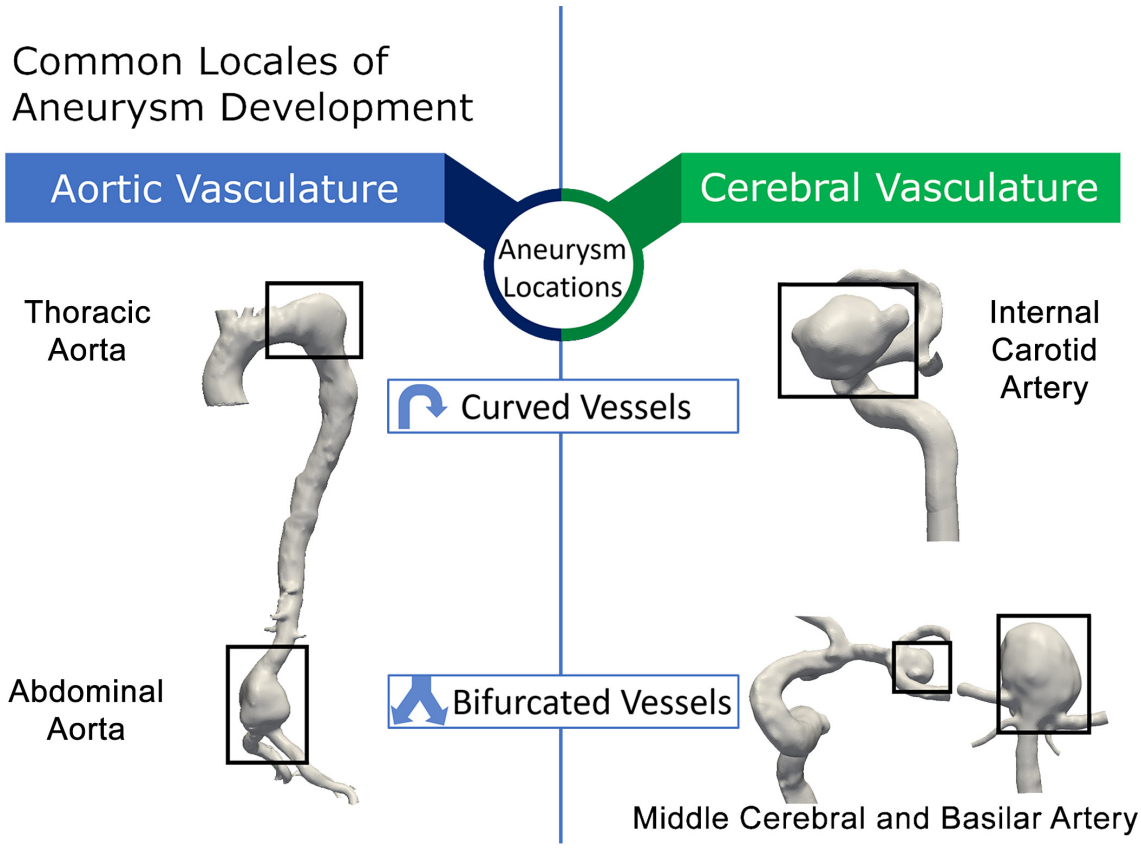

Figure 1.2: Common locales of aneurysms in the human vasculature. High vessel curvature and bifurcations in the aortic and cerebral arterial system are shown to be likely areas of aneurysm development (black boxes). Areas represent aneurysm locations at the thoracic and abdominal portion of the aortic vasculature as well as the internal carotid, middle cerebral, and basilar arteries of the cerebral vasculature

While the presence of vortices has been linked with altered arterial cells, less is known about the characteristics of vortices and if they can help lead to novel insights into the risk of IA development and rupture. Current vortex analyses are typically restricted to qualitative visual assessment of computational fluid dynamic (CFD) derived flow or assessment of only votrices' center-most (critical-point) regions[42, 252, 345]. Additionally, *in-vitro* study of vortices often involve the generation of relatively simple

and spatially stable vortices (compared to *in-vivo* counterparts) using specialized flow chambers [23, 47, 62, 67, 68, 122, 318]. Such methods result in a narrow assessment of vortices that may overlook important spatial and temporal flow characteristics that could prove indicative of IA pathology. Research focused on understanding the impact that vortex characteristics have on IAs, and determining if said analysis is useful in differentiating IAs likely to rupture from those to remain asymptomatic[345] could significantly improve the understanding, and eventual clinical management of, this pathology.

1.0.4 Objectives and Contributions

The objectives of this work are composed of computational, analytic, and *in-vitro* investigations of vortices and their relationship to IAs. Primarily these investigations focus on determining if quantifying and analyzing the spatial and temporal characteristics of vortices can be utilized to improve the understanding of IA development and rupture. The contributions of each work toward this end are as follows: **one)** develop a novel methodology for the identification of vortices beyond their critical-point regions as a means to improve the quantification of their spatial and temporal characteristics, **two)** determine the strength of vortex characteristics for predicting areas of IA development, **three)** how the surgical repair of and IA may alter bulk-flow characteristics within the vasculature and/or subsequent unprepared IAs, **four)**

improve the differentiation of ruptured and unruptured IAs by analysis of vortex characteristics, and **five)** determine if vortices of varied spatiotemporal stability trigger differing levels of cellular change indicative of IAs. The combination of such an analytical methodology and an understanding of how vortex characteristics are indicative of IA development, growth and rupture could give much-needed insight towards this potentially life-threatening arterial malformation.

Chapter 2

Hemodynamic Flow Vortex Identification and Quantification of Characteristics

Assessment of hemodynamics indicate that vortical flow spatial complexity may impact IA pathology[43]. Yet the methods driving the identification of vortices in many studies rely on visual assessment of velocity streamlines (lines tangental to the velocity vector of flow), or analysis of only the critical point of vortex patterns [42, 119, 284, 345]. Reliance on streamline visual assessments could lead to varied inter-rater reliability while giving no quantifiable characteristics of flow. As for critical point methods, they assess pressure minimum locales to identify the center-most

region of areas of swirling flow, yet give no information of the broader flow structural characteristics. The initial goal of this dissertation was the development of an alternative technique for vortex analysis, expanding upon vortex core analysis to assess the spatial and temporal characteristics of the broader structure of vortices [319]. For this purpose, an initial method was investigated by expanding upon two established vortex identification methods, the Q-criterion [150] and λ_2 [159]. Additionally, an analytical method based on Shannon's informational entropy [291] was developed as an alternative vortex identification metric not wholly reliant upon critical point analysis.

2.1 Generation of Hemodynamic Flow Data

To achieve the goal of this chapter, high resolution hemodynamic data is paramount for the initial development of analytic techniques, especially due to the complex nature of flow within IAs. In a clinical setting, time-resolved three-dimensional flow velocity data (3D velocity vector fields) can be measured using phase-contrast magnetic resonance imaging (PC-MRI) or phase-contrast magnetic resonance angiography (PC-MRA)[32, 227]. Yet, determining flow details in and around IAs has proven difficult using such methods. The complex, disturbed patterns of IA flow results in incoherent velocities (at the sub-grid level) and these specific characteristics may not be resolved using typical "averaged" velocity measurements at the relatively large resolutions of medical imaging (at $\geq$1-mm scale)[2]. As a consequence of sub-grid

limitations, clinical hemodynamic flow measurements may be subject to errors and imaging artifacts[227, 315], altering the characteristics of vortices within IAs. CFD applies aspects of fluid mechanics, data structures, and numerical analysis, alongside advancements in computational power and mathematical models as a means to calculate fluid flow within a defined system. This field of computational science has garnered interest by the clinical and research community as a means to better understand and analyze flow in and around IAs while being more robust against limitations faced in *in-vivo* measured flow data [51, 370]. CFD simulation can achieve spatiotemporal resolutions at factors greater than MRI data, up to a computer's memory limit, and can generate data free from imaging errors and/or flow artifacts. High quality flow data allows for the development of novel analytic techniques to be tested and refined on data free from errors which may confound initial outcomes.

2.1.1 Modeling of "Patient-specific" Vasculature

Medical imaging data was taken from Digital Imaging and Communications in Medicine (DICOM) files of ten (10) patient's vasculature structure using digital subtraction angiography (DSA). These files were arbitrarily selected from an internal database: five patients with a single bifurcation (terminal) aneurysm, and five with a single sidewall aneurysm. Cases were chosen that had either an IA in the internal carotid artery (ICA) or the basilar artery (BA). A commercially available image

segmentation package (Mimics Innovation Suite, version 17, Materialise Inc. Leuven, Belgium) was used to reconstruct the vascular surface from scans, resulting in 'patient-specific' vascular structures. All structures were loaded into the commercially available computer aided design (CAD) 3-matic software (Version 9, Materialize Inc., Leuven, Belgium). The longest available upstream vessel section proximal to the aneurysm was left intact to maintain as much of the patient geometry possible, while much of the vasculature distal to the aneurysm was removed, leaving a small portion as vessel outlets: for both ICA or BA IAs, the vessel bifurcation that occurs post-IA was kept intact. Remaining surface irregularities were manually removed using the localized smoothing function, and a 1^{st} order Laplacian smoothing filter was used post-editing to perform a global smoothing to the vessel structure. Cylindrical vessel extensions 6 times the relative vessel diameter were added to both the inlet and outlet vessels for each model using the open-source Vascular Modeling Toolkit (VMTK) software (version 1.2). Vessel extensions help reduce the effects of inlet, plug-flow conditions, allowing flow correction to parabolic flow indicative of physiologic hemodynamic characteristics [266].

2.1.2 Mesh Generation

Processed vascular surface structures were converted into an unstructured, 3D, tetrahedralized volumetric mesh using an open-source mesh generator, Tetgen (version

1.4.2) [301]. The mesh generation process was performed by an in-house Python script derived from VMTK. Approximately, 1 million tetrahedral computing cells were used per case, with the average mesh size as 0.0022-mm^3, with 3 layers of prism computing cells along the wall of vessels as a means to achieve greater WSS accuracy [105]

2.1.3 CFD Simulation

To compute fluid velocity data in and around the IA, the time-dependent 3D Navier-Stokes equations was numerically solved using a commercial CFD solved (ANSYS-FLUENT Inc., version 14.0, Lebanon, NH) In the ANSYS-FLUENT solver, the pressure-velocity coupling was obtained using the Semi-Implicit Method for Pressure Linked Equation (SIMPLEC) algorithm [347] with a first-order streamline-upwind stabilization approach. The explicit time-marching second-order scheme with a time step of $1 \times 10^{-}3$ second (1000 steps per cardiac cycle) was used for computations.

Vessel walls were assumed rigid with a no-slip boundary condition. It is worth nothing that blood vessels are naturally compliant and an assumed rigidity causes a rise in overall wall shear stress values (30-50%), while flow pattern characteristics remain similar or only have small localized changes [27, 255, 303]. This assumption ensures a

reduced computational time and lessens required computer memory. Blood was considered an incompressible Newtonian fluid with a dynamic viscosity of 0.004 kg/m-s and a mass density of 1040 kg/m^3. Assuming blood as Newtonian is shown to increase WSS while minimal changes occur in flow patterns [193]. A zero-pressure condition was used for all vessel outlets. For the inlet flow rate, two pulsatile waveforms (one for ICA and BA respectfully) at a rate of 60 bpm were derived from magnetic resonance measurements taken from Gwilliam et al. [128] as patient-specific flow waveforms were not available. Each case had its waveform scaled according to their inlet cross-sectional area, standardizing the mean volumetric flow rate to either 280mL/min for ICA cases or 180mL/min for BAs, values based on MR measured physiological rates [101, 390]. Four (4) cardiac cycles were simulated per case at 20 data points per cardiac cycle, with only the final cycle saved as a means to reduce initial transient flow conditions.

A published method [161] was used to semi-automatically isolate and extract the IA sac from its parent vessel. The isolated IA sac was sealed at the IA opening (ostium) and converted to a binary mask, spatially-registered with the volumetric velocity data. The mask allows the analysis of only the intra-aneurysmal velocity data, reducing the time for computational analysis. Masked velocity data was re-sampled from a high-resolution tetrahedral mesh to a 3D rectilinear grid format to mimic the data format used by PC-MRI. This was performed so that the developed method(s) could easily be adapted to *in-vivo* medical imaging data in the future. Re-sampling of data was

performed for a range of voxel sizes (0.1-0.8mm) to assess its impact on identified vortices.

All computational methods for the identification and quantification of the spatial and temporal characteristics of vortices were performed using in-house scripts (C++ and Python) developed using the open-source VTK/VMTK software package.

2.1.4 Vortex Core Identification and Analysis: λ_2 and Q-criterion Methods

Two of the most prominent methods for the identification of flow vortices via the identification of critical point, rely on the analysis of the symmetric rate-of-strain and skew-symmetric vorticity portion of a second order flow tensor. To achieve this, the eigenvalues of the velocity gradient tensor field within a system is calculated and when a pair of complex conjugate eigenvalues are identified, the tensor field is deconstructed into its rate-of-strain and vorticity tensors as calculated in Equation 2.1.

$$\nabla\vec{u} = S + \Omega$$
$$S = \frac{1}{2}\left[(\nabla\vec{u}) + (\nabla\vec{u})^T\right] \tag{2.1}$$
$$\Omega = \left[\frac{1}{2}(\nabla\vec{u}) - (\nabla\vec{u})^T\right]$$

Where $\nabla\vec{u}$ is the calculation of the velocity gradient, S as the rate-of-strain tensor and Ω as the vorticity tensor.

Using these values, Hunt, Wray and Moin [150] defined a vortex as a connected fluid region with a positive second invariant ∇u, where the Euclidean norm of the vorticity tensor dominates. This is referred to as the Q-criterion method

$$Q = \frac{1}{2}\left[|\Omega|^2 - |S|^2\right] > 0 \tag{2.2}$$

Jeong and Hussain identified vortices as a connected flow region with two negative eigenvalues and S^2 and Ω^2 as:

$$\lambda_2 = (S^2 + \Omega^2) < 0 \tag{2.3}$$

This is referred to as the λ_2 method.

These two methodologies were assessed using our simulated data. While from a mathematical perspective, a critical point is indicated by either a $\lambda_2 < 0$ or Q > 0, setting

analytical thresholds close to these values was found to overestimate areas of flow as being indicative of a vortex. To limit the over-identification of areas of flow as part of vortices, a number of computational thresholds were tested. Additionally, modifications to the Q and λ_2 methodologies was performed through the normalization their values by their $\vec{u}^2$ via Equation 2.4. Normalization was performed to narrow the distribution of possible values for the identification methods, helping to minimize marked differences in vortex characteristics due to slight changes in thresholds. Subsequently, methods were also tested to determine its susceptibility to varying data resolutions[319]. As previously stated, data resolution can vary significantly between CFD derived data and clinically measured data, so having a analytical methodology robust to differing data quality could help minimize research findings between separate studies.

$$\begin{aligned} Q(x,t) &= \frac{Q(x,t)}{|\vec{u}(x,t)|^2} \\ \lambda_2(x,t) &= \frac{\lambda_2(x,t)}{|\vec{u}(x,t)|^2} \end{aligned} \tag{2.4}$$

For all (10) simulated cases, multiple threshold values for λ_2 and Q-criterion methods (standard and normalized) were assessed within the intra-aneurysmal velocity data. Based off each case's resultant Q or λ_2 values, five threshold values were tested:

† Mean.

† Mean$\pm$Standard Deviation

† Mean$\pm$Half Standard Deviation

† Mean/2

† Mean/4

When the standard deviation was included as part of the threshold, the value was added for the Q criterion threshold, and subtracted for the λ_2 threshold. This was done to account for the theoretical thresholds for vortex identification as > 0 for Q and < 0 for λ_2.

Identified vortex areas were mapped to 3D iso-surfaces: surface representation of values within a given space, using the well-established marching cube algorithm[212]. The volume of identified iso-surfaces was calculated and averaged across the simulated cardiac cycle. As a means to determine the stability of vortices, the degree of volume overlap (DVO) between *flow vortex regions* of adjacent time-steps was calculated: i^th and $(i+1)^th$. DVO values ranging from 0 indicating no overlap between vortex areas of adjacent time-steps equating to low stability, to 1 as having no change in the spatial characteristics indicating a completely stable structure. The temporally-averaged DVO value (TA-DVO) and standard deviation of DVO over the cardiac cycle (STD-DVO) were calculated for each case. Additionally, the number of spatially separated vortices were calculated and their value averaged over all 20 time-steps.

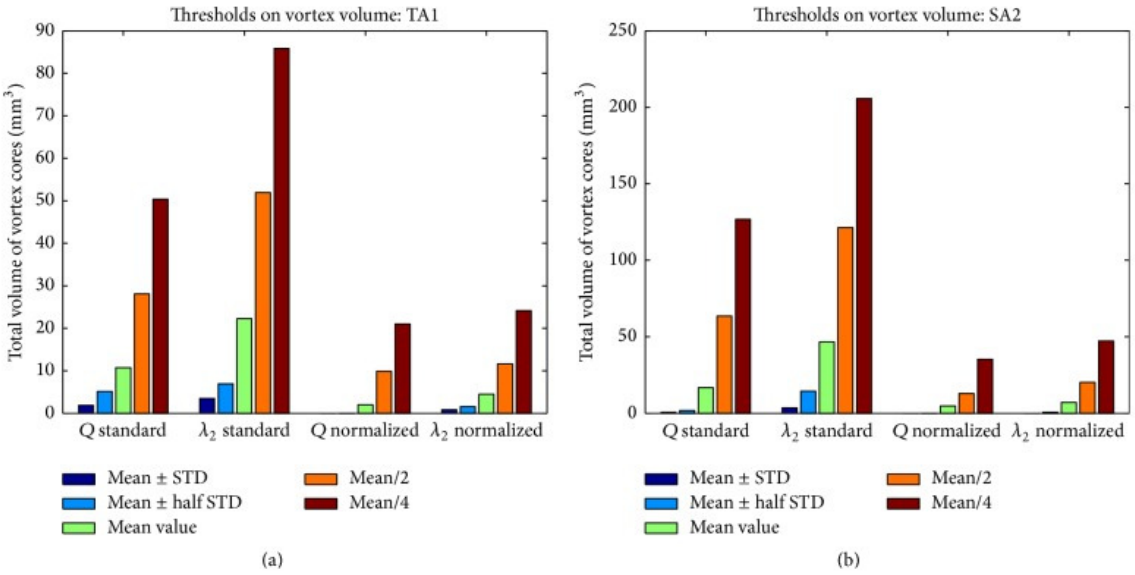

Figure 2.1: Variations of identified vortex volumes due to altered threshold values in (a) TA1 and (b) SA1. Threshold values were tested for four vortex extraction methods: standard Q-criterion, standard λ_2 method, [normalized] Q-criterion, and [normalized] λ_2 method. Selected threshold values were mean/4, mean/2, mean, mean $\pm$ (STD/2), and mean $\pm$ STD (added STD for Q-criterion and [normalized] Q-criterion and subtracted STD for λ_2 and [normalized] $\lambda_2$methods).

2.2 λ_2 and Q-criterion Outcomes

Across all cases studied, a threshold larger than mean$\pm$0.5Std resulted in a significant reduction in the overall identified vortex volume, with some cases having no vortices identified (Figure 2.1). Alternatively, reducing threshold(s) past mean/2 resulted in a significant increase in identified vortex volume, as regions (visually) corresponding to minimal flow disturbances, unlikely to be a part of a vortex. A visual representation of these changes can be seen in Figure 2.2.

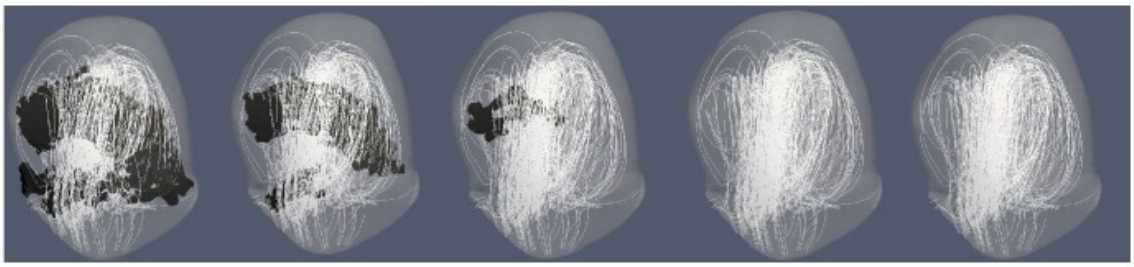

Figure 2.2: Extracted vortex cores (black surface) under varied analysis threshold values. From left to right: mean/4, mean/2, mean, mean + (std/2), and mean + std. All images were from case TA 1, [normalized] Q-criterion at a 0.2mm resolution. At threshold values $\geq$mean + 0.5std, a reduction, or lack of identified vortex structures occurred.

Changes to vortex characteristics under varied thresholds determined that, in terms of the absolute volume change of identified vortices, the [normalized] Q-criterion and [normalized] λ_2 method proved more robust than their non-normalized counterparts: smaller changes due to threshold variation. Visual assessment of the extracted vortex *iso-surfaces* alongside their simulated velocity streamlines showed the normalized identification methods better identified regions of swirling flow the the vortex core without including large portions of the flow along the curvature of the aneurysmal wall as shown in Figure 2.3. Further analysis of vortices under varied conditions was performed using the normalize Q-criterion method. The summary of vortex parameters measured using this method can be seen in Table 2.1.

Re-sampling of simulated data to varying voxel sizes determined spatial resolution's impact on the [normalized] Q-criterion method. In order to reduce the appearance of small, isolated areas of flow being mistaken as part of vortex structure(s), only

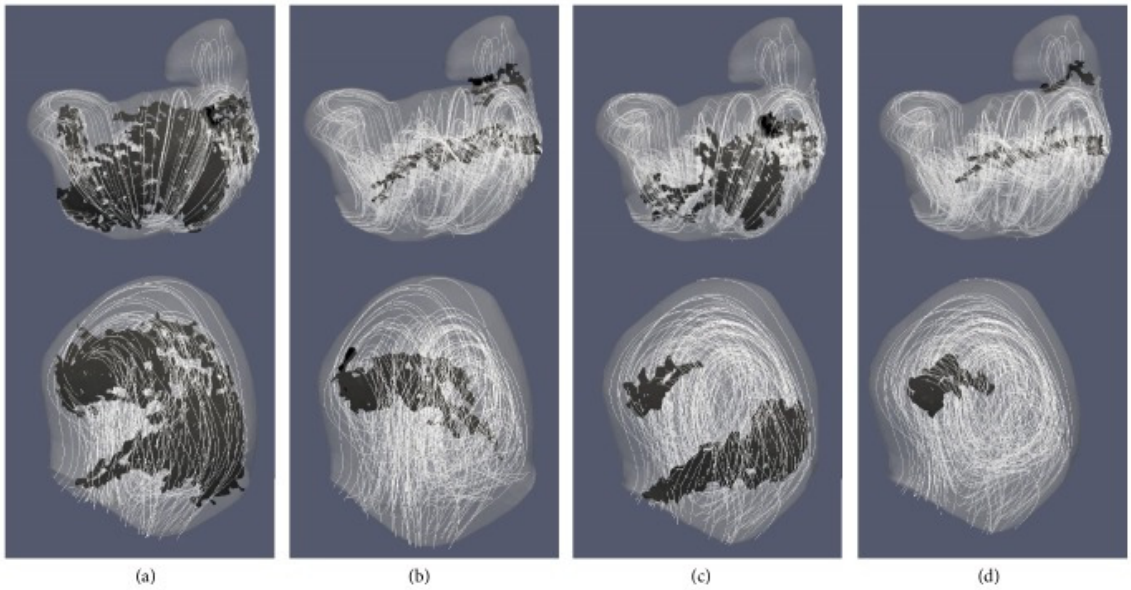

Figure 2.3: Comparison of identified vortex cores from four methods: (a) standard λ_2, (b) normalized λ_2, (c) standard Q-criterion, and (d) normalized Q-criterion. Top row is from one sidewall IA case, and bottom row is from a terminal IA case. Velocity streamlines were visualize to represent simulated flow patterns. Threshold values for each case were their means (for representative value), and only extracted vortex cores with a volume $> 0.5\text{mm}^3$ are shown.

connected vortex regions with a volume $\geq 0.5\text{mm}^3$ were analyzed. Through a visual inspection, we found that as voxel size changed, structural characteristics of the vortex core(s) were altered (Figure 2.4, which could lead to a misinterpretation of the temporal flow characteristics within an IA when data resolution is not held constant across studies. Data of resolution (<0.2mm) caused the vortex structure to become fragmented, dividing larger *iso-surfaces*, creating a greater chance of small divided vortices to exist below the chosen 0.5mm^3 volumetric cut-off. Figure 2.5 shows how changes to voxel sizes impact the mean DVO and the mean number of cores over the cardiac cycle

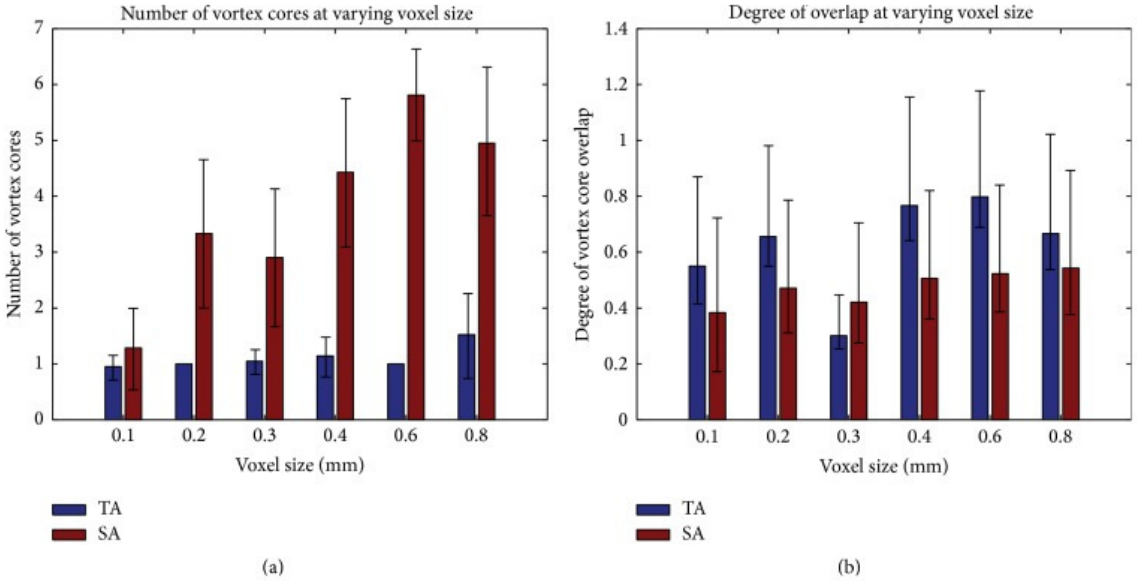

Figure 2.4: Alterations to vortex core characteristics over voxel sizes 0.1mm to 0.8mm: (a) changes to the number of vortex cores and (b) changes to DVO. Error bars stand for ± one STD.

Table 2.1

Summary of three vortex parameters in all 10 IA cases using the Q-criterion method (normalized): average vortex volume, mean and standard deviation of the number of vortex cores across cardiac cycle, and mean and standard deviation of DVO across the cardiac cycle. The identification threshold was set as mean + one STD.

Aneurysm	**Mean Vortex Volume (mm^3)**	**Mean Number of Cores**	**Mean DVO**
TA 1	2.015	1.048±0.218	0.301±0.082
TA 2	8.823	3.667±0.577	0.592±0.150
TA 3	2.021	1.191±0.402	0.651±0.147
TA 4	3.042	2.714±0.644	0.574±0.122
TA 5	0.504	0.762±0.768	0.382±0.386
SA 1	0.838	1.095±0.436	0.508±0.190
SA 2	4.783	2.905±1.221	0.420±0.184
SA 3	0.693	0.905±0.768	0.229±0.220
SA 4	2.570	1.429±0.507	0.594±0.143
SA 5	55.465	5.429±1.661	1.296±0.068

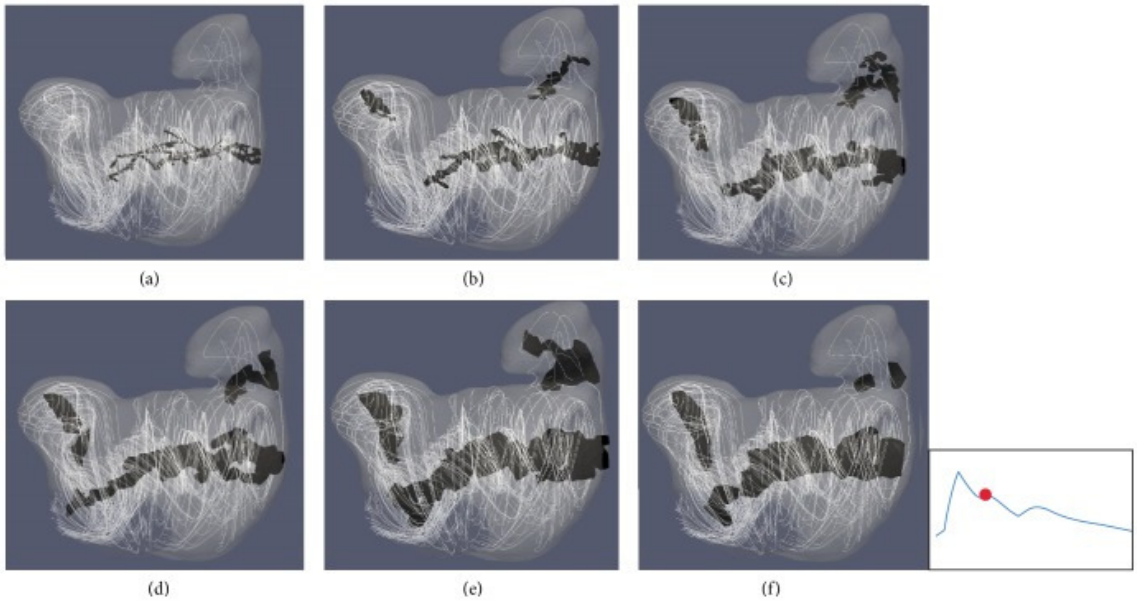

Figure 2.5: Visual comparison of voxel size on extracted vortex core structures for case SA2. Voxel sizes: (a) 0.1mm, (b) 0.2mm, (c) 0.3mm, (d) 0.4mm, (e) 0.6mm, and (f) 0.8mm. Vortices were identified using the [normalized] Q-criterion method, a threshold value of the mean [normalized] Q value per case, and only cores with a volume $> 0.5\text{mm}^3$ were saved. The marked waveform shows the data point in the cardiac cycle used for extracting the structures.

As the main goal of quantifying vortex spatiotemporal characteristics is to develop novel indices for determining an IAs risk of rupture, the collinearity of vortex characteristics to IA geometric characteristics was determined. Colinear variables applied to statistical predictive models may inflate estimate variances and confound the relationship between predictors and outcomes[165, 380]. Person's linear correlation between IA geometric characteristics and the quantified vortex variables was calculated and can be seen in Table 2.2.

Table 2.2
Pearson's linear correlation between geometrical parameters of IAs and characteristics of their vortex structures

Mean Number Vortex Cores	**Terminal Aneurysms**		**Sidewall Aneurysms**		**Combined Data**	
	Correlation coefficient	p value	Correlation Coefficient	p value	Correlation Coefficient	p value
Aneurysm Volume	0.142	0.820	0.995	<0.001	0.814	0.004
Ostium Area	0.150	0.810	0.825	0.0855	0.621	0.0552
Ostium Circumference	0.125	0.812	0.774	0.125	0.560	0.093
Aneurysm Height	0.735	0.15	0.906	0.034	0.831	0.003
Aspect Ratio	0.596	0.289	0.659	0.227	0.616	0.0581
Volume/Ostium	0.233	0.706	0.998	<0.001	0.826	0.003
Mean DVO						
Aneurysm Volume	-0.522	0.366	-0.416	0.487	-0.416	0.231
Ostium Area	-0.433	0.466	-0.691	0.196	-0.632	0.0499
Ostium Circumference	-0.415	0.487	-0.743	0.150	-0.640	0.046
Aneurysm Height	0.036	0.954	-0.201	0.746	-0.227	0.528
Aspect Ratio	0.442	0.456	0.420	0.481	0.424	0.223
Volume/Ostium	-0.637	0.248	-0.350	0.564	-0.375	0.286

2.3 Vortex Core Identification: Shannon's Entropy

While the utilizing a normalized Q-criterion method was found to be most robust critical-point method to altered threshold values and less apt to identify flow along the IA wall as part of vortex structures, such methods are still solely dependent on critical point analysis. Additionally, as seen in Figure 2.3, these methods tend to result in a disjointed or fragmented vortex *iso-surface* which may result in a perceived reduction in both the size of the vortex and its spatiotemoral stability, and would make it susceptible to flow changes dude to flow data artifacts/errors. A novel methodology for vortex identification was developed applying concepts from informational (Shannon's) entropy [292] to overcome the shortcomings of strict critical point methods.

Shannon's entropy expresses the information a system, specifically how deterministic/the probability that a specific event will occur. High entropy equates that no specific event is likely to occur at a greater extent over any other, with an entropy of zero indicating only one specific event occurs. From the perspective of flow analysis, Shannon's entropy can be applied to determine the flow directionality within a given region of interest (ROI). An overview of this methodology can be seen in Algorithm 1, with in-depth details provided below.

Algorithm 1 Pseudo Code: Normalized Entropy for Vortex Analysis

```
Input: aneurysmal velocity data (.vti format)
Allocate memory for and calculate orientation of 360 bins
for iteration = 1, 2, ..., N (points in data) do
    Calculate and normalize vector directionality
    Determine normalized bin to which vector aligns
end for
for iteration = 1, 2, ..., N (points in data) do
    for iteration = 1, 2, ..., K points around N do (11x11x11 ROI)
        Calculate number of vectors aligned with each bin / K = p(x_i)
    end for
    Calculate entropy in ROI: -∑ p(x_i) log_2 p(x_i)
    Normalize Entropy (normalized to log(K))
end for
```

The spatially-varying directionality of a flow field was determined by first dividing its 3D angular space into 360 bins of equal area (Lepordi method)[202]. This creates a series of 'cones' with with surface patches connected to a unit sphere center 2.6. Velocity vectors within the system are overlaid within this unit sphere, identifying the cone to which each velocity vector aligns. The probability $p(x_i)$ of the velocity field (X) direction $(x : \epsilon(x_1, x_2...x_n))$ aligning with a specific bin determines the entropy

of the system.

$$H(x) = -\sum_{x_i \epsilon X} p(x_i) log_2 p(x_i) \tag{2.5}$$

To which the entropy H(x) is normalized against the maximum possible entropy within the system (log(K))2.6.

$$NE(X) = \frac{H(X)}{log(K)} \tag{2.6}$$

As the overall direction of velocity vectors within the flow field concentrate towards the same bin, entropy is seen as a minimum (0), whereas the probability of vectors occurring in any direction as equally likely results in a value closer to 1. For the analysis of flow in this work, velocity vectors within a ROI around each voxel was performed as to determine said voxel's NE. The ROI was fixed at $N_x x N_y x N_z; N_x = N_y = N_z = 11$

While the use of Shannon's entropy aims to overcome limitations of critical point methods for vortex identification, sole reliance this method carries an inherent limitation: the inability to distinguish between swirling flow and random (Brownian) flow (Figure 2.7).

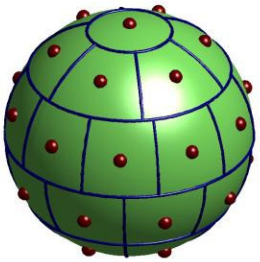

Figure 2.6: Example of a unit sphere divided into 'bins' of equal area using the Leopardi method.

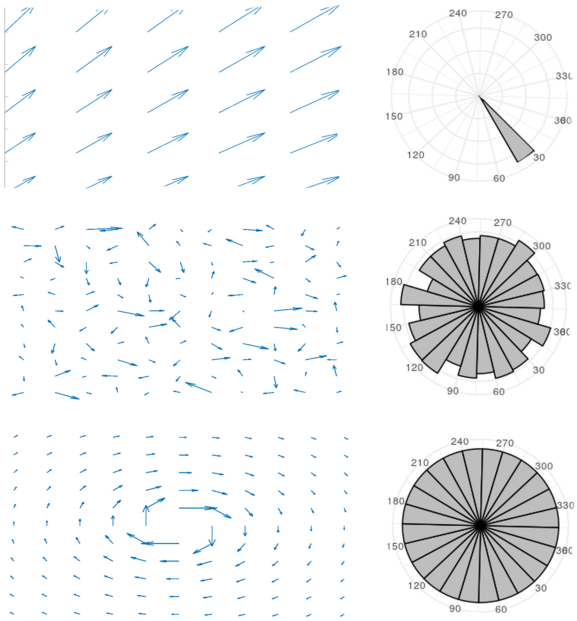

Figure 2.7: The relationship between 2D flow patterns, angular histogram and entropy: (top) laminar flow, (middle) Brownian (random) flow, (bottom) perfectly rotational flow. The left and right plots are the 2D vector flow field and their histogram of angular vector direction respectively. Laminar flow has an entropy value close to 0, while both random and rotational flow have similar histogram frequency distribution with entropy values close to 1.

While the probability of vectors within Brownian and swirling flow both result in NE towards 1, the two patterns represent different flow structures and must be properly differentiated to identify vortices. The nature of randomized (Brownian) flow is such

that it is unlikely to contain a centroid region. This lack of a defined centroid region in Brownian flow is exploited to help the developed Shannon's entropy method better identify areas of vortices. When a voxel is identified (via Shannon's entropy) as possibly belonging to a vortex region, its λ_2 value is calculated. When this value is $<$ 0, the dot product of the voxel's normalized velocity vector $||\vec{u}||$ and its eigenvector (λ_u,) is calculated, determining the angle between the vector and its degree of change.

$$du(\theta) = ||\vec{u}|| \cdot \lambda_u \tag{2.7}$$

The multiplication of $du(\theta)$ alongside a voxel's NE allows for the differentiation of swirling flow from Brownian flow as values $<$**0.3** are likely to belong to Brownian flow and can be excluded from additional analysis. For this dissertation, utilizing Shannon's entropy alongside Equation 2.7 to identify vortices will be referred to as the combined entropy (CE) method.

$$CE_x = NE(X) * du(\theta)_x \tag{2.8}$$

2.3.1 CE Method Analysis

In a similar fashion as the assessment of the Q-criterion and λ_2 methods, the CE method was tested under varied conditions to determine its susceptibility to data resolutions. Vortices analyzed using the CE method were found to have little to no statistical differences in their resultant DVO values as a function of data resolution. Yet, statistical differences ($p < 0.05$) in vortex volumes were noted in many of the TA cases. Specifically, a marked increase was seen in vortex volumes between the voxel sizes of 0.2 and 0.3 mm. Visual assessment of *iso-surfaces* in these cases shows a trend where separate vortices in the 0.2mm voxel size, are connected in 0.3mm voxel data, accounting for the increase in vortex volume. This similar phenomenon was not seen in the sidewall IAs, where statistically significant increase in vortex volume was not noted between 0.2mm and 0.3mm voxels. In contrast, a volumetric decrease was seen in many of the SA vortex volumes at lower resolutions: $\geq$ 0.4mm. This difference in IA type's susceptibility to data resolution may be in-part due the nature flow entering the IA sac. In TAs, the main flow jet tends to enter perpendicular to the IA ostium where it then splits laterally within the IA sac (Figure 2.8). A larger voxel size may cross this flow division, connecting otherwise distinct areas of swirling flow. Continued analysis of vortices in other areas of the vasculature containing TAs (MCA, AcoM, etc) should be investigated as IA locales may impact vortex characteristics. The ROI size used in the CE method was also assessed to determine its impact on quantified

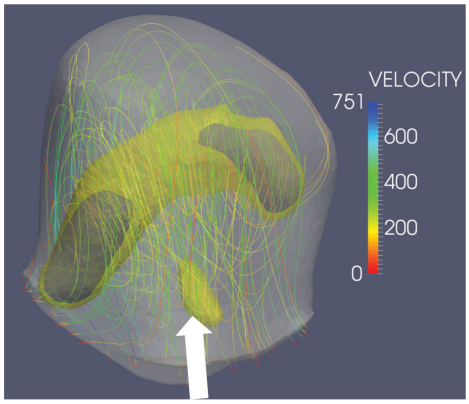

Figure 2.8: Comparison of vortex *iso-surfaces* between one example TA. Black surfaces are vortices identified at 0.2mm and yellow at 0.3mm voxel size. Streamlines show flow pattern and flow velocity (mm/s)

vortex characteristics. 3 ROI sizes were compared across all 10 cases: N_7, N_{11}, N_{15}. For all these tests, the voxel size of 0.2mm was held constant. The volume of identified vortices were found to be statistically different between each ROI size ($p < 0.05$) with an inverse relationship: as N increases, the vortex volume decreases.

Comparison of the DVO values between the CE and normalized Q-criterion method showed an increase in value when applying the CE method: p-value < 0.001 (-0.359.-0.177 95% CI). While differences were shown between the quantified characteristics of vortices between these two methods, it is important to note that visual assessment of *iso-surfaces* showed similar spatial placement between the two methods (Figure 2.9).

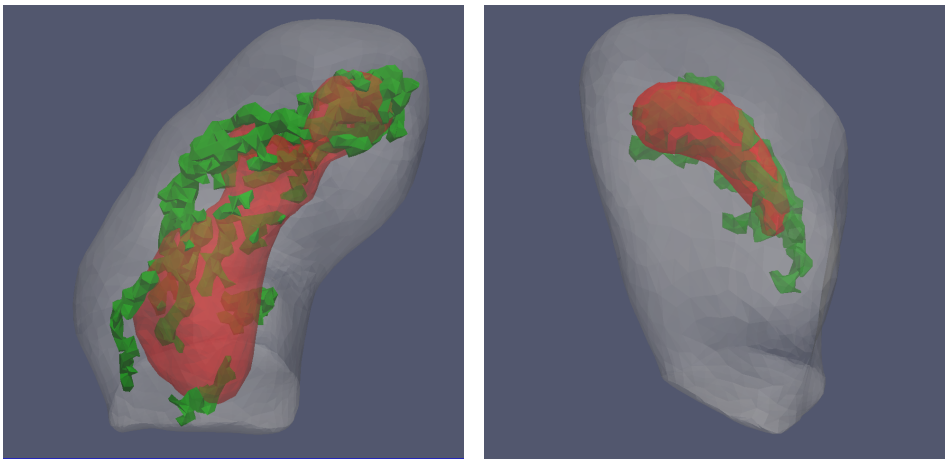

Figure 2.9: Comparison of spatial placement of identified vortex *iso-surfaces* between the (green) normalized Q-criterion method and (red) CE method. Two representative cases shown: **(left)** sidewall IA and **(right)** terminal IA, both vortices taken from the 5^{th} step of the cardiac cycle.

2.4 Discussion

While the normalization of Q and λ_2 methods helped to reduce the impact of varied analytic thresholds on vortex characteristics quantified by the identification of critical points in flow, these methods were still subject to limitations. Such methods are susceptible to both incorrect identification of vortex areas and generating disjointed and/or highly fragmented vortex *iso-surfaces*. These limitations may alter the assessed characteristics of vortex size and spatiotemporal stability. Additionally, estimated parameters based on velocity field derivatives can be significantly influenced by noise levels [129], making a vortex identification methodology solely reliant on calculated derivatives (i.e. critical point methods).

The developed CE method overcomes some of the inherent shortcomings of relying solely on critical point analysis. First, Shannon's entropy takes stock of the directionality of flow velocity vectors within an area as a means to assess patterns, gaining a degree of protection from small scale flow changes. Second, the CE method is not solely reliant on assessment of velocity vector gradients, which are susceptible to noise in imaging data. The analysis of a broader area of the flow field shields not only identifies the structure of vortices beyond their center-most points thus giving more comprehensive information concerning vortex characteristics. It is worth noting that, while ROI sizes significantly impact the resultant volume of vortices, changes to vortex spatial temporal stability (DVO) are less susceptible to ROI size. Across the 10 cases analyzed, only 3 cases showed statistical decreases in DVO as an inverse of ROI size. While there are statistical differences between the quantified spatial temporal characteristics of vortices identified by the normalized Q-criterion and CE method, with CE vortices being larger and more spatially stable, the spatial locations of identified vortices were similar between methods. These initial findings suggest that the developed CE method identifies analogous area(s) of flow vortices recognized by more long-standing critical-point methods.

2.5 Conclusion

The developed CE method was found to be more robust than critical-point based methods when quantifying vortex spatial stability across varied data resolutions and methodical thresholds. Having an analytical method that is able to both overcome the limitations inherent to solely critical-point analysis and evaluate a broader aspect of vortex characteristics can help lead to novel information that may prove essential for identifying conditions indicative of IA development and rupture. For the remainder of this dissertation, the developed CE method will be implemented during any identification and quantitative analysis of flow vortices.

2.6 Acknowledgements

This work is partially supported by a research contract from Siemens Medical Solution USA, Inc., to Michigan Technological University and the Research Excellent Fund from Michigan Technological University. The authors also want to thank their colleague Professor Charlie Strother, M.D.degree holder, from the University of Wisconsin-Madison for supplying some DSA data used for this study and Dr. Thomas Redel from Siemens Healthcare Inc. for technical support.

Chapter 3

Vortex Analysis to Improve Prediction of IA Initiation

In much of the human vasculature, blood flows in a laminar, mostly unidirectional pattern. Yet investigations into the nature of IAs uncovered their non-random distribution in areas of the vasculature susceptible to disturbed flow: vessel bifurcations or areas of significant vasculature curvature [118, 210, 237]. While such areas of the vascular geometry are prone to IAs, the majority of the populace never develop an IA in said areas. To understand this discrepancy, studies have attempted to elucidate the conditions indicative of IA development that exist within these areas [55, 172, 311]. A specific area of focus is on the role of complex vascular hemodynamics and how they may be indicative of IA growth[195, 289]. Such studies have helped to understand

the roll of the tangential fluid stressors, wall shear stress (WSS), impacting changes to the vascular wall. In areas of the cerebral vascualture (prone to IA development) WSS outside physiological ranges ($\sim$ 15 - 30 dynes/cm^2) or elevated WSS gradients (high rates of WSS change at a distance for a given point in time) are associated with IA development [6, 8, 48, 61, 89, 264]. However, in many of these studies, only the correlation of WSS metrics to IA initiation sites were evaluated. Heightened areas of hemodynamic stressors are not wholly specific to IA areas, and not all areas of heightened WSS gradients develop IAs. Limited specificity may reduce any single index's effectiveness to predict IA initiation, generate false positives, and could account for inconsistencies among study findings [192, 218, 297]. Additionally, WSS indexes only assess near-wall hemodyanmics, giving minimal insight to bulk flow characteristics within the vessel. Failure to quantify hemodynamic vortex characteristics overlook metrics that may prove beneficial to the identification of areas at high risk of IA development. To address this limitation, the analysis of vortices using the CM method was applied alongside WSS metrics to assess areas of eventual IA development. The objectives of this aim were twofold. First, assessment of indices in both areas of known IA development and nearby areas of no known IA development was performed to improve the understand of indices' relationship to IA initiation. Second, determine whether or not combining vortices identified using the developed CE method alongside near-wall hemodynamic indexes could improve the accuracy of predicting IA initiation. As an additional means of strengthening this work, clinical

data containing taken from patients with 2-4 closely-spaced side-wall IAs located at the Internal Carotid Artery (ICA) were used so that multiple IA sites can be identified in the same vessel. To our knowledge, minimal work has been done in terms of predicting the initiation of multiple ICA IAs.

3.1 Materials and Methods

3.1.1 Data-set

Since pre-aneurysm vascular geometries are scarce, a published computational geometry-based surface reconstruction method was adopted to recreate said geometries from patient medical imaging data [110]. Flow in and around sites of eventual IA formation was generated using these pre-aneurysm geometries in conjunction with "patient-specific" computational fluid dynamics (CFD) simulations, similar to methodologies adopted within other studies [61, 110].

From an internal database of 3D-DSA based on patient angiographic images data obtained from standard clinical equipment, 18 subjects were identified who had multiple closely-spaced sidewall IAs located within the supra-clinoid segment of the ICA. This data set was aggregated using scans from the University of Wisconsin and Changhai

Hospital (China), and was exempt by Michigan Technological University's institutional review board as it was a secondary analysis of existing data sets.

3.1.2 Model Creation

Vascular geometries were extracted from patient's medical imaging data in an identical fashion as mentioned in section 2.1.1. Once all vascular geometries were obtained and edited (i.e smoothed, removal of extraneous vascualture, etc), 2 groups of models were created: one with all IAs computationally removed from the vessel (Model A), and the other with one IA intact (Model B). As vascular pathology may alter hemodynamics [135, 323], the initial formation of one IA may disturb localized flow, impacting the initiation of subsequent IAs. Model B data aimed to address this concern, and was considered an additional benefit of this work. To create Model A, the following process was used. First, a semi-automated IA removal method [110], implemented in VMTK, removed all IAs and reconstructed the IA-free vessel geometry. Next, the IA-free geometry was imported into the 3-Matic software program and the geometry was projected onto the original vessel to remove unintended alterations to parent vessel curvature that may occur during IA removal. Geometries were then smoothed to remove surface irregularities. For Model B, the 3-Matic software was used to re-attach one IA back onto a copy of the Model A vasculature. When the vascualture contained tandem IAs, two IAs with distinct separation of their ostia

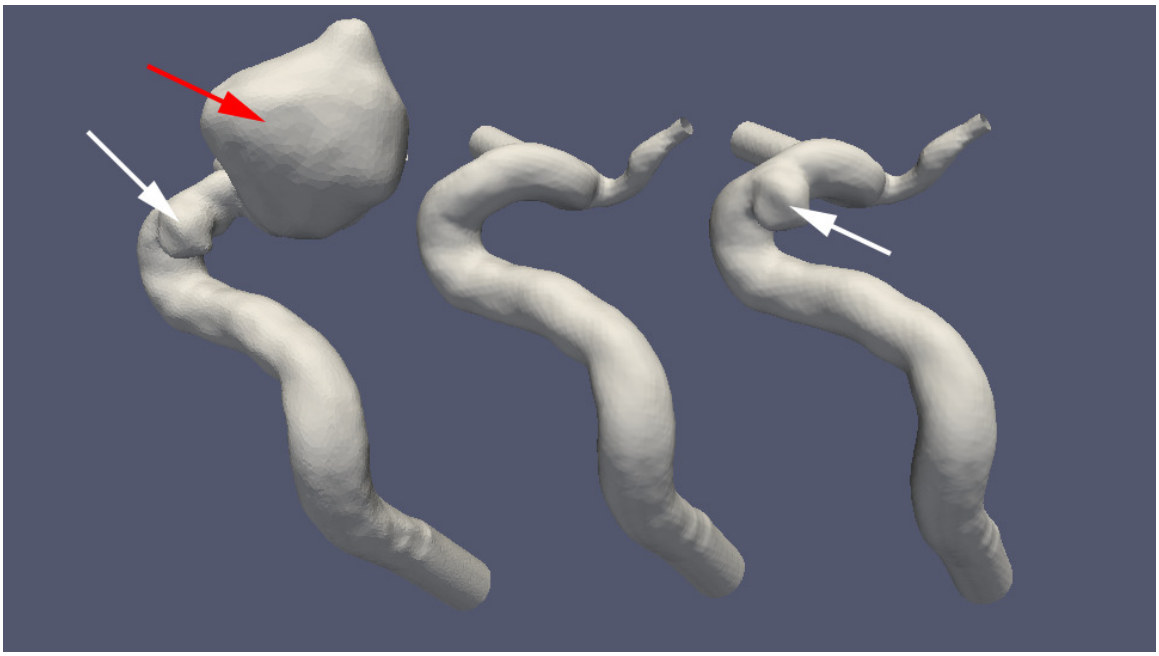

Figure 3.1: Vascular model with all IAs intact **(left)**, both IAs computationally removed: Model A **(center)** and 1 IA reattached: Model B **(right)**. Arrows identify the vessel IAs: white identifying the reattached proximal IA, red identifying the distal IA.

along the longitudinal axis of the parent vessel, the proximal IA was kept intact. For adjacent IAs with their two IAs opposite each other on the transverse axis of the parent vessel, two Model Bs were generated, each with one of their IAs intact. An example of an original vessel and their resultant Model A and B can be seen in Figure 3.1. All models were converted into an unstructured, 3D volumetric mesh using the open-source mesh generator Tetgen via VMTK [300]. Approximately, 1 million computing cells were used per case, with an approximate cell volume of 0.003mm^3.

3.2 CFD Simulations

Flow within the the created vascular models was simulated by numerically solving the Navier-Stokes equation in the ANSYS-FLUENT software package, using the Gwilliam waveform as the flow inlet boundary condition in a similar manner to that in Section 2.1.3. Additionally, as a differing waveform may impart alterations to the expression of hemodynamic indexes, four (4) randomly selected cases were re-run with a waveform from retrospectively gated phase contrast magnetic resonance images of older adults (age 68 $\pm$ 8 years) by Hoi et al. [144]. Figure 3.2 shows both the Gwilliam and Hoi waveform. These 4 cases were compared to their Gwilliam waveform counterparts. All simulations had their flow waveform scaled to the vessel's inlet cross-sectional area, standardizing the mean volumetric flow rate to 280mL/min or 240ml/min for the Gwilliam and Hoi waveforms respectively. Four cardiac cycles were simulated with 1000 time-steps per 1 second cardiac cycle. Twenty equally-spaced time points were saved from the final cardiac cycle for data processing and analysis and four randomly selected cases were re-run and sampled at forty equally-spaced time points to assess the impact on calculated indexes.

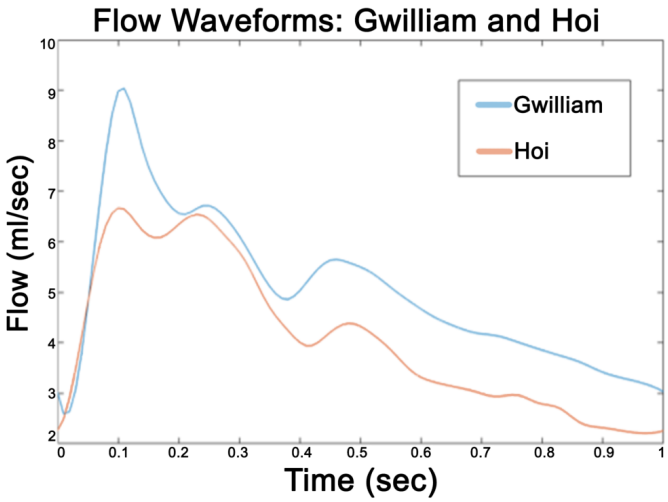

Figure 3.2: Wave forms of human vascular flow rates at the internal carotid artery used as inlet boundary conditions for fluid dynamic simulations: taken from Gwilliam[128] and Hoi[144]

3.2.1 Calculation of Hemodynamic Indexes

The following parameters were calculated from simulated flow data as they have been linked with increased IA formation: WSS, WSS Gradient (WSSG), Oscillatory Shear Index (OSI) [140], Aneurysm Formation Indicator (AFI) [218], and Gradient Oscillatory Number (GON) [298]. Additionally, the mean number of flow vortices, identified using our CE method, was calculated and tested to determine their impact on prediction outcomes.

The ANSYS-FLUENT software calculated WSS via normal velocity gradient at the vessel wall:

$$\tau_{\mathrm{w}} = \mu \frac{\partial v}{\partial n} \tag{3.1}$$

where μ is the dynamic viscosity. WSS is known to regulate endothelial structure, function, and gene expression in the internal carotid artery of the cerebral vasculature[154, 245].

The calculation of WSSG was taken from methods used in the literature [244, 297]. We assume that the vessel wall is represented by a set of surface triangles: given an arbitrary triangle whose surface normal is n, τ, a function of WSS, locally resides in a plane perpendicular to n. Mathematically, two orthogonal vectors p and q lie within the plane can be constructed as follows: p is the flow direction at time t and q is perpendicular to p and n. Thus, the WSSG is computed by taking local derivatives of the WSS magnitude over the p and q directions for a given time instant t [244].

The WSSG was calculated using in-house VMTK scripts and is calculated as followed:

$$\begin{aligned} WSSG &= \sqrt{(\frac{\partial \tau_p}{\partial p})^2 + (\frac{\partial \tau_q}{\partial q})^2} \\ \frac{\partial \tau_p}{\partial p} = \nabla \tau \cdot \alpha, \frac{\partial \tau_q}{\partial q} &= \nabla \tau \cdot p, p = \frac{\tau}{|\tau|}, q = n \times p \end{aligned} \tag{3.2}$$

with the time-averaged WSSG calculated as

$$WSSG_{\text{av}} = \frac{1}{T} \int_0^T |WSSG| dt \tag{3.3}$$

where the gradient operator $\bigtriangledown$ denotes partial derivatives of the magnitude of τ in its coordinate directions. If the flow direction p in Equation 3.2 becomes an average

flow direction over the cardiac cycle then the instantaneous spatial vector of WSS, $G = (\frac{\partial \tau_p}{\partial p}, \frac{\partial \tau_q}{\partial q})$, can be used to calculate the GON metric, which reflects oscillations in the directionality of spatial gradients of WSS over the cardiac cycle:

$$GON = 1 - \frac{|\int_0^T G dt|}{\int_0^T |G| dt} (0 \leq GON \leq 1) \tag{3.4}$$

T is the period of the cardiac cycle.

OSI is a nondimentional parameter, computing oscillations in WSS vector directionality over the course of the cardiac cycle:

$$OSI = 0.5 \times \left\{ 1 - \frac{|\int_0^T \tau_i dt|}{\int_0^T |\tau_i| dt} \right\} \tag{3.5}$$

were τ_{i} represents the WSS vector at a given time step across the duration of the cardiac cycle (T). The OSI describes the changes of a WSS vector's alignment with the cardiac cycle's temporally-averaged WSS vector. An OSI of 0 indicates no change in directionality and 0.5 being a complete direction reversal.

AFI quantifies the variation in angle between the instantaneous WSS vector at a point and its time-averaged WSS vector:

$$AFI = cos(\theta) = \frac{\tau_i \cdot \tau_{av}}{|\tau_i| * |\tau_{av}|} \tag{3.6}$$

For each point along the vessel wall, the minimum AFI calculated during the cardiac cycle was used to indicate the greatest deviation of the WSS vector from its mean direction. A minimum AFI of -1, 0, and 1 indicate deviations of 180°, 90°, and 0°respectively.

The spatially averaged value of aforementioned indexes was identified within the areas of known IA growth as well as in regions of interest (ROIs) with no known IA initiation. Due to the limited specificity of indexes to IA areas, nearby ROIs with no known IA initiation acted as a negative control for statistical analysis and predictive modeling. An example of calculated indexes within areas of IA initiation and IA areas absent of calculated indexes can be seen in Figure 3.3.

3.2.2 Regions of Interest

For areas containing IA sites, ROIs of vessel segments spanning the area(s) of the removed IA's ostium were chosen. For ROIs of non-IA initiation, three vessel segments for each patient case were chosen. The length of each non-IA ROI equals the cross-sectional diameter of their parent vessel(proximal to the first identified IA). Two non-IA ROIs were chosen in tandem, proximal to the site of the first formed IA, while the third was chosen immediately distal to the site of the last IA. In the event that the third ROI encountered a vessel bifurcation, it was instead chosen directly

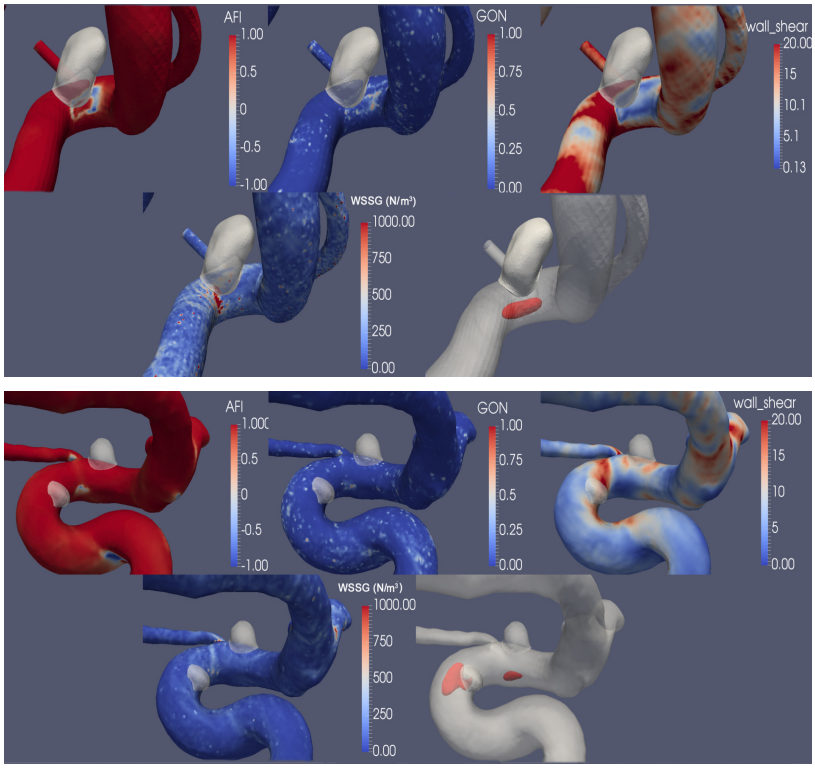

Figure 3.3: Simulated flow showing elevated hemodynamic indexes (or reduced AFI) **(top)** or reduced indexes (or increased AFI) **(bottom)** at areas of IA initiation: AFI, GON, WSS, WSSG. An identified vortex did occur within one (of two) sites of IA initiation

proximal to the first two ROIs. All non-IA ROIs were divided laterally, and each side investigated individually as stressors are not uniform around the vessel wall [196]. The division plane for non-IA ROIs was selected in relation to the Frenet Frame normal of the vessel centerline tangent. The Frenet normal, defining the oscillating plane of curvature at the midpoint of each ROI centerline was chosen for respective cut planes. Examples of ROIs and chosen cut planes can be seen in Figure 3.4.

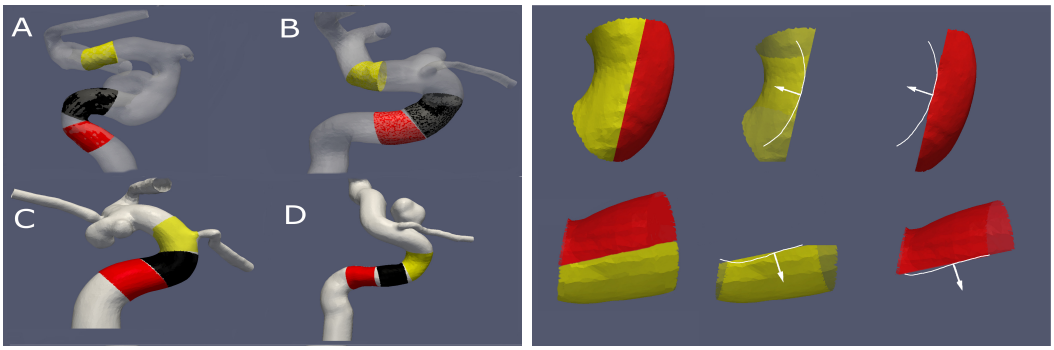

Figure 3.4: Examples of ROIs for no IA development. **(Left)**: ROIs were either chosen with two proximal to the first IA and one distal to the last IA (A and B), or all three ROIs proximal to the first IA (C and D). **(Right)**: ROI division in relation to the vessel Frenet Frame normal (yellow) and opposite (red). The white line is the centerline following vessel curvature, with the arrow pointing to normal.

3.2.3 Statistical Analysis

The mean values of WSS, WSSG, OSI, GON, and AFI along the ROIs and flow vortices were determined within all ROIs. Prior to predictive modeling, the correlation amongst variables was performed to eliminate redundant variables and subsequent over-fitting in models. Multivariate logistic regression analysis (step-wise elimination) was then performed to identify index combinations significant in predicting IA initiation. Model B was assessed separately from IA-free models (Model A). Using Model B, how the presence of one proximal IA impacts predictive outcomes was evaluated, which could give much needed insight toward how multiple IAs alters flow characteristics indicative of future IA development [365].

The model(s) derived from multivariate logistic regression were tested using repeated k-fold cross-validation (10 folds, 10 repeats). The area under the receiver operating characteristic curve (AUROC) assessed grouped indexes as well as each variable individually to determine their strength towards predicting IA initiation. Statistical analyses were performed using the R statistical platform (Version 3.4.4).

Explanation of logistical regression analysis and receiver operating characteristic curves can be seen in Appendix A

3.3 Results

Correlation analysis among study indexes showed AFI and OSI as highly correlated (cor=0.92, $p<0.001$). These indexes both relate alterations of WSS vector directionality, giving grounds for their correlation. OSI was removed from subsequent analysis.

The correlation of spatial means of hemodynamic indexes to the occurrence of an IA within all analyzed ROIs was assessed (Table 3.1). Our findings showed a lack of strong correlative relation of area of known IA development to indices, stressing the need of grouped parameters to improve predicative models.

Table 3.1
Pearson's correlation (and p-value) of mean of hemodynamic variables within all regions of interest to the occurrence of an IA: Model A and Model B data.

Variable	Correlation:p-value	Variable	Correlation:p-value
Model A		**Model B**	
AFI	-0.190 : 0.022	AFI	-0.170 : 0.021
WSS	0.333 : < 0.001	WSS	0.309 : < 0.001
WSSG	0.241 : 0.004	WSSG	0.177 : 0.016
GON	0.221 : 0.008	GON	0.207 : 0.005
Flow Vortex	0.477 : < 0.001	Flow Vortex	0.381 : < 0.001

Step-wise multivariate logistic regression identified the index combination best suited (from available data) to identify areas of IA initiation. In Model A, combining mean number of vortices (MV), WSS and GON acted as the strongest parsimonious model for predicting IA formation (Eq3.7). It is worth noting, mean GON values were found to by highly right-skewed, with small values. The log transform of GON means was taken to lower its weight on odds ratios and improve prediction models. The odds ratio(s) of the chosen hemodynamic indexes show that the occurrence of flow vortices increase the odds of the IA initiation by 14.34 times, elevated log transformed GON increasing the odds by 6.45 times, and elevated WSS increasing odds by 1.33 times.

$$Odd_{NoIA} = exp^{2.66*MV+1.864*GON+0.286*WSS+0.938} \tag{3.7}$$

Repeated k-fold cross-validation with the combined MV+GON+WSS model showed the strongest outcomes (AUROC 0.879, 95% CI 0.821-0.942) over any individual index. ROC curves from model outcomes can be seen in Figure 3.5.

Similar analysis was performed on Model B data, assuming development of the attached IA impacted subsequent flow characteristics in areas of distal IA formation. K-fold cross-validation of Model B data, using Model A indexes (MV+WSS+GON), showed a slight reduction in predictive outcomes: AUROC 0.879 and 0.824 (CI 0.737-0.912) for Model A and B, respectively: Figure 3.5. Model B's analysis determined the combination of MV+WSSG+GON indexes still created the parsimonious model, yet the impact of each index was altered. The odds ratio for Model B based on the MV+WSS+GON prediction was:

$$Odd_{1IA_{MV+WSS+GON}} = exp^{1.789*MV+1.69*GON+0.219*WSS+0.888} \tag{3.8}$$

It was unclear if the change in outcomes arose from one of the IA ROIs no longer being analyzed, or Model B's remaining IA altering flow characteristics. To assess if outcomes between Model A and B were attributed to altered hemodynamics, a secondary analysis of Model A data was performed where ROIs coinciding with the area(s) of IA reattachment (in Model B) were excluded, eliminating their impact on outcomes. Subsequent k-fold cross validation with the MV+WSSG+GON predictive model was performed for the secondary analysis of Model A data.

Secondary analysis of Model A data showed similar predictive outcomes to Model A's original analysis: AUROC of 0.883 (CI: 0.806-0.958) and 0.879 respectively. Yet the

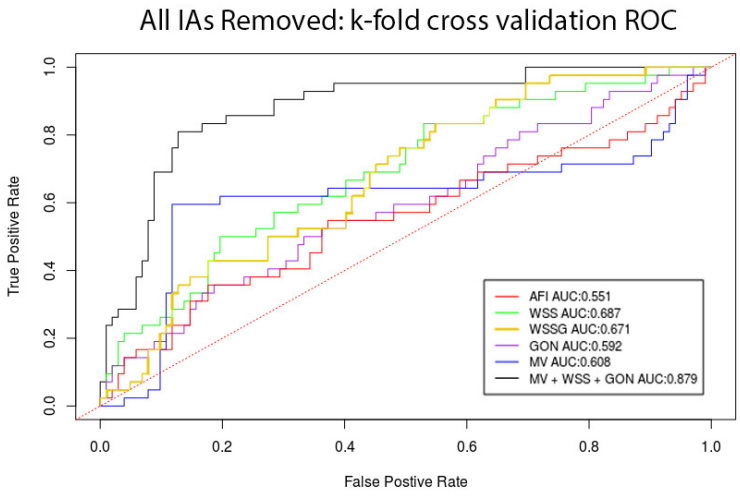

(Model A)

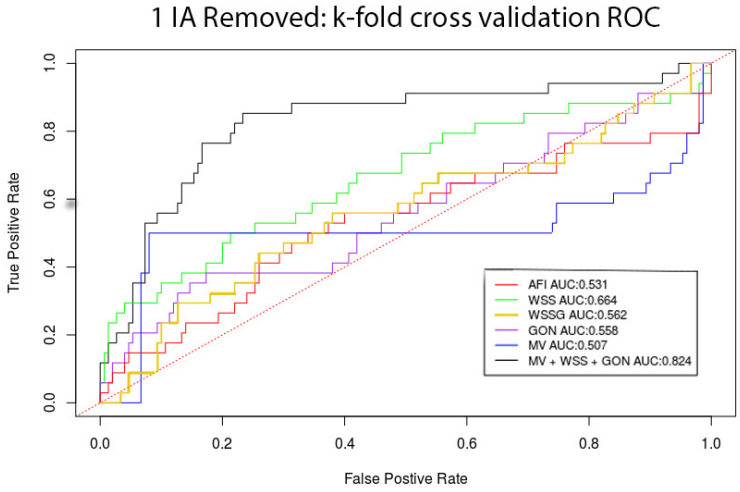

(Model B)

Figure 3.5: ROC curves of averaged prediction probabilities from repeated k-fold cross-validation of regression modelling. The AUROC values of individual indexes were assessed (AFI, WSS, WSSG, GON, and MV) as well as the parsimonious combined model (MV+WSS+GON). **Top**: Model A, **Bottom**: Model B.

strength of GON marking an almost 2 fold increase in its odds ratio: 6.45 to 11.665 original vs secondary analysis respectively. Table 3.2 shows the odds ratios of indexes under differing analyses.

Table 3.2
Odds ratios of predictive indexes for the analysis of Model A (A1), secondary analysis of Model A (A2), and Model B data (B). Analysis was performed with the MV+GON+WSS indexes in predictive models. Values in red indicating marked differences in index strength in relation to the A1 Model.

Model	MV	GON	WSS
A1	14.34	6.45	1.33
A2	10.49	11.67	1.39
B	5.98	5.42	1.25

Quantified hemdoynamic indices were also assessed under altered simulation conditions were to determine if significant differences occurred as such differences could impact prediction outcomes. Table 3.3 shows that significant alterations to indices between chosen waveforms, while mesh density had no significant impact. Alterations in time-steps (data sampling rate) had no significant impact on AFI or GON values, but did lead to alterations on WSS and WSSG values. In terms of impact on vortices, Figure 3.6 shows the spatial similarities of between simulations run with the Gwilliam waveform, Hoi waveform, and run with both a dense and less dense mesh, all sampled at 20 time-steps per cardiac cycle. Additionally, Figure 3.6 shows the sampling rate's impact on vortices, comparing simulations run with the Gwilliam waveform on the denser mesh at a 40 and 20 time-step sampling rate. Finally, changes to the temporally-averaged volume of vortices, in areas of eventual IA development, were compared between the four simulation conditions (Figure 3.8), with only a slight reduction (not-significant) change in vortex size when using the Hoi waveform compared

Table 3.3
Percent change to hemodynaimc indexes in ROIs under varied simulation conditions. Paired t-test was performed to determine statistical significance of change.

Comparison	**AFI** %Change p-value	**WSS** %Change p-value	**WSSG** %Change *p-value*	**GON** %Change p-value
Waveform:	-12.6%	-10.14%	-46.9%	114.60%
Gwilliam vs Hoi	<0.001	<0.001	<0.001	<0.001
Mesh Density:	-0.13%	-2.39%	-6.47%	4.98%
1.5 vs 6 million cells	0.862	0.08	0.09	0.44
Time-steps:	0.98%	-10.52%	-50.03%	0.201%
20 vs 40 per cycle	0.01	<0.001	<0.001	0.92

to the Gwilliam waveform.

3.4 Discussion

Reliance on assessing near-wall WSS to determine areas indicative of IA formation have shown to vary in their success [120, 218, 228, 280, 297]. Furthermore, indices are often only individually correlated only with areas of known IA development [61, 218]. This gives a restrictive appraisal of conditions indicative of this vascular pathology as heightened expression of hemodynamic stressors are not wholly specific to areas of IA formation. Assessment of areas of both known and no known IA development showed minimal correlation to WSS indices, stressing the importance of adopting a

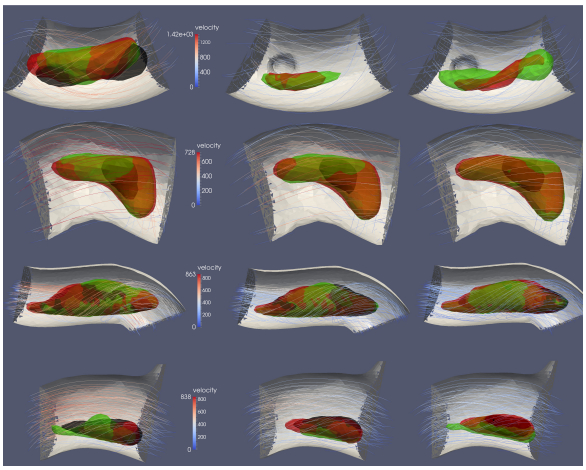

Figure 3.6: Vortices identified **(Red):** Gwilliam waveform, lower mesh density vs **(Green):** Gwilliam waveform, higher mesh density (20 time-step sampling rate) vs **(Black):** Hoi waveform, lower mesh density. Columns representing vortices at the 2nd, 10th and 15th cardiac cycle data point.

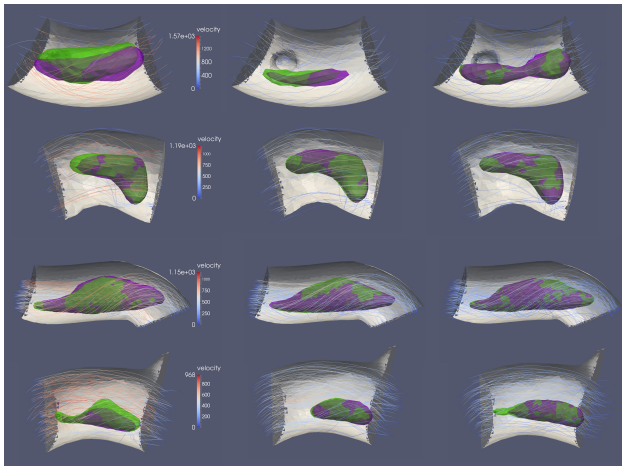

Figure 3.7: Vortices identified at 20 time-step **(Green)** and 40 time-step sampling rate **(Purple)** over the cardiac cycle. Columns represent vortices taken at three-equivalent time-points over the cardiac cycle.

multivariate approach to predictive modelling and analysis. Said near-wall indices overlook bulk flow hemodynamic characteristics which may play a role in IA development. The addition of our CE method for identifying vortices aimed to improved the prediction of IA initiation by analyzing the relationship of vortices to IA development. These results demonstrated that combinations of near-wall and bulk flow

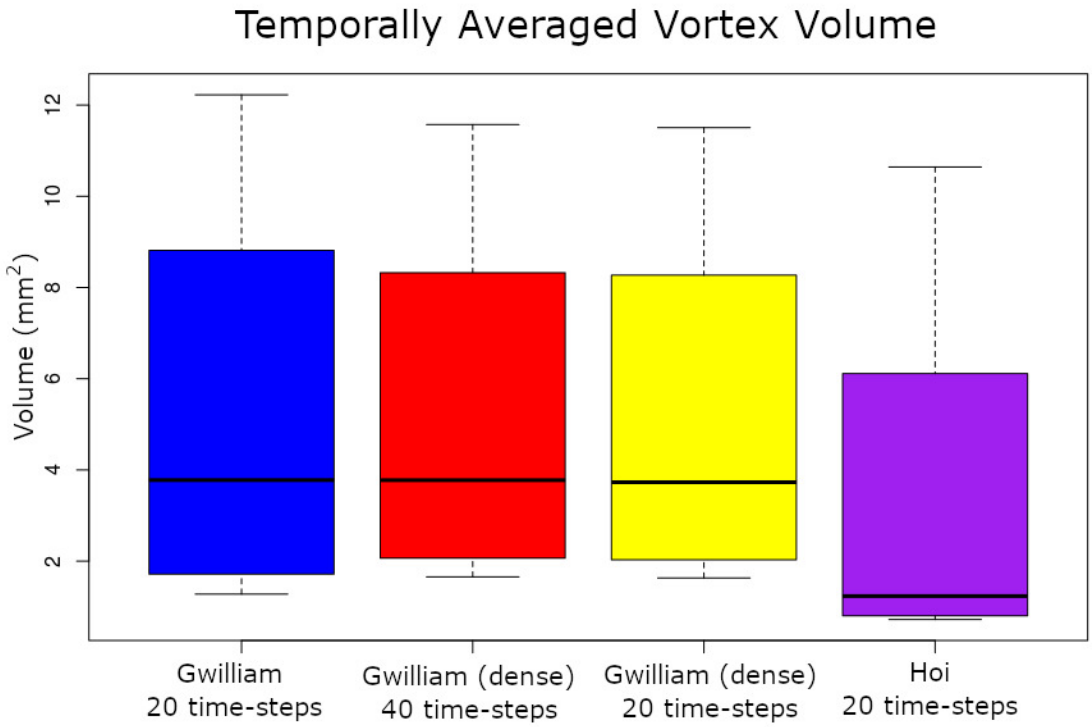

Figure 3.8: Temporally-averaged vortex volume in four randomly selected cases run under varied simulation parameters: **(Blue)**Gwilliam waveform, lower mesh density (20 time-steps), **(Red)**Gwilliam waveform, higher mesh density (40 time-steps), **(Yellow)**Gwilliam waveform, higher mesh density (20 time-steps), and **(Purple)**Hoi waveform, lower mesh density (20 time-steps).

hemodynamic variables, specifically WSS, GON and vortices, improved the accuracy of predicting areas of IA formation as indicated by the elevated AUROC in relation to individual indexes. The adoption of WSS, GON and vortices into a predictive model is supported by ideas that alterations in flow patterns and increasing shear stress impact vascular endothelial cells [131] and could impact IA initiation [340]. Analysis showed that the application of vortices applied alongside known GON, and elevated WSS improved the strength of IA prediction. The almost two fold increase

in GON's impact on prediction models between Model A and its secondary analysis suggests that the flow vortices may trigger oscillating compression and tension forces in the downstream vasculature, increasing the possibility of IA development [297]. The secondary analysis of Model A data made no distinct change to the impact of WSS on prediction models. Understanding conditions that impact IA prediction and development may benefit from leaving additional IAs intact and noting subsequent changes to hemodynamics and predictions.

The presence of a singular IA has been shown to alter the localized hemodynamics [319] and such changes may propagate downstream in the vasculature. An evaluation of Model B (one IA intact) data showed that while alteration to the localized flow did not change the indexes needed for the prediction model, it did alter each indexes' predictive strength. The introduction of one IA into the vasculature altered local flow conditions, reducing the odds ratio of both vortices (10.49 to 5.98) and GON (11.66 to 5.42) on IA prediction.

Assessment of hemodynamic indexes generated using differing inlet waveforms showed marked changes. The Hoi waveform resulted in a 60.9% reduction in vortex volume in relation to the Gwilliam waveform. Additionally the Hoi waveform lead to a reduction in WSS, AFI, and WSSG values, and an increased GON, while maintaining a degree of visual spatial consistency between indices generated by the Gwilliam waveform. The changes to variable values was expected due to the lower volumetric flow rate

in the Hoi waveform, coupled with its depressed peak amplitude. As both risk of IA generation increases as a function of age [17] and characteristics of cardiac waveforms vary across ages, a larger study using vascular models from patients of known age (not available for this work) alongside an age appropriate waveform may help lead to a clearer understanding of indices' impact on predictive models. Spatial intensities of the near-wall hemodynamic indices and vortex volume had minimal change when analyzed under varied mesh density and sampling rate: percent difference 12.4% and 1.2% respectively.

It is worth noting, the hemodynamic variables were only assessed based off a patient's overall vessel geometry at a single given time-point. As no information was available concerning their vessel geometry prior to IA development, certain assumptions had to be made for this study. Both the choice of IA maintained (the proximal IA kept for Model B simulations), and that the overall curvature in the internal carotid siphon did not change significantly post-IA development were assumed. In order to better validate predictive models, a continuous longitudinal study of patients would need to be conducted, assessing possible changes to both vessel curvature and temporal order of IA development.

3.5 Conclusion

IA formation is a multi-faceted vascular pathology, with varying conditions impacting their development [302]. A comprehensive analysis of near-wall and bulk-flow hemodynamic indices applied to predictive modeling could help elucidate patients at risk for developing an IA more-so than just the near-wall flow characteristics. Increased WSS intensity and fluctuations, coupled with the presence of complex swirling flow patterns indicate area(s) with a higher possibility of IA development. While the adaptation of hemodynamic vortex analysis has shown to be beneficial in the identification of areas of likely IA development, this work gives no insight to the usefulness of hemodynamic indices to assess the severity of (developed) IAs. Further analysis of the hemodynamic patterns in resultant IAs was performed in Chapter 5 to help overcome this limitation.

3.6 Acknowledgements

The study was partially funded by a research contract through Siemens Medical Solution (USA) Inc. Kevin Sunderland is currently supported by a pre-doctoral fellowship from the American Heart Association [18PRE33990321].380 No funding sources had any role in the collection, analysis, or interpretation of study data. We also thank

our colleagues, particularly, Dr. Charles Strother (University of Wisconsin) and Dr. Qinghai Huang (Changhai Hospital) for providing us the data used in this study.

Chapter 4

Two closely-spaced Aneurysms of the Supraclinoid Internal Carotid Artery: How Does One Influence the Other?

Of patients who suffer an aneurismal subarachnoid haemorrhage, 15-35% of cases present with multiple IAs [99, 277, 350]. In many of the multiple IA cases, two aneurysms occur on the same section of the parent artery; these we have defined as closely-spaced aneurysms. When multiple IAs are detected, a clinical management decision may result in the surgical treatment of only one IA with subsequent treatment(s) onremaining IAs at a later time or not at all. Yet in a study study by Ferns [108], PC-MRA imaging suggested that in a closely-spaced IA situation, once one IA

was treated, the remaining IAs may grow.

To better understand the risks associated with multiple IAs, both Jain [155] and Crompton's [78] clinical observations found that the first (proximal) IAs in a paired IA system had a higher chance to rupture. In an attempt to understand the factors behind proximal aneurysm's higher risk of rupture, Jain studied rubber aneurysm phantoms placed into a pulsatile flow circuit and observed that in distal aneurysms there was a decrease in pressure variation as compared to that in the proximal aneurysm [155]. Very recently, Jou and Britz represented a CFD case study where the computer-simulated hemodynamics of eight small IAs (< 7 mm) from one patient were analysed [166] to better understand the hemodynamic characteristics within multiple IAs. Yet these studies give no indication into how an individual IA impacts subsequent IAs within the same vessel. To our knowledge, while a few studies have looked into how the the occlusion of flow into a proximal IA impacts subsequent near-wall hemodynamic characteristics in any distal IAs[325], less is known of the impact on bulk-flow characteristics within the non-repaired IA.

Using currently available CFD techniques in association with "patient-specific" geometrical models, an expansion on observations made by early studies was performed. The goals of this project were the following: **First)**, to identify those hemodynamic features that might be particular to two closely-spaced IAs; and, **Second**, to identify

the hemodynamic impacts of one IA onto the other. The second objective was investigated using modified geometrical models in which one of two closely-spaced IAs was computationally removed. Quantitative metrics were selected to evaluate hemodynamic features: kinetic energy density(KED), wall shear stress(WSS), oscillatory shear index (OSI) flow vortex degree of volume overlap (DVO) using the developed CE methodology. WSS and OSI are indications of the near-wall stressors placed upon the aneurysm, KED indicates the energy within a system, and the vortex DVO allowing for the quantification physiological flow stability. Assessment of these indices could give insight to how conditions within an IA are altered in the event of the surgical repair of another nearby IA.

From an internal database combining medical imaging data from University of Wisconsin (USA), Changhai Hospital (China) and a public database[1], 15 subjects were identified who had at least two closely-spaced IAs located at the supra-clinoid segment of the ICA. All IAs were known to have been unruptured at the time of patient imaging. The study was exempted by the institutional review board (IRB) at the Michigan Technological University as this study was a secondary analysis of the existing data. Vascular structures were separated into one of two groups dependent on the degree of ostium overlap between IAs: adjacent or tandem. Adjacent IAs (AA) were defined as two IAs whose ostiums were directly opposite each other on the transverse axis of the parent vessel, while tandem IAs (TA) were defined as two IAs with

[1]http://ecm2.mathcs.emory.edu/aneuriskweb/index

a distinct separation (no ostium overlap) along the longitudinal axis of the parent artery. This separation resulted in 8 patients with adjacent IAs and 7 patients with tandem IAs. The appearance and basic geometrical parameters of these aneurysms are shown in Figure 4.1 and Table 4.1 respectively.

4.1 Methods

Vascular geometries were extracted from patient's medical imaging data, and volumetric meshes were made in an identical fashion as in section 2.1.1. For each subject in the AA group, three meshes were created: one with both IAs present (Model A), and two meshes with one of two IAs removed (Model B). In the TA group, two meshes were created for each subject: one with both IAs present (Model A) and the other with no proximal IA (Model B).

In order to create Model B meshes, the method for IA removal / reattachment used in Chapter 3.1.1 was employed. All vessel surface geometries (Models A and B) were converted into a unstructured, 3D, tetrahedralized volumetric mesh with approximately, 1 million computing cells were used per case, resulting in approximately 0.003mm^3 cell volume.

Vascular blood flow patterns, flow velocity and WSS values were calculated using the

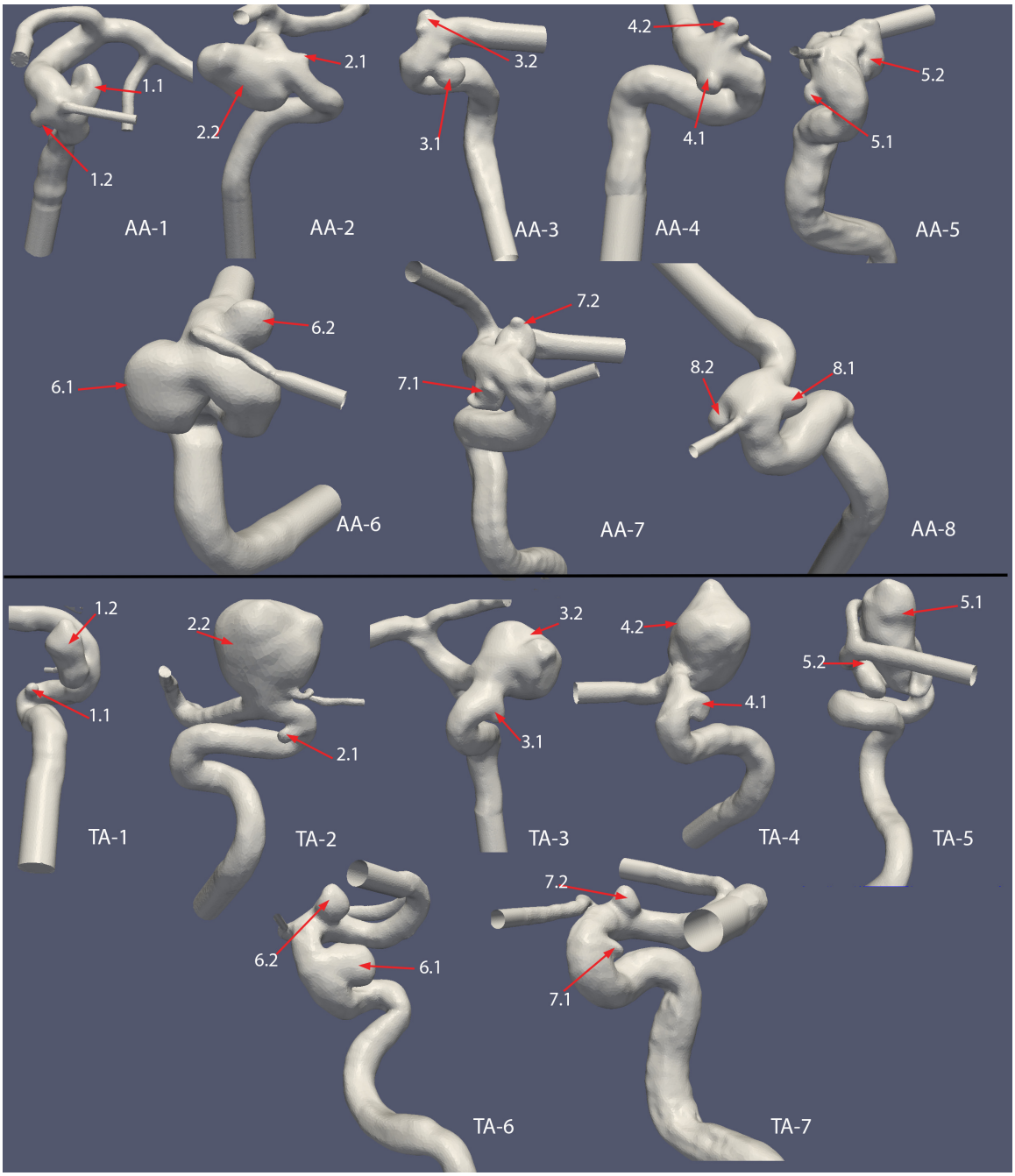

Figure 4.1: Vascular models of closely-spaced, multiple ICA IAs in 15 subjects. In each model, arrows point to IAs. Each IA is label following the same convention: group, case number and IA number. For instance, AA-1.1 stands for the first aneurysm in the case 1 of the Adjacent IA group.

Table 4.1
Geometric Characteristics of IAs: Volume, Ostium Area, Aspect Ratio, IA Diameter, and Parent Vessel Diameter

Case	Vol. (mm^3)	Ost. Area (mm^2)	Aspect Ratio	Diameter: IA(mm)	Vessel Diameter (mm)
AA1.1	45.14	14.19	1.11	4.42	3.98
AA1.2	5.56	6.61	0.55	2.12	3.98
AA2.1	2.69	6.44	0.55	2.09	3.91
AA2.2	322.92	33.72	1.22	8.51	3.91
AA3.1	42.740	11.14	1.09	4.34	4.84
AA3.2	21.68	12.99	0.65	3.46	4.84
AA4.1	23.38	17.14	0.59	3.55	5.36
AA4.2	14.59	9.62	0.75	3.03	5.36
AA5.1	9.35	7.71	0.68	2.61	5.31
AA5.2	71.65	7.76	1.61	5.14	5.31
AA6.1	211.82	20.21	1.41	7.40	4.87
AA6.2	27.47	11.81	0.85	3.74	4.87
AA7.1	31.70	15.25	0.91	3.93	4.66
AA7.2	89.19	20.89	1.16	5.54	4.66
AA8.1	16.55	13.01	0.67	3.16	4.50
AA8.2	25.02	17.10	0.60	6.63	4.50
TA1.1	6.75	4.90	1.19	2.34	4.17
TA1.2	7.98	2.24	1.81	3.81	3.65
TA2.1	6.13	4.45	0.98	2.27	3.58
TA2.2	1185.90	34.44	1.95	13.13	3.86
TA3.1	4.96	7.03	0.55	2.12	3.67
TA3.2	356.10	22.14	1.58	8.79	3.98
TA4.1	24.48	14.40	0.63	3.60	4.19
TA4.2	1116.11	21.05	2.85	12.87	4.72
TA5.1	1083.49	42.76	2.07	12.74	5.37
TA5.2	62.38	21.30	1.85	3.45	5.43
TA6.1	111.46	31.76	0.83	5.97	5.05
TA6.2	185.27	14.91	1.02	7.07	5.12
TA7.1	7.04	8.00	0.59	2.38	4.81
TA7.2	19.67	11.49	0.7	3.35	5.22

ANSYS-FLUENT software (v14.0 ANSYS-FLUENT Inc., Lebanon, NH) in the same manner as in 2.1.3. The inlet waveform for all cases was taken from Gwilliam et. al [128], with each case's volumetric flow rate scaled to 280mL/min.

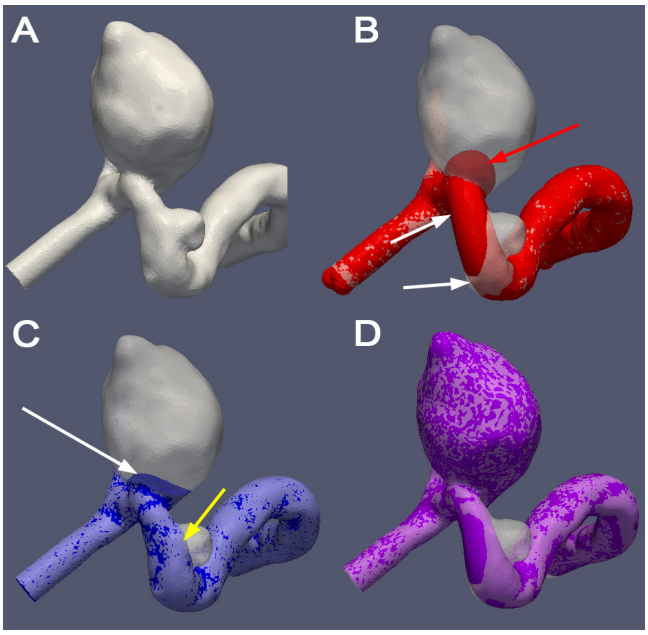

Figure 4.2: Example of the vessel modification process: **A** Original vessel structure (Model A). **B** Semi-automated computational removal of the IAs: red is resultant vessel, white is original vessel, red arrow indicates unintended IA removal, white arrow shows altered vessel curvature. **C** Modified vessel from part B, projected onto original vessel to reclaim vessel curvature and create area (white arrow) for needed IA reattachment, while slight errors due to vessel projection in areas of (intended) removed IA (yellow arrow) were removed by vessel smoothing. **D** Completed modification (purple) shows Model B against original vasculature (white, Model A).

4.1.1 Analysis of Hemodynamic Parameters

Wall Shear Stress Wall shear stress (WSS) values were calculated by the ANSYS-FLUENT solver (Equation 3.1) for all cases, across all data points (spatial and temporal). For every IA, the spatio-temporal averaged wall shear stress (STA-WSS), maximum WSS (MaxWSS), and mimimum WSS (MinWSS) values were calculated. In addition, the Oscillatory Shear Index (OSI) was calculated using Equation 3.5.

Kinetic Energy The spatially-averaged kinetic energy density (SA-KED) within the IA dome was calculated as follows:

$$SA - KED = \frac{\frac{1}{2}\rho \sum v^2}{n} \tag{4.1}$$

Where v is the velocity values, ρ is the mass density of blood, and n is the number of voxels within the IA. The SA-KED at each time-step (cardiac phase) was calculated, as well as the spatio-temporally averaged KED (STA-KED) for all cases.

Degree of Volume Overlap Among Flow Vortices Identification of vortices within the IA sac was performed using the CE method described in 2.3. Explanation of the calculation of the degree of volume overlap (DVO) can be seen in Section 2.1.4. The temporally-averaged DVO value (TA-DVO) and standard deviation of DVO values over the cardiac cycle (STD-DVO) were calculated for each case. In the event that no vortices could be identified in a specific IA, it was removed from any analysis dealing with vortices (but remained for analysis of other characteristics).

4.1.2 Statistical Analysis

The paired t-test (or paired Wilcoxon-Mann-Whitney test for non-normalized data distributions) was used to compare Model A and Model B differences across all time-steps (final cardiac cycle) for the following characteristics: WSS, OSI, KED, and

DVO. Paired t-tests were also performed to assess differences between the MaxWSS and (largest) MinWSS across the cardiac cycle between the pre and post-remodelled cases. To assess statistical differences between IA types (adjacent, proximal and distal IAs), ANOVA tests (with Tukey post hoc analysis) were performed for the STA-WSS, STA-KED and TA-DVO values. All statistical analyses were performed at a 0.05 level of significance, and were measured with in-house scripts using the RStudio software program (Version 1.0.136, RStudio, Boston, MA USA).

4.2 Results

4.2.1 Hemodynamic Characteristics Among IA Types

Initial comparisons of the STA-WSS, STA-KED, and TA-DVO values between IA types can be seen in Figure 4.3. A trend across all IAs was seen in which the calculated values are higher in the proximal IAs over distal or adjacent IAs, yet said differences were not found to be statistically significant. Aneurysmal aspect ratios (*i.e* IA height/ostium width) have been shown to be a geometric characteristic inversely correlated to IA WSS. To ensure that the relative differences of STA-WSS between groups were not wholly driven by their aspect ratios, the calculated STA-WSS were plotted in Figure 4.4 against their respective aspect ratios. The STA-WSS

values for all IA types were shown to decrease in relation to their aspect ratios, yet the rate at which the STA-WSS decreased (slope of the fitted line) was nearly 2 times quicker for the proximal and adjacent IAs than for the distal IAs of similar aspect ratios.

4.2.2 Inter-aneurysm “Damping" Effect (Model A vs. Model B)

The magnitude of flow energy and WSS tends to follow the characteristic pattern of the inflow waveform: peak WSS and energy values occurring near peak systolic flow, and lower values during slow diastolic flow [14]. A small number of spiked increases or decreases in measured values over the cardiac cycle, may skew the overall pattern of hemodynamic changes between Models if only the spatio-temporally averaged values are considered. To address this, comparative analysis between Models were made using the values across all time-steps (SA-WSS, SA-KED, and DVO), as opposed to assessing their temporally averaged characteristics.

Comparison of hemodynamic characteristics across all time-steps (SA-WSS, SA-KED, and DVO) showed notable changes between Model A and Model B. In the presence of adjacent IAs, the local flow of the parent artery is likely “split", supplying flow into both IAs simultaneously. In Model B of the adjacent IAs, the splitting effect was

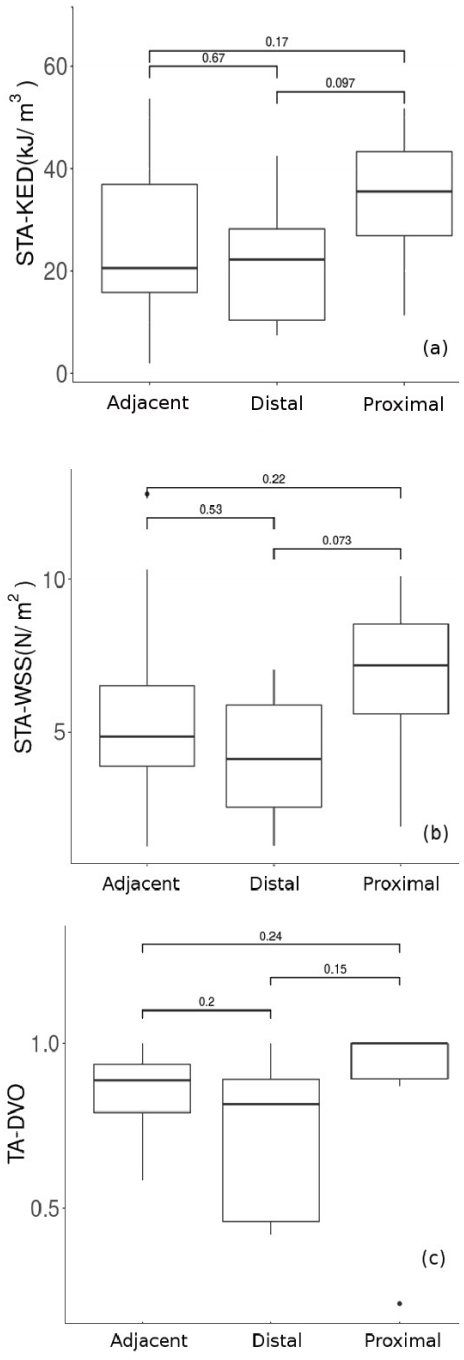

Figure 4.3: Box plots of characteristic differences between adjacent (both), proximal and distal IAs: **(a)** STA-KED, **(b)** STA-WSS and **(c)** TA-DVO. The top and bottom of boxes indicate 75 and 25 percentiles, respectively. The line inside each box represents their median. Error bars show the minimum and maximum values. Circle markers indicate outliers. p-values displayed for comparison between IA types

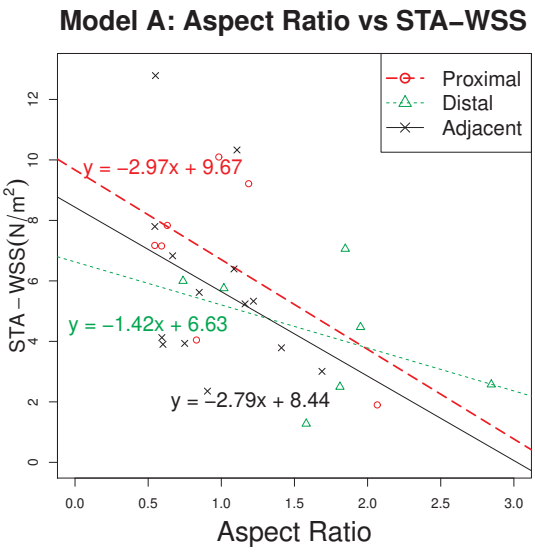

Figure 4.4: A plot showing the relation between STA-WSS and the aspect ratio in Model A

reduced, resulting in higher flow energy (SA-KED, SA-WSS) being directed into the remaining IA. This increase in energy also coincided with a subsequent decrease in IA DVO. In contrast, removal of the proximal IA resulted in lower flow energy within the subsequent distal IA. Model B simulations for distal IAs were seen to have an overall decrease in SA-KED and SA-WSS and an increase in DVO values. All these changes were statistically significant. The analyses for MaxWSS and MinWSS across the cardiac cycle showed no statistical significance between Models. The outcomes of all statistical analyses for these hemodynamic characteristics are summarized in Table 4.2.

Assessment of STA-WSS changes between Model A and Model B found that, while

WSS magnitude changes occurred, the overall spatial patterns remained visually consistent (see Figure 4.5). A quantitative assessment of the maximum OSI (MaxOSI), identifying the greatest directionality change of the WSS, showed a decrease in adjacent IAs in Model B to compared to Model A, while values increased in distal IAs but none of these changes were found to be statistically significant. In terms of changes to DVO values, a decrease in vortex stability was noted after removal of one of the adjacent IAs, indicating flow in the remaining IA becomes significantly more unstable. As for the distal IA (after proximal removal), a slight increase was seen in DVO values but was not found to be significant. Outcomes of statistical tests for hemodynamic variables between Models can be seen in Table 4.2.

Table 4.2
A summary of notable changes in hemodynamic parameters in Model B as compared to those in Model A. A paired t-test (or Wilcoxon test) was performed to assess changes across all time-steps of the final cardiac cycle.

Group	Results	p-value
Adjacent	Increase in SA-KED	<0.001
	Increase in SA-WSS	<0.001
	Increase in MaxWSS	$=0.09$
	Increase in MaxOSI	$= 0.24$
	Decrease in DVO	<0.001
	No Change in MinWSS	
Distal	Decrease in SA-KED	<0.001
	Decrease in SA-WSS	<0.001
	Decrease in MaxWSS	$= 0.31$
	Decrease in MaxOSI	$=0.06$
	Increase in DVO	$= 0.153$
	No Change in MinWSS	

To determine if IA geometry was a driving force behind the statistically significant changes to vortex stability post vessel remodelling in adjacent IAs, linear regression

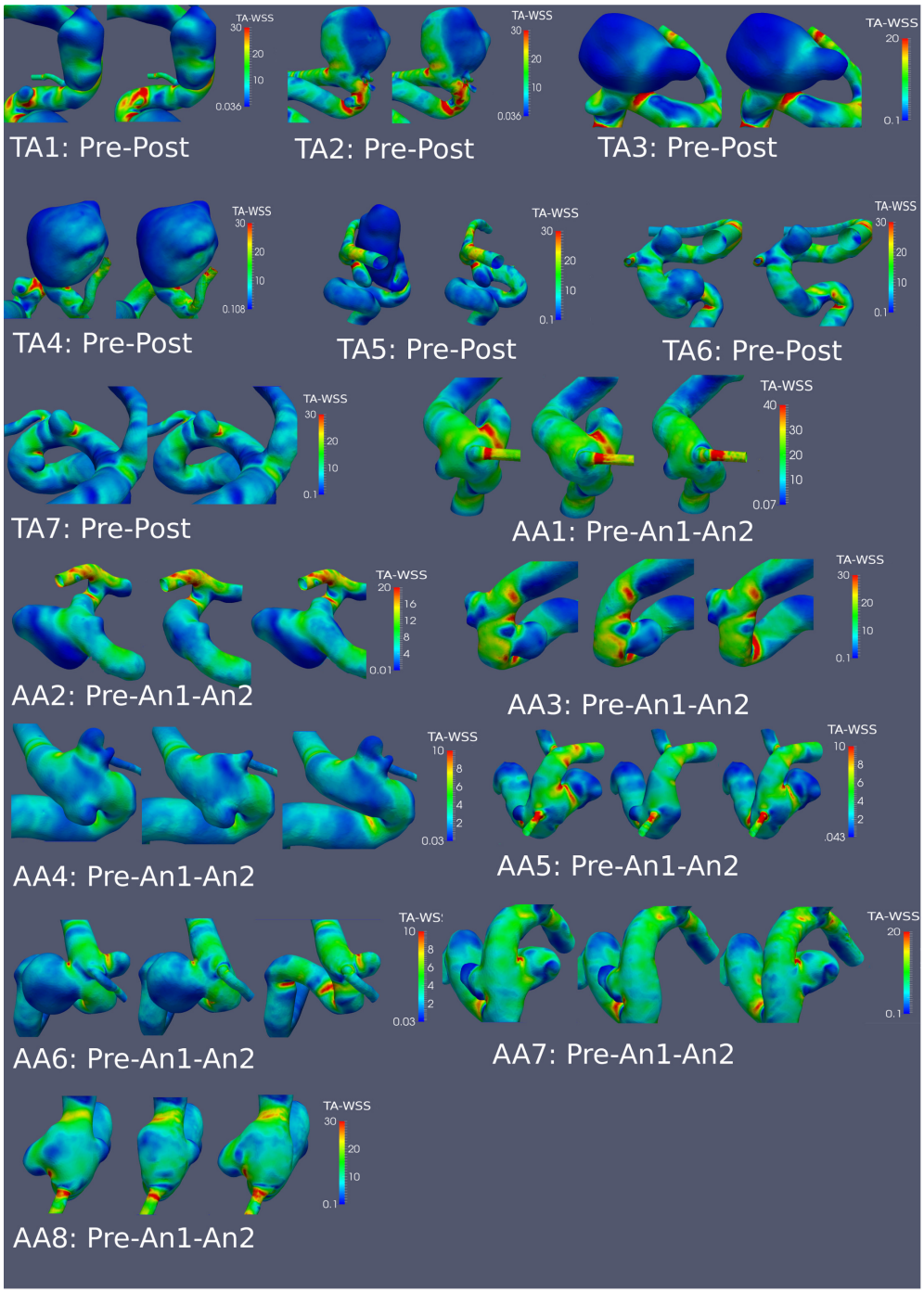

Figure 4.5: Plots showing spatial patterns of TA-WSS comparing between Model A and Model B. Color bars were scaled to each IA grouping as to assess spatial TA-WSS patterns. Pre representing all IAs intact (Model A), Post as proximal IA removed, An1-2 as either An1 or An2 remaining (adjacent IAs).

analysis was performed on temporally averaged mean percent change of DVO against IA geometry: IA volume, ostium area, aspect ratio, parent artery diameter, and IA diameter. A strong negative relationship was seen between the IA volume, IA diameter, and ostium area of adjacent IAs in relation to their mean percent change in DVO. Statistical testing was performed and found no distinct linear relationship in mean percent change in DVO when compared to their IA geometry. Similar comparative analysis was performed on the temporally averaged percent changes of SA-WSS and SA-KED values in relation to IA geometry. No statistically significant linear comparison was found between the degree of SA-WSS or SA-KED change vs IA geometry for any of the IA groups.

Table 4.3
Linear Regression Analysis: Mean Percent Change to DVO in Relation to IA Geometry: IA Volume, Ostium Area, Aspect Ratio, IA Diameter, and Parent Artery Diameter. Only outcomes with statistical significance shown.

	% Change DVO		
	Adja. Vol.	Adja. Ost.	Adja. IA Diam.
Corr.	-0.734	-0.887	-0.673
p-value	0.016	0.0006	0.032
Slope	-0.046	-0.786	-2.37
Y-int.	0.208	9.38	7.87

4.3 Discussions

4.3.1 WSS Analysis

When faced with multiple IAs in a given section of cerebral vasculature, initial assessments may result in only select IAs being surgically treated, leaving other IAs intact. Yet current information on how closely spaced IAs impact each other's hemodynamics, or how the repair of a single IA may alter flow conditions in the untreated IAs is limited. This study focused on identifying hemodynamic features particular to closely-spaced IAs and assessing the hemodynamic impacts of one IA on the other: WSS, KED, flow stability, and OSI.

In our study, as IA aspect ratio increased, the negative relation to lower STA-WSS among proximal and tandem IAs were approximately 2 times greater than that which occurred among distal IAs of similar characteristics (Figure 4.4). The probability that there was stagnant flow in proximal and tandem IAs as compared to the distal IAs (of similar aspect ratios) was supported by the relative higher TA-DVO values seen in proximal and tandem IAs in relation to the distal IAs (Figure 4.3c). According to the theory advocating slow flow as a risk factor for IA rupture, several of our observations would indicate that these proximal IAs are, as earlier proposed by Jain

and Crompton, more prone to rupture than are the distal IAs[78, 155]. In the majority (71.4%) of the distal IAs, the presence of a proximal IA increased the distal IA's SA-WSS; possibility helping to limit destructive vascular remodelling that may occur during low WSS [12, 370]. Assuming the theory of deleterious effects from slow or stagnant flow to have some validity, our observations show that a proximal IA may actually provide a protective effect to the distal IA of a tandem pair[155]. In such a case, repair of a proximal IA may worsen conditions in a remaining distal IA by decreasing both its SA-KED and SA-WSS while possibly leading to in increase in flow stagnation. Yet in adjacent IAs, surgical/endovascular interventions on one IA may altered localized flow conditions, leading to increased flow energy and WSS into the remaining IA. It is worth noting, that while flow stressor and energy was altered post-singular aneurysmal repair, less of a change was seen in the distribution of stressors pattern or oscillations in stressor directionality (OSI).

The clinical impacts of aberrant WSS is known to trigger varying vascular degradation: with high WSS thought to impact IA growth, expansion, and mural cell death, and low WSS thought to impact degenerative vascular inflammation [228]. Smaller IAs tend to have higher WSS than larger IAs, yet both IA sizes are shown to have lower WSS in their ruptured IAs then their unruptured counterparts [167, 386]. While ruptured IAs tend to have lower WSS, there exists a degree of overlap in the range of their hemodynamic values with unruptured IAs [88, 233, 374]. In this study the statistically significant decreases in STA-WSS within distal IAs post-proximal IA repair

was noted. Such an impact could worsen hemodynamic conditions within an IA and increase the likelihood of rupture.

4.3.2 Vortex Analysis

While assessment of near-wall flow stressors are often taken into account to assess the potential severity of IAs and aid in the choice of clinical interventions, WSS give little insight into the bulk flow patterns within the IA sac. Flow stagnation is a proposed mechanism that create conditions impacting the weakening of an IA wall[43, 51, 228, 274, 370]. Through this study, the stability of the vortex patterns (DVO) identified by our CE method gives novel insight into hemodynamic changes brought upon by the treatment of a single IA, which would be otherwise overlooked only relying on WSS-based variables. Specifically, the simulated ”repair" of one of two adjacent IAs was found to disrupt the stability of vortices in the remaining IA while alterations to WSS-indices are less prevalent. The reductions in the quantified DVO values indicate that, while an unrepaired IA still may pose a threat to patient health, the reductions in flow stability caused by the repair of another IA may help reduce risk severity. While increases in DVO values were seen in distal IAs post-proximal repair, findings were not statistically significant. There may be conflicting factors impacting the degree of change in DVO for proximal IAs, requiring further studies with a greater number of cases to determine: distance between IAs or size of proximal

IA.

4.3.3 Limitations

For this study, the number of patient data containing multiple IAs was limited and all IAs in this study were unruptured. A greater number of cases analyzed could help strengthen finding in this study, as well as determining if the characteristics of ruptured IAs amplify or dampen the changing hemodynamic characteristics in subsequent IAs. Additionally, no information was available into the order of IA development (or if the multiple IAs developed simultaneously). A longitudinal analysis of patients presenting with IA(s) or *in-vivo* models pre and post IA development would be needed to address this issue.

The simulated treatment of an IA in this study was done in an overly simplified way. More specifically, the IA was completely removed and the vessel reconstructed, resulting in no flow entering the “treated" IA. In the clinical setting, the complete isolation of the IA from the blood stream is not always achieved [247]. Additional studies mimicking varied repair parameters (*e.g.* different coverage values for flow diverting stents or IA sac occlusion via coiling) would be provide more insight for how clinical management of a singular IA impacts hemodynamics in any remaining IAs. Furthermore, all proximal IAs regardless of their sizes were removed to simulate

a clinical treatment procedure. However, in some scenarios, that implies that a large distal IA would not be initially treated while the smaller proximal IA would be treated. While small IAs are associated with their own risk of rupture [199], the prevailing mindset is larger IAs pose a greater risk of rupture. Nevertheless, the chosen methodological method or removal of the proximal IA regardless of size difference was necessary for study consistency and distal IAs may have limited impact on the hemodynamics in proximal IAs.

4.4 Conclusions

The focus of this work was to investigate altered hemodynamic conditions within a multiple IA system pre and post treatment of a single IA. This study showed that closely spaced IAs may exhibit significant hemodynamic alterations onto each other when concerning WSS, KED and flow stability (DVO). These initial results suggest that surgical or endovascular interventions on only one (of a multiple IA scenario) could lead to detrimental hemodynamic changes into developed IAs. Understanding these alterations may help uncover risk factor(s) pertaining to the post-surgery growth of remaining IAs.

4.4.1 Acknowledgments

We are grateful to our colleagues (in particular, Mr. Chris Haferman at the Michigan Tech and Dr. Pengfei Yang from the University of Wisconsin) for their assistance in data processing and acquisition. This research is partially supported from the Michigan Tech/Portage Foundation Graduate Fellowship and a research contract from Siemens Medical Solution (USA) Inc.

Chapter 5

Vortex Analysis to Differentiate Ruptured and Unruptured Aneurysms of the Middle Cerebral Artery

As mentioned previously, clinicians must make a diagnostic choice if surgical or endoscopic-based interventions should be undertaken when an IA is identified. Yet such treatments may be over perscribed as the majority of IAs remain at low rupture risk, and possible surgical complications can cause patient morbidity or mortality similar to that of IA rupture. IA geometric characteristics and their

usefulness in predicting rupture have been extensively investigated with varying success[163, 187, 213, 234, 370]. A number of studies have eluded to an increase in IA size as a risk for both IA growth and rupture. [16, 125, 346]. A meta-analysis performed by Brinjikji et al reported that IA $\leq$ 10 mm in size (diameter) grew at a rate $<$ 2.9% per year, while IAs $>$ 10 mm were associated with growth rates of 9.7% per year[40]. This growth was also reported with an associated IA rupture rate: 3.1% per year compared with 0.1% per year for stable (non-growing) aneurysms (p $\leq$ 01). Findings such as these suggest that IA size is indicative of rupture risk, with large IAs (>10mm) thought to be at high rupture risk, leading the majority to undergo surgical intervention [234, 364, 370]. Whereas small IAs (<4mm) are thought to be at low rupture risk and thus are typically spared surgery, even though work suggests small IAs rupture at not insignificant rates[199]. This leaves medium-sized IAs to which the decision to perform clinical intervention based on geometric characteristics alone is less ubiquitous. WSS and its derivatives are often incorporated alongside IA geometry as a means to differentiate high risk IAs from those unlikely to rupture[192, 211, 370]. However, as previously mentioned in Chapter 1, indices based on WSS extrema showed varying predictive strength across studies[36, 84, 163, 270, 345, 355]. The combination of geometric indices having reduced usefulness in predicting medium-sized IA rupture risk and the varying predictive strengths of WSS, emphasises the need for novel analytic metrics to help differentiate which IAs should be subject to surgical intervention.

My previous work bolsters the idea that vortices within bulk heomdoynamic flow (versus near-wall WSS) impact IA development[320, 321] and work from other groups indicate that vortices play a role in IA rupture[345]. Yet, while a study by Varble et al. [346] aimed to determine if a strong correlation between vortices and IA rupture existed, findings showed minimal correlation. This weak association may have been in-part due to the study focusing on identifying only the centroid region of vortices and thus, limited the scope of assessed vortex characteristics. The goal in this work was to assess the strength of the developed CE method for analyzing the broader spatial-temporal characteristics of vortices to help improve the identification of characteristics indicative or IA rupture in a cohort of 47 middle cerebral artery (MCA) aneurysms: 12 ruptured and 35 unruptured. Specifically if vortices help improve the assessment of medium sized IAs (4-10mm), sizes difficult to assess using currently applied geometric and WSS metrics. Insight into the characteristics of complex flow indicative of IA rupture could help improve the understanding of this vascular pathology and could one day aid in clinical decision making.

5.1 Computational Model Creation

From an internal database, patient-specific IA models were created from medical imaging data (DICOM images of 3D rotational angiographies) acquired

from three sources: University of Michigan Medical Center (USA), Changhai Hospital at Shanghai (China), and the Aneurisk open-source repository (http://ecm2.mathcs.emory.edu/aneuriskweb/index). The inclusion criteria were as follows: (1) sufficient data quality to establish CFD models, (2) IA size (width) between 4 and 10 millimeters (clinically qualified as medium-sized IAs), and (3) IAs at the M1 bifurcation the MCA. Only MCA IAs were analyzed in this work as differences in IA location (MCA, anterior communicating artery, internal carotid artery, etc), or IA type (bifurcation, sidewall, fusiform), may have differing vortex characteristics that would confound predictive models. To properly determine how these different factors may impact vortex characteristics concerning rupture risk and would require a more substantial data-set for proper analysis. As this was a retrospective analysis of existing data, only angiographic data acquired post-rupture were available for ruptured IAs.

Geometric (stereolithography [STL]) models were created by isolating the vessels of interest in DICOM files and converting them into STL files and then edited in the same manner as covered in section 2.1.1. Some STLs were directly available from the Aneursik repository and Changhai Hospital. The available portion of the parent vasculature proximal to the internal carotid artery siphon was maintained, all secondary outlet vessels proximal to the IA were kept, and a portion of the parent vessel distal to the IA was maintained as outlets. Example STLs can be seen in Fig 5.1

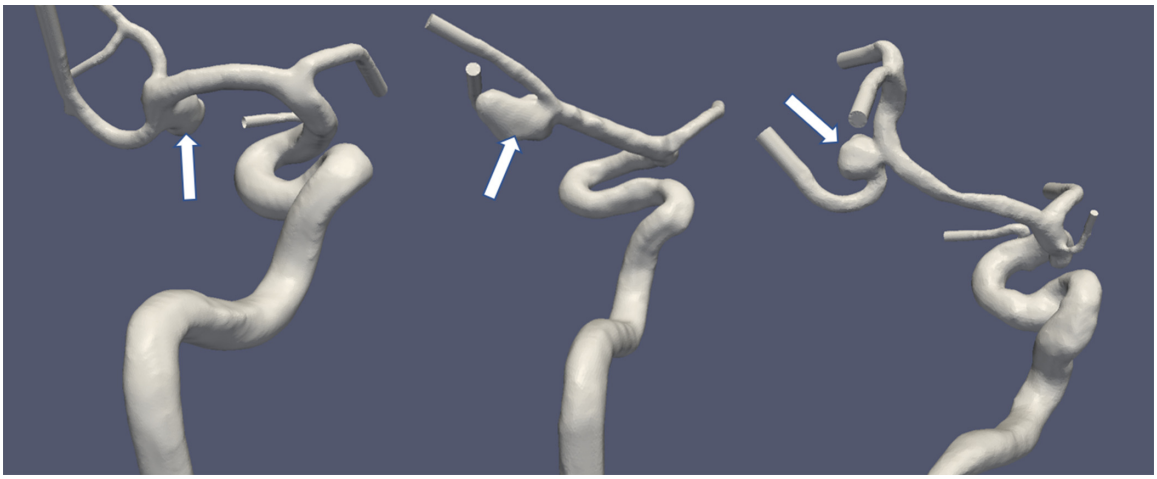

Figure 5.1: Three examples of patient-specific vessel models of bifurcation IAs of the M1 section of the MCA. White arrows indicate IAs

All models were converted into an unstructured, 3D tetrahedral volumetric mesh under the VMTK framework. Each case contained 1.5-2 million mesh elements.

5.2 CFD Simulations

Blood flow velocity and WSS was calculated using the ANSYS-FLUENT software (Version 17.0, ANSYS-FLUENT Inc., Canonsburg, PA, USA) using the same methodology as in section 2.1.3. The inflow waveform from Gwilliam et. al.[128] was applied as velocity inlet boundary conditions for simulations in this work. As flow waveform characteristics vary with age and may alter the simulated hemodynamic characteristics, a secondary analysis of WSS and vortex characteristics was performed using a waveform by Hoi et. al, taken from older patients (averaged 68 years old)[144] as was

used in Chapter 3.

5.2.1 Aneurysm Geometric Characteristics

For the quantification of IA geometric characteristics, the IA sac was first isolated from the vessel using a published method[264] and the resultant cut plane was capped and identified as the IA ostium using an in-house script written in VMTK. The geometric values from IAs from the Michigan Medical Center and Changhai Hospital were calculated using in-house scripts in VMTK. The geometric measurements calculated (using our in-house scripts) for IAs from the Aneurisk data-set were compared with the measurements given by the Aneurisk repository to ensure similar values. For the sake of reproducibility, we used the geometric values given by the Aneurisk site for predictive modeling.

Seven (9) geometric parameters were calculated for each IA[93, 233, 264].

Aneurysm Surface Area and Volume: Measured directly from the isolated IA geometry before and after ostium capping (respectively).

Aneurysm Height: Typical IA height measurement follows a straight line of the maximum stretch from the ostium centroid to the IA dome[93, 213]. Instead, this study used a modified height measurement [110, 264]. The length of the centerline of the IA

sac is measured, starting from the ostium centroid, following the shape of the IA sac, to the highest point of the IA dome. The radius of the maximum inscribed sphere at the centerline's endpoint is added to the length measurement to fully measure the IA height.

Vessel Diameter: The parent artery diameter value is computed at locations close to the aneurysm ostium [264]. For terminal aneurysms, the vessel diameter of the common branch was measured at the point prior to centerline splitting between the daughter arteries, and both daughter arteries' diameter were measured at the point one (common artery) diameter away from the IA ostium cut. The average of the three values was used as the value of the vessel diameter.

IA Width: The maximum width of the IA sac along the direction perpendicular to flow entering the IA.

Size ratio(s) IA size ratios (width/vessel diameter and height/vessel diameter) were calculated.

IA secondary bulb The presence or absence of secondary bulbous portions of the IA wall was identified by a human observer. An example of an IA with/without bulb can be seen in Fig5.2

Aspect Ratio: A modified calculation of the commonly defined aspect ratio (aneurysm

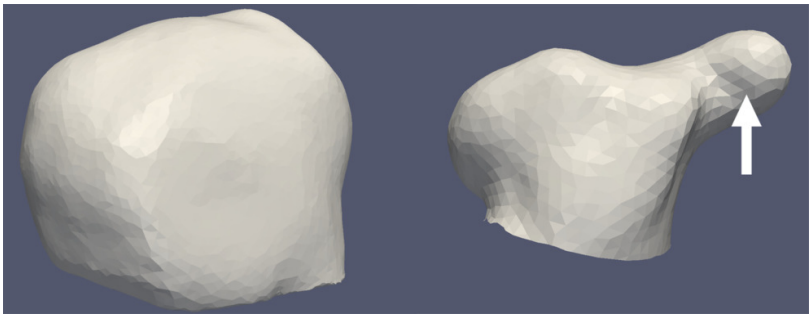

Figure 5.2: (Left) IA without a secondary bulbous portion of the IA wall. **(Right)** IA with a secondary bulbous portion of the IA wall (arrow).

height/ostium diameter) was used by adapting the modified IA height calculation height, and both the area and circumference of the ostium into the aspect ratio calculation as the ostium diameter is rarely uniform for an IA[264].

$$AspectRatio^{*} = \frac{IA_{height^{*}}}{4 * (Ostium_{area}/Ostium_{circumference})} \tag{5.1}$$

The aspect ratio of an IA has been shown to be correlated with levels of hemodynamic stressors and has been used as an ease-of-use method to assess conditions within an IA [383].

5.3 Aneurysm Hemodynamic Characteristics

Wall Shear Stress: The calculation of WSS was performed by the ANSYS-FLUENT commercial finite-element solver (ANSYS v17.0) by solving Equation 3.1.

The spatial-temporally averaged value of the aneurysm's WSS(STA-WSS) was calculated alongside its temporally-averaged WSS minimum (TA-WSSMin) and temporally-averaged WSS maximum(TA-WSSMax). Additionally, the temporally-averaged low wall shear ($\leq$2 dynes/cm^2) area (TA-LSA) and low shear area standard deviation (LSA-std) were calculated for each case.

Oscillatory Shear Index: The mean and standard deviation of OSI were calculated for each case using Equation 3.5 .

For predictive modeling, all WSS variables were only evaluated across cardiac-cycle systole. In relation to systole, the diastolic portion of the cardiac cycle typically has a lower flow rate, minimal changes occurs to the flow pattern, and lasts for a greater portion of the cardiac cycle. Averaging hemodynamic values over the entire cardiac cycle may skew outcomes in relation to the characteristics of diastole. As to capture the greatest degree of hemodynamic change for both WSS and vortex characteristics, values (means, standard deviations) were assessed only across the systolic portion of the cardiac cycle.

5.4 Aneurysm Vortex Characteristics

In an similar manner to vortex characteristics described in Chapter 2, spatial temporal characteristics of vortices were quantified: vortex volume, vortex surface area and vortex stability (DVO). The number of vortices was not used in assessing statistical characteristics as it was found that typically only one vortex was identified in an MCA IA (regardless of rupture status) when using the developed CE methodology. As vortex volume can be highly correlated with IA volume (see Table 2.2), it was not used directly in predictive modeling as to avoid significant collinearity between indices. Instead, the vortex volume was normalized to their IA volume, as well as normalizing the surface area of the vortex iso-surface to its IA surface, indicating the proportion of IA flow constituting a vortex. These new variables were called vortex volume to IA volume (VtV) and normalized vortex surface (NVS) and their means and standard deviations (across cardiac systole) were calculated.

5.5 Statistical Analysis / Predictive Modeling

Due to the number of potential variables used for rupture predictive modeling, possible non-linear relationships (between variables), and the potential for model overfitting, a statistical predictive method was required that could better contend with

these conditions. The Support Vector Machine (SVM) methodology, a supervised machine learning algorithm used for classification problems, was implemented for this work[157, 306]. Given the multiple parameters thought to impact IA rupture, SVM utilizes a structural risk minimization principle to determine a hyper-plane that best divides binary outcomes: ruptured and unruptured IAs. The orientation of the chosen hyper-plane aims to generate the largest minimum distance (margin) between data points of each class.

An explanation of the equations behind SVM and the chosen kernel function (radial basis function) can be seen in Appendix B.

A number of models were generated using different variable groups:

- Geometric
- WSS
- Vortices
- Geometric + WSS
- Geometric + Vortex
- WSS + Vortex
- All groups (Geometric + WSS + Vortex)

Statistical characterization modeling was performed via cross-validation (80%/20% training/testing) over 100 iterations to help limit model over-fitting. The area under the curve (AUC) of receiver operating characteristic (ROC) curves were quantified for each iteration and averaged (over all iterations). Additionally, the total accuracy of models and the percent of correctly identified ruptured and unruptured IAs (across all iterations) were calculated.

A summary of the methodology used in this study, from the creation of vascular models, simulation of flow, quantification of vortex characteristics, to the assessment of vortices' impact on statistical characterization can be seen in Figure5.3

5.6 Results

A summary of calculated indices can be seen in Table 5.1

5.6.1 Statistical Characterization Model Outcomes

Relying solely on WSS led a low AUC value, having minimal success for distinguishing ruptured from unruptured MCA IAs (∼0.56 AUC). The geometric+WSS model improved the resultant AUC compared with using just WSS indices, but still underperformed when compared geometric indices alone (0.80 geometric model AUC).

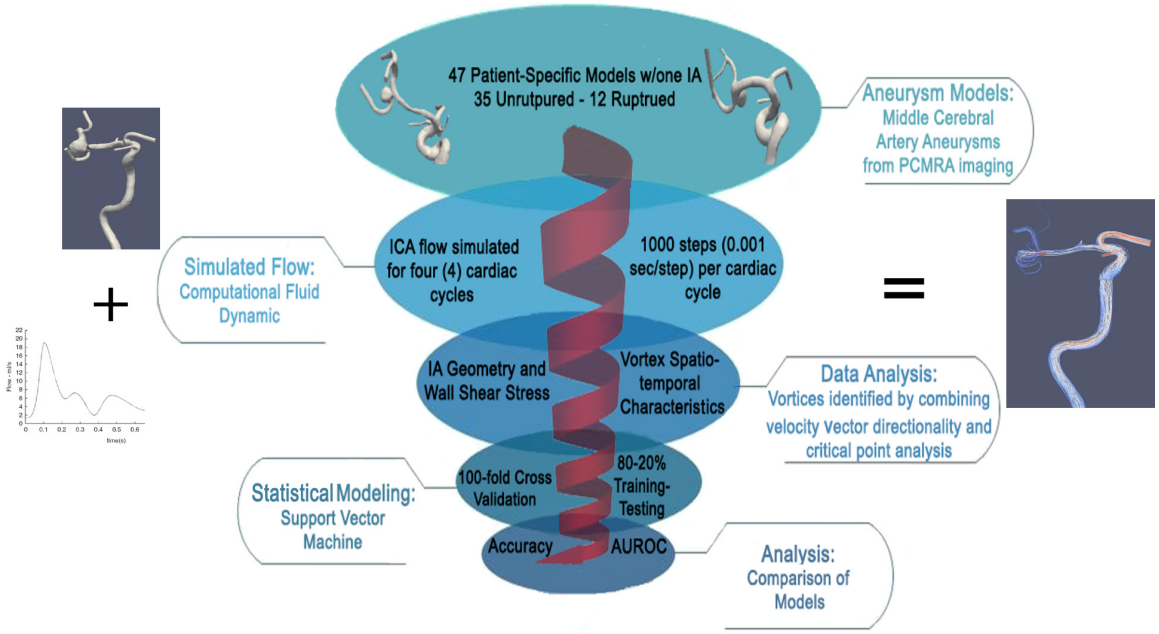

Figure 5.3: Summary of methodology for measuring vortex characteristics and determining their impact on statistical characterization. Creation of patient specific vascular models, generation of simulated blood flow data, analysis of IA geometric and hemodynamic characteristics, modeling using 100-fold cross validation via Support Vector Machine methodology, analysis of outcomes.

A characterization model solely utilizing vortex indices resulted in an AUC of only 0.62, performing better than their WSS counterparts but worse than the geometric model. The proposed vortex indices alongside WSS improved the resultant AUC over the WSS model alone but was similar to that of solely relying on vortex indicies. Adapting all index groups into a statistical characterization model had similar AUC values to that of the geometric (only) model. The ROC curves from statistical characterization models and their AUC's can be seen in Figure 5.4

Analysis of ruptured and unruptured IAs properly identified showed our geometric

Characteristic	Unruptured: 35 Cases	Ruptured: 12 Cases	Total: 47 Cases
IA Volume *	155.79±157.64	75.47±53.78	135.27±142.52
IA Height	6.52±2.60	5.64±1.48	6.30±2.38
IA Width	6.83±2.06	6.12±1.51	6.65±1.94
Size Ratio (Height)	2.90±1.30	3.00±0.99	2.92±1.22
Size Ratio (Width)	3.04±1.03	3.28±1.20	3.10±1.07
Aspect Ratio	1.61±1.61	1.73±0.86	1.64±1.45
Vessel Diameter *	2.31±0.46	1.97±0.38	2.22±0.47
Systolic Sta-WSS	6.59±7.51	6.48±4.44	6.56±6.81
Systolic TA-WSSMin	0.44±0.85	0.37±0.36	0.43±0.76
Systolic TA-WSSMax	47.60±51.15	62.28±69.40	51.35± 55.92
Systolic OSI	0.02±0.02	0.02±0.03	0.02±0.02
Systolic TA-LSA	39.76±27.75	31.81±23.31	37.73±26.67
Systolic TA-LSAstd	19.55±9.72	24.76±6.88	20.88±9.30
Systolic TA-DVO	0.73±0.13	0.78±0.14	0.74±0.13
Systolic STD-DVO	0.15±0.07	0.16±0.10	0.15±0.075
Systolic VtV	14.91±6.05	12.95±7.45	14.42±6.47
Systolic NVS	37.71±12.35	30.87±13.04	35.96±12.75

Intracranial Aneurysm (IA), Normalized Vortex Surface (NSV), Oscillatory Shear Index (OSI), Spatial-temporally averaged Wall Shear Stress (STA-WSS), Standard Deviation Degree of Volume Overlap (STD-DVO), Temporally Averaged Low Shear Area (TA-LSA), Temporally Averaged Low Shear Area Standard Deviation (TA-LSAstd), Temporally Averaged Degree of Volume Overlap (TA-DVO), Temporally Averaged Wall Shear Stress Minimum (TA-WSSMin), Temporally Averaged Wall Shear Stress Maximum (TA-WSSMax), Vortex Volume to Aneurysm Volume (VtV).

Table 5.1

A list of geometric, wall shear stress (WSS), and vortex-related indices used for statistical characterization. Parameters are listed as Mean + one standard deviation. * indicates characteristics with statistical differences between unruptured and ruptured IAs: t-test, $p < 0.05$.

model, while having the highest AUC overall, had limitations. Said model identified 90.5% of unruptured IAs across the 100 iterations of SVM modeling, while only properly identifying 46.5% of the ruptured IAs. The vortex model had reduced success in rupture IA identification but an increase in unruptured identification (29.4 and 94.5 % respectively) compared with its geometric counterpart. The geometric+vortex model improved the identification of unruptured IAs yet showed reductions in the success of identifying ruptured IAs when compared to the geometric model: 94.3 and 25.0 %.

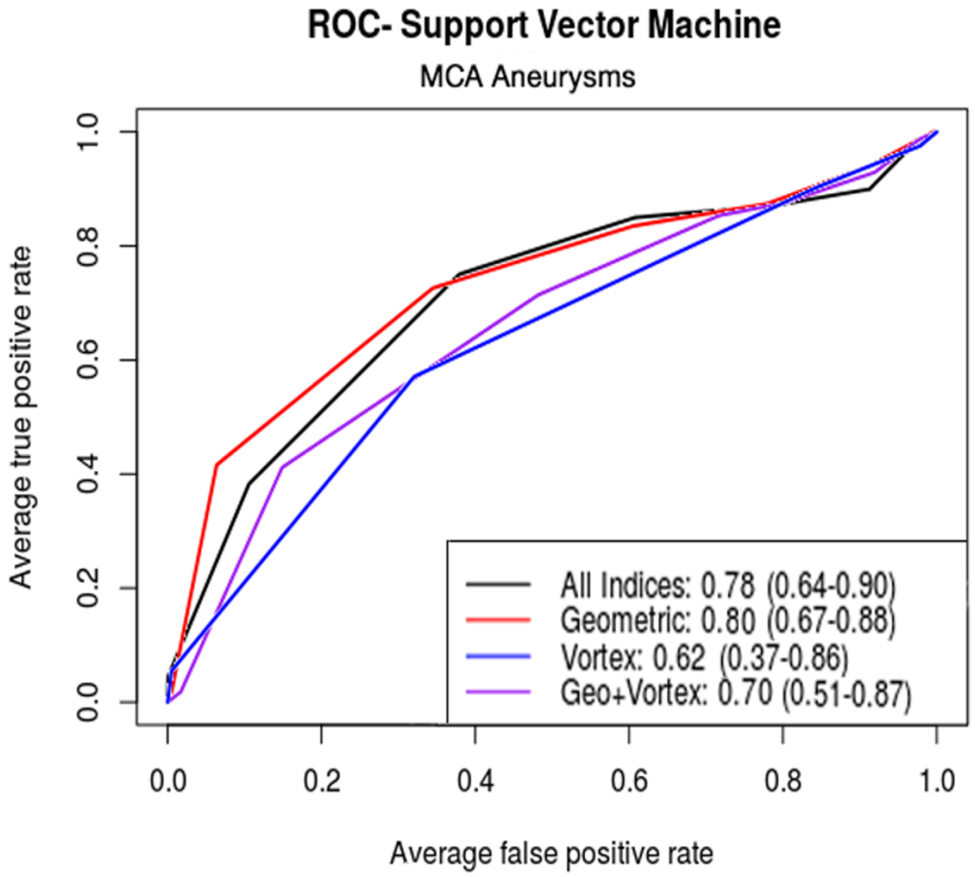

Figure 5.4: ROC curves averaged from 100 runs of cross-validation support vector machine statistical characterization modeling. Outcomes: AUROC (95% CI) for geometric, vortex, geometric+vortex, and all indices models. WSS based model ROC curves (besides the 'all' model) are not shown for ease of visualization.

Our WSS model overestimated almost all MCA IAs as unruptured, properly identifying 97% of and only 2% of ruptured IAs in our data set. The WSS+vortex model had similar outcomes in rates of unruptured and ruptured accuracy to that of the vortex model alone.

While individual geometric, WSS and vortex indices showed mixed outcomes toward

prediction outcomes, combining all indices into a model led to the strongest outcome in terms of accuracy: an overall accuracy of 0.85, identifying 99.0% unruptured and 44.3% ruptured IAs.

The values for AUCs, total accuracy, and percent of properly identified unruptured and ruptured IAs across all data sets and models can be seen in Table 5.2.

Table 5.2
AUC and accuracy calculated for all statistical characteristic models with varied index groups for MCA IAs. Models consisted of geometric, wall shear stress, and vortex indices.

Models	Mean (AUC 95% CI)	Total Accuracy	Ruptured Identified (%)	Unruptured Identified (%)
Geo	0.80(0.67-0.80)	0.80	46.5	90.5
WSS	0.56(0.32-0.79)	0.74	2.0	97.0
Vortex	0.62(0.37-0.86)	0.78	29.0	94.5
Geo + WSS	0.73(0.56-0.88)	0.76	44.5	87.0
Geo + Vortex	0.70(0.51-0.87)	0.77	25.0	94.3
Vortex + WSS	0.61(0.39-0.84)	0.77	27.0	93.7
All	0.78(0.64-0.90)	0.85	43.5	99.0

5.6.2 Changes Under Differing Waveform

The waveform used in this work was taken from work by Gwilliam et al.[128] and was measured from patients of an median age of 28 years (range: 20-40 years). As the chosen inlet flow waveform may impact hemodynamic characteristics (WSS and vortices), a secondary analysis was performed to assess the impact that varied waveforms (adjusted for age) may have on simulated values and prediction outcomes. Four (4)

randomly selected cases had a second simulation performed using a waveform characteristic of flow rates in the carotid bifurcation in older adults measured by Hoi et al.[144]. The secondary (Hoi) inflow waveform was chosen from the characteristic of flow from older adults (mean 68±8 years). Example of the differences between flow waveforms and can be seen in Figure 3.2. Vortex characteristics of the cases run using the Hoi inlet waveform were compared to their counterparts run with the Gwilliam waveform. At a 0.05 level of significance, paired Welch's two-sample t-test showed no statistical difference for Systolic TADVO values between the waveforms: p-value 0.21 (95% CI: -0.03-0.15). No statistically significant reduction in the VtV generated with the Hoi waveform was seen when compared to the Gwilliam waveform, though the value was near-significance and may change if a a larger sample set were to be investigated: p-value 0.05, 95%CI (-0.03-2.46). A statistically significant decrease was seen in STA-WSS and TA-WSSMax values generated by the Hoi inlet waveform in comparison to the Gwilliam waveform: p-value < 0.001, (95%CI: 0.89–2.33) and p-value < 0.001, (95%CI: 4.88-16.06) respectively. These changes were to be expected as the Hoi waveform has a lower volumetric flow rate in comparison to the Gwilliam waveform. No statistical difference was seen in the TA-WSSMin between both waveforms: p-value 0.09 (95%CI: -0.01 – 0.11).

For the assessment of differing waveform's impact on characteristic outcomes, the Hoi vortex and WSS values were not directly substituted into the data set. The available ages of the cases in our data set fell in-between the age ranges of the Gwilliam and

Model	AUC(95% CI): Gwilliam (only) - Gwilliam+modified	Accuracy: Gwilliam (only) - Gwilliam+modified
All Indices	0.78(0.64-0.90) - 0.76(0.60-0.90)	0.85-0.82
WSS and Vortex	0.61(0.39-0.84) - 0.64(0.42-0.86)	0.77-0.79
Geo. and Vortex	0.70(0.54-0.87)-0.61(0.39-0.81)	0.77-0.77
Vortex	0.62(0.37-0.86)-0.58(0.35-0.82)	0.78-0.80

Table 5.3
Comparison of AUC and accuracy values of statistical characterization outcomes from the Gwilliam waveform data only, and the Gwilliam+modified waveform data.

Hoi waveforms ($\sim$ 45 years) and an age-appropriate waveform was not available. To account for this, the generated values for STAWSS, TA-WSSMin, TA-WSSMax, OSI, TA-LSA, TA-LSAstd, TA-DVO, DVOSTd, VtV, and NSV (systolic values) from both waveforms (for selected cases) were taken, and their midpoint value was used as an assumed 'age-appropriate' outcome: this was considered a 'modified' output. These modified outputs were substituted into the data table for the four selected cases, and statistical characterization modeling was performed in identical manner as the initial analysis (Gwilliam waveform data only). Comparison of outcomes with the Gwilliam or Gwilliam+modified waveform data, showed slight changes in accuracy: reduced accuracy when using all indices, but slight increased accuracy for the WSS+vortex or vortex alone model(s). The largest degree of change in AUC was seen in the geometry + vortex model with a decrease from 0.70 to 0.61, yet no change occurred for the overall accuracy. The resultant differences between the Gwilliam data outcomes and the Gwilliam + modified data can be seen in Table 5.3

5.7 Discussion

Initial analysis of our available MCA data, while not a robust enough study to suggest modifying clinical practices in the assessment of MCA IA rupture potential, findings suggests that the addition of vortex indices alongside geometric+WSS indices into a statistical model helped to improve the differentiation of unruptured and ruptured IAs. The sole application of geometric indices applied in a plethora of studies, showed to be the strongest index group for properly distinguishing ruptured from unruptured IAs in our data set. Yet geometric indices in this study had limited success in properly identifying ruptured aneurysms, as well as misidentifying 10% of unruptured IAs. If geometric indices were solely applied to assess the likelihood of rupture, such outcomes would leave many at-risk aneurysms without needed clinical intervention, as well as exposing many patients with low-risk IAs to an invasive interventional procedure. WSS-based models in this study had significant difficulty identifying ruptured IAs. Specifically our WSS-model tended to predict almost all IAs as unruptured, unable to distinguish characteristics indicative of ruptured IAs. However, due to the unbalanced number of unruptured and ruptured IAs in our data set (almost 3:1), this underestimation of ruptured IAs still resulted in an accuracy of 0.74 even though such models only correctly identified 2% of ruptured IAs. This outcome is consistent with the theory that both ends of WSS extrema may contribute toward IA rupture, making such indices of problematic use on their own [228]. The combination of both

commonly used geometric and WSS characteristics into a predictive model also had a reduced outcomes when compared with geometric characteristics alone. It is worth considering, the choice of condensing the WSS information across the IA sac to single numeric indices (WSS average, extrema, low-WSS coverage, mean OSI) may obfuscate stressor spatial information that would prove beneficial for predictive modeling, contributing to the minimal success of current WSS indices.

In this work, the goal was to determine how the spatiotemporal characteristics of swirling patterns in the bulk flow of IAs can be used to improve models for differentiating ruptured and ruptured IAs among medium-sized MCA IAs. Current work suggests the combination of IA geometric and near-wall WSS characteristics to discern the likelihood of an IA to rupture have limitations. Solely relying on vortex characteristics, while having improved overall outcomes (accuracy 0.78) over WSS indices (accuracy 0.74), were found lacking in comparison to established geometric indices and had reduced success in properly identifying ruptured IAs versus a combined geometric+WSS model. This indicates that vortices alone are not a suitable replacement for IA geometric or WSS characteristics concerning rupture assessment. Yet the inclusion of vortices alongside the geometric+WSS model helped to overcome some of the limitation present in said combined model: specifically helping to improve upon the proper identification of unruptured aneurysms (up to 99% accuracy). Yet the addition of vortex indices to the geometric+WSS model has no significant

impact on improving the identification of ruptured IAs: 44.5% to 43.5% ruptured accuracy for geometric+WSS and geometric+WSS+vortex model respectively. Given medium-sized IAs are common and their management strategies are arguably the most difficult, quantifying the spatiotemporal characteristics of the bulk-flow within such IA sacs may provide useful information often overlooked in the assessment of ruptured and ruptured IAs.

Although our overall study design is appropriate for a feasibility study, there are some limitations. The first limitation is that only a small number of MCA were used, and further understanding of vortex characteristics indicative of both ruptured and unruptured IAs may be achieved upon the introduction of additional cases. From a perspective of statistical characterization, a 1:1 ratio between binary outcomes (unruptured and ruptured IAs) is optimal for SVM [279], with many studies having a closer 1:1 ratio [356, 385]. Removing unruptured IAs from the data set available for this study to create a 1:1 ratio was not performed as only 24 cases would remain; a number inadequate for robust statistical characterization. In a secondary analysis of characterization sensitivity, we found that even a slight reduction in the overall number of unruptured cases led to undesirable outcomes. Using leave-one-out validation, the analysis was performed on both our entire data set and a reduced data set where 3 randomly selected unruptured aneurysm cases were removed. This was performed over 100 iterations and the 3 removed cases were changed each iteration. For each iteration, the total accuracy of the model was calculated. The cumulative average

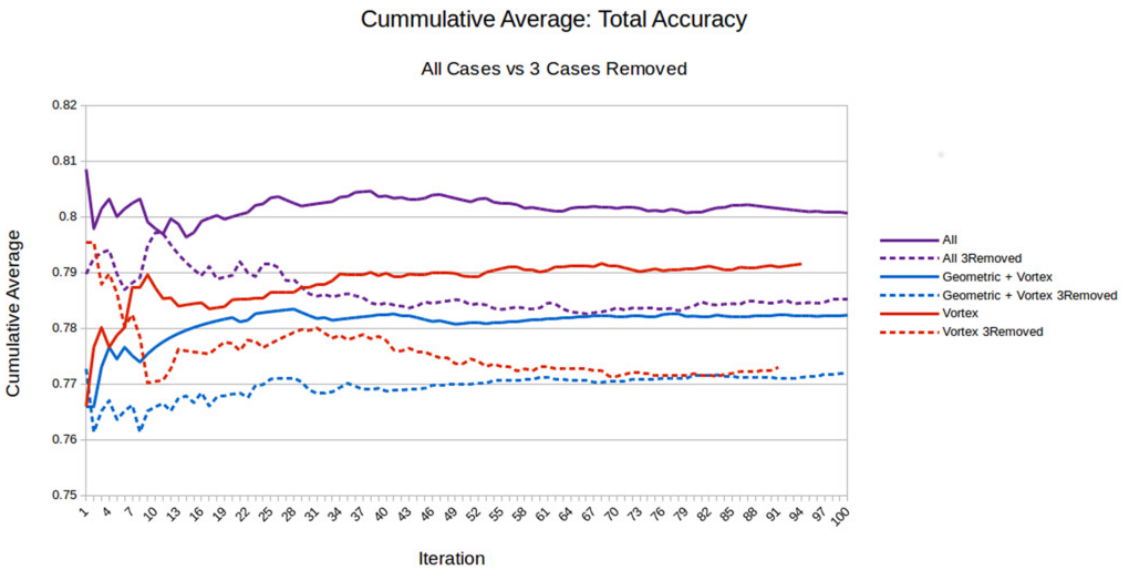

Figure 5.5: The cumulative average of the total accuracy for vortex, geometric+vortex, and all models using our data sets with no cases removed (solid lines) and 3 unruptured IA cases removed (dotted lines). For each model, the removal of 3 cases caused a lower total accuracy compared to its counterpart where no cases were removed.

for the total average was calculated across all 100 iterations, limiting the impact of a possible outlier from skewing the assessed strength model outcomes (The removal of just 3 cases lowered the ability of models to accurately differentiate ruptured from unruptured aneurysms (Figure 5.5).

This sensitivity to the removal of data would inhibit the ability to perform a relevant analysis using a 2:1 or 1:1 ratio data set given the currently available cases. Additionally, given the size of the current data set, it would prove impossible to determine if model outcomes were solely due to the reduction of the number of cases, or if our chosen indices had less ability to correctly differentiate unruptured and ruptured IAs than is currently suggested by our analysis. To properly determine the impact that

the binary outcome ratio has on MCA IA analysis, additional ruptured cases will need more robust data set as opposed to the removal of unruptured cases from currently available cases.

Second, this work reveals that, while the strongest generated model benefited from the application of quantitative analysis of vortex characteristics alongside IA geometric and WSS indices, the said model has room for improvement: only identifying 43.5% unruptured IAs. Relying on idealized flow waveforms may constrain the characteristics of generated vortices in IAs, reducing their usefulness in statistical characterization. To improve upon these findings, measured patient flow waveforms should be used as inlet boundary conditions for simulations as they would better represent the flow patterns inherent in patient IAs. The choice of assumed vessel rigidity may also impact simulated outcomes. While the vascular structures were taken from pre-existing medical imaging, information regarding varied patient vessel stiffness, often an impact of vascular pathology separate from a developed IA, was unavailable. Due to this lack of information, vessel compliance could not be accurately simulated on a case by case basis. Assumed vessel rigidity for simulated hemodynamics is an often employed methodology, knowing that such assumptions increase pulse wave velocity [203] and WSS in a rigid vessel [7] though similarities are observed in WSS distribution and low WSS areas between both types of simulations in arterial flow [303]. Yet recent studies suggest that differences exist in near-wall velocity patterns in compliant versus rigid IA simulations while bulk-flow aneurysmal patterns remain similar

[335]. It is worth noting that variability in collagen architecture and the mechanical strength of IAs vary even across the dome of a given unruptured IA [278], indicating that simulating uniform vessel compliance across an an IA wall may cause unintended errors in characterization model outcomes. Additionally, backwards traveling waves can occur within the vascular system, especially at secondary outlet vessels connected to the parent artery, and are impacted by vessel wall compliance. Unfortunately, less is know to what extent these potential backwards traveling waves impact IA flow. However, in earlier studies by a research group involving my advisor [156], simulation methods were compared with phase-contrast magnetic resonance imaging in two intracranial aneurysms. The gross hemodynaimcs obtained from *in vivo* measurements (with the influence of backward-traveling waves) was comparable to CFD simulation results without the consideration of the pulse wave, suggesting that such backward-traveling waves may have minimal impact on aneurysmal bulk flow. Further studies are required to determine if the degree of IA compliance impacts quantified vortex characteristics and the outcomes of statistical characterization, especially in the even of varied compliance across the same IA dome/possible wave reversal.

Third, only angiographic data post-rupture was available for the ruptured IAs in this work. I recognize that slight variations in IA geometry may occur post-rupture. Such changes could alter the distribution and intensity of WSS across the IA wall and/or the characteristics of vortices. Yet less is know to when such geometric changes will

occur: shortly before IA rupture, during rupture, or post-rupture. Thorough investigations in this matter are on ongoing [286, 305], and further work on how altered IA sac geometry post-rupture impacts vortex characteristics should be investigated. Additionally, while this work highlights the need to assess bulk-flow patterns of ruptured IAs, further work is needed to determine if the spatiotemporal characteristics of vortices can improve the characterization of unruptured IAs likely to expand or rupture. Longitudinal studies constituting hemodynamic analysis of unruptured IAs and noting the vortex characteristics of those which remain stable versus those that grow or rupture within a given period could give novel insight into the nature of this pathology.

Although our CFD-simulated parameters, including vortex-related parameters, did not show significant improvements in terms of IA rupture characterization, the use of CFD for rupture risk assessment still could be meritorious as the current analysis of hemodynamic parameters is sub-optimal. For instance, the choice of condensing the WSS and vortex information across the entirety of the IA sac to single numeric indices such as averages, extrema, or low-WSS coverage, may obfuscate spatial information that would prove beneficial for statistical characterization, contributing to the minimal success of current indices. Looking forward, more innovative machine learning methodologies are recommended to maximize the information obtained through CFD simulations.

5.8 Conclusion

The application of quantified spatiotemporal characteristics of hemodynamic vortices within medium-sized MCA IAs was performed to determine their impact on models for differentiating unruptured and ruptured IAs. Current models using geometric and WSS based indices may have inherent limitations when applied to medium-sized IAs. It was found that a combined geometric and WSS based model could be strengthened upon the inclusion of vortex indices, giving credence to the need for a further understanding of the bulk-flow hemodynamic characteristics in the IA sac and their relation to IA rupture. While this feasibility study is not enough to justify changes to current clinical decision-making concerning assessing IA rupture risk, quantifying the spatiotemporal characteristics of vortices may contain useful information overlooked by assessing only the geometric and near-wall flow stressors within IAs. Continued use of the identification of vortices and adapting their quantified spatiotemporal characteristics into statistical characterization using larger data sets may one day uncover information that can help clinical decision making concerning the assessment of, and determining optimal treatments, for IAs.

5.9 Acknowledgements

The study was partially funded by a research contract through Siemens Medical Solution (USA) Inc. (Jiang), a pre-doctoral fellowship from the American Heart Association (18PRE33990321; Kevin Sunderland), a grant from the National Key Research and Development Program of China (2016YFC1300703; Qinghai Huang) and funding from the College of Engineering at the Michigan Technological University (Jiang).

Chapter 6

Impact of Vortex Spatial and Temporal Stability on Vascular Endothelial Cells

Pathological weakening of the vascular wall, a known component of IA development and possible rupture, is precluded by alterations to cellular functionality. From the perspective of hemodynamics triggering such changes, significant attention is given

to the inner most (intimal) layer of the cerebral vasculature comprised of an endothelial cell (EC) monolayer. As mentioned in Chapter 1 the vascular EC monolayer comes into direct contact with blood flow and serves a dual purpose: hemodynamic mechanosensors which transduce fluid force stressors into biochemical signal cascades[46, 92], and act as a selectively permeable barrier to plasma solutes and biomacromolecules ($>3nm^3$) as to limit the invasion of leukocytes and monocytes into the vascular wall[44, 71, 168, 242]. Multiple *in vivo* and *in vitro* studies have demonstrated that laminar hemodynamic flow promotes healthy EC physiology, helps maintain cell-cell adhesion complexes, and limits the transport of inflammatory molecules into the vascular media layer [37, 50, 68, 210, 230]. Whereas vortical flow negatively impacts ECs, altering the cellular monolayer and its ability to maintain vascular health, leading to a weakening of the localized arterial tissue. While a full exposition into the cellular changes triggered by vortices is beyond the scope of this dissertation, alterations to cell-cell adhesion, cell inflammatory adhesion markers, and increased cellular death (apoptosis) are known to occur in vortical flow, contributing to the development and possible rupture of IAs.

Vascular endothelial (VE)-cadherin is an EC specific adhesion molecule that supports cell-cell junctions. In laminar flow, these transmembrane proteins aggregate to cellular peripheries and bind to one another to form well-defined connections between ECs [229]. These connections promote vascular stability, regulate cellular

turnover and/or cellular growth, and helps reduce cellular apoptosis[271]. Hemodynamic vortices in turn cause a breakdown in VE-cadherin junctions, triggering a loss of EC functionality[258, 287]. Also, while not directly tasked with the maintenance of vascular permeability, the breakdown of VE-cadherin connections lead to decreased regulation of macromolecules into the vessel wall as gaps now exist in the EC monolayer[95, 229].

In a healthy vessel, the EC monolayer maintains antiatherogenic characteristics, inhibiting platelet and inflammatory cell adhesion along the arterial wall, limiting their invasion into deeper layers of the vessel[5]. Increased arterial inflammation has shown to be a significant factor in the pathogenesis of IAs and their potential rupture [54, 139, 302]. Specifically, increased leukocyte and macrophage infiltrates in the vessel wall give rise to proteases which degrade elastin [79] and trigger the breakdown of exracellular matrix proteins [11, 188, 333, 339], weakening the strength of the arterial wall. One of the molecules involved in the adherence of inflammatory cells, impacting their ability to infiltrate into deeper layers of the vessel, is vascular cell adhesion protein 1 (VCAM-1) [104]. This cell-surface protein allows for the binding of leukocytes, monocytes or basophils, which trigger alterations to EC shape, aiding in the migration of such proteins into deeper layers of the artery as the altered shapes creates gaps in the cellular monolayer [74]. VCAM-1 is shown to have low expression in laminar, atheroprotective hemodynamic conditions [352], whereas low stressor flow vortices induce heightened VCAM-1 expression [275].

When exposed to disturbed hemodynamic flow, the breakdown of cellular physiology and altered functionality can result in the EC endoplasmic reticulum losing the capacity to correctly fold cellular proteins. Instead, stress receptor-bound proteins are released which signaling cellular death (apoptosis) [215]. One such family of proteins are cysteine proteases (caspases) [70, 256, 288]. Active (cleaved) caspase-3 degrades multiple cellular proteins and triggers fragmentation of EC DNA, leading to cellular death[226]. Increased cellular apoptosis exacerbates many of the aforementioned arterial changes: altered regulation of vessel permeability and reduced ECM proteins/vessel mechanical strength. *In-vitro* studies have shown that the prolonged exposure to vortical flow causes a marked increase of cleaved caspase-3 production over cells exposed to laminar flow [288].

While such deleterious alterations to cells are imparted by vortical flow, the study of such patterns is typically reserved to assessing differences between vortical and laminar flow, with limited focus given to the characteristics of vortices. The study and understanding of hemodynamic vortices' on ECs have been facilitated in no small part by specialized *in vitro* parallel plate flow chambers (PPFCs). PPFCs allow the generation of controlled flow patterns onto cultured cells, while having reduced cost and complexity than *in vivo* animal models[68, 176, 368]. The inclusion of a "step-down" section following a PPFC inlet was found to generate an area of low shear ($<$ 2 dynes/cm^2) vortical flow, followed by subsequent areas of flow reattachment and resumed laminar flow [123]. Such chambers have allowed the investigation of both

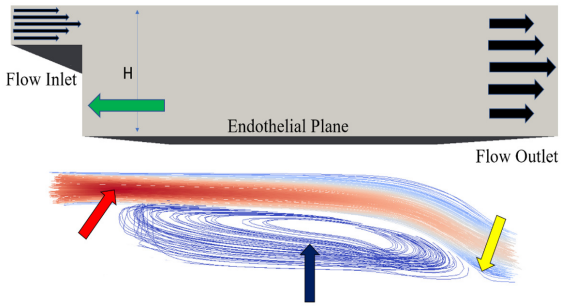

Figure 6.1: CFD simulated example of a "step-down" of a PPFC. Step-down area, flow inlet, flow vortex, and area of flow re-attachment identified with a green, red, blue and yellow arrow respectively. Simulation data was generated using ANSYS-FLUENT (version 19.0)

disturbed and laminar flow within a single chamber as can be seen in Figure 6.1. Despite PPFC's usefulness, they are not without limitations: only one vortex flow pattern is typically generated and it remains spatially and temporally stable during experimentation. Yet such highly stable vortices within the hemodynamic environment are unlikely in part due to the complex geometry of arterial areas known to generate vortical flow (vasculature curvature and the aneurysmal sac) and the pulsatile nature of hemodynamic flow rates in the arterial system. Generation of these relatively simplistic vortices (in PPFCs) in relation to their *in-vivo* counterparts may give a constrained understanding of how the characteristics of vortical flow impact levels of cellular changes. As shown in Chapter 5, the spatiotemporal characteristics of flow vortices are useful in differentiating ruptured from unruptured IAs, though that work gave no information regarding to what degree (if any) differing vortex characteristics/stability impart divergent levels of EC change. Assessment of flow vortices of varying stability onto arterial cells could lead to novel insight of IA pathology.

For the final aim of this dissertation, a modified PPFC with an array of obstacles (baffles) introduced along the flow path to disrupt flow and generate multiple areas of vortices onto cultured ECs was designed. CFD simulated flow within this chamber, and the CE method developed in Chapter 2 quantified the spatial and temporal stability of distinct areas of vortical flow. Combining these *in-silico* and *in-vitro* methods allow the application of vortices of known characteristics onto cultured ECs, giving insight into how such patterns may lead to differing degrees of cellular change(s). This aim focuses on highlighting how the stability of vortices impact the degree of change to VE-cadherin, VCAM-1 and cleaved caspase-3 expression in human umbilical vein endothelial cells (HUVEC). A greater understanding of the impact that hemodynamic vortices of varied characteristics have on cellular/arterial changes will not only lend validity towards my earlier work, but also help elucidate novel information concerning the nature of IA development, growth and rupture.

6.1 Methods

6.1.1 Parallel Plate Flow Chambers

For this work, two chambers were designed: one generating laminar flow and one disturbed flow.

Typical PPFCs incorporate two plates spaced at a fixed height to create a flow channel, with Equation 6.1 governing the relationship between channel geometry, volumetric flow rate, and resultant WSS as described by Hochmuth et al. [143].

$$\tau = \frac{6Q\mu}{WH^2} \tag{6.1}$$

Q as the flow rate, W and H as chamber width and height respectively, μ (in Poise) as fluid dynamic viscosity, and τ as shear stress (dynes/cm^2). The laminar flow chamber for this works was designed with dimensions of 14.5cm x 2.4cm x 0.045cm for length, width and height respectively. Based off of these dimensions and Equation 6.1 a flow rate of 40 ml/min was used to achieve a WSS value of 7.5 dynes/cm^2. A recesses was made in the bottom portion of the chamber to hold a glass slide: 7.5cm x 2.5cm x 0.1cm (l,w,h). This recess was made 5.5cm from the flow inlet, allowing initial flow irregularities to be "washed out" and corrected to laminar flow before reaching the cell slide. For the disturbed flow chamber, a design based off an expanded section chamber [173, 239] and maze channel reactor[124] was utilized. The main body of the flow chamber consists of an inlet and outlet connector of 0.3cm inner diameter, and an expanded inner chamber of 7.5 cm x 2.5 cm x 0.4cm (l,w,h). The increased height of the disturbed flow chamber versus the laminar chamber was specifically designed to create low WSS throughout the chamber ($<$ 1 dynes/cm^2). As WSS values may impart differing levels of changes to ECs [228], a very low WSS throughout the chamber was chosen to ensure that disturbed flow characteristics would be the

main difference between analyzed areas. The chosen inlet flow rate for the disturbed chamber was set to 26.5 ml/min, allowing for a 15 dynes/cm^2 WSS at the inlet based on Equation 6.2 [80], followed by a sudden reduction in stressors within the chamber, better mimicking WSS changes in values between the parent vessel and a developed IA [354].

$$\tau = \frac{32 * Q}{\pi * D^3} \tag{6.2}$$

Q is the volumetric flow rate (μl/sec), D is the diameter of the inlet (in mm). The flow chambers were milled out of autoclavable polycarbonate plastic (McMaster-Carr, product 8574K) by the Michigan Technological University Machine Shop. Diagrams of the chambers can be seen in Figure 6.2.

The internal baffles required to generate flow vortices within the (disturbed) chamber were molded out of a bioinert polymeric organosilicon polydimethylsiloxane (PDMS): (Sylgard R 184, 10:1 w/w base to curing agent). Utilizing PDMS also enabled baffles to undergo slight deformation when sealing the PPFC, lessening the change of cracking the cell plate. Four internal baffles of 0.5 x 1.5 x 0.3cm (l,w,h) were created, with each baffle 1 cm apart and connected by a 0.1cm thick ceiling, bringing the total height of the baffle structure to match the height of the disturbed chamber.

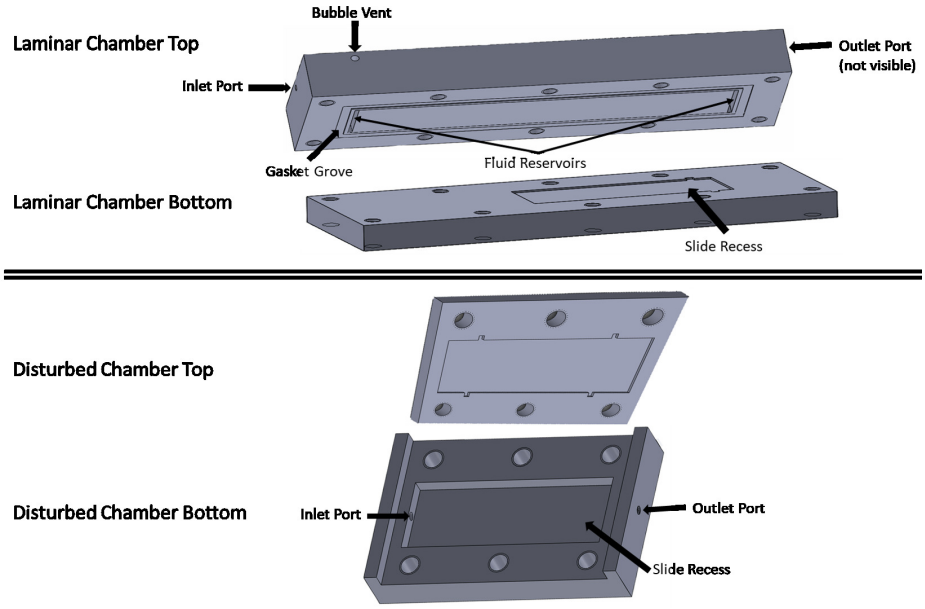

Figure 6.2: Diagram of the laminar parallel plate and disturbed flow chamber. Both chambers contain a slide recces in their bottom plate to allow the placement of a EC-seeded glass slide. The diameter of the inlet and outlet port of each chamber (and bubble port for the laminar chamber) is 0.3cm , while the height of the flow area is 0.045cm and 0.4cm for the laminar and disturbed flow chamber respectively. A silicone gasket is placed between the top and bottom plates of (each) chamber to ensure a water tight seal. The top and bottom plate of each chamber is held together by stainless steel axle bolts and wing nuts.

6.1.2 Computational Fluid Dynamics

CFD simulations were performed to generate velocity flow data and assess the stability of vortices within the proposed channel designs. 3D models were created in OpenSCAD (OpenSCAD-2019.05 x86 64-bit) and saved as STL files. These models were imported into the ANSYS-FLUENT(Version 19.0) software package and converted into volumetric meshes. The Navier-Stokes equations was numerically solved, with the simulated fluid considered incompressible, Newtonian, and having properties

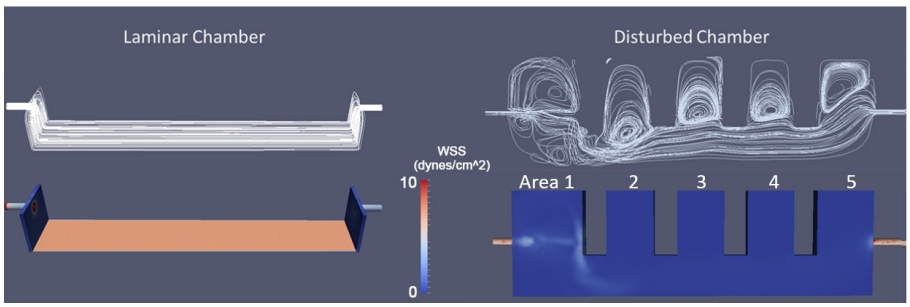

Figure 6.3: Outcomes of simulated flow chambers: flow velocity streamlines (white lines) and WSS (dynes/cm^2) of Laminar and Disturbed flow chambers. Example is for one time step.

mimicking cell culture medium: 998 kg/m^3 density and 0.9 x10^{-3}Pa·s dynamic viscosity. To simulate the flow pattern generated by the peristaltic pump, video was taken of pump-generated flow through a direct reading flowmeter (Cole-Parmer). Motion tracking of the flowmeter ball in the video was performed by the Kinovea analytic software (Kinovea-0.8.15, Joan Charmant & Contrib.) and converted into the volumetric flow rate over time. A user defined function for FLUENT was created based off the calculated temporal volumetric flow rates and used to generate inflow boundary conditions mimicking the oscillating flow pattern of the peristaltic pump. Flow was simulated for 3 seconds at 1000 time-steps per second, with 20 equally spaced time points saved across the final time step for analysis. Outcomes of simulated models can be seen in Figure 6.3

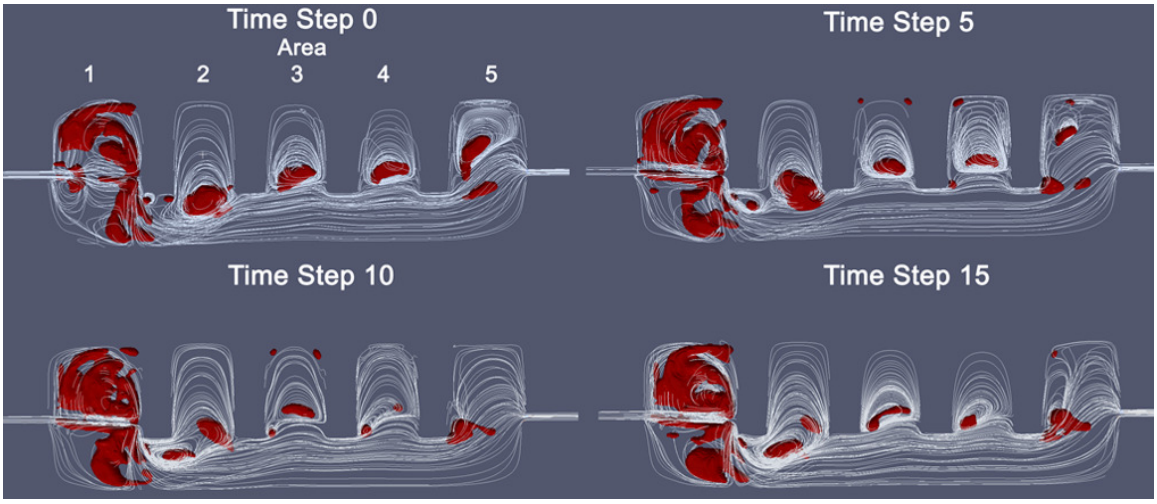

Figure 6.4: Simulated flow within the disturbed PPFC. Streamlines (white lines) and 3D *isosurfaces* (red) highlighting the areas identified as vortices using the developed CE method. Time steps 0, 5, 10, and 15 shown.

6.1.3 Quantification of Vortex Spatial Temporal Characteristics

Analysis of the simulated velocity flow patterns within the proposed disturbed chamber was performed prior to any *in-vitro* experimentation to ensure areas of vortices with varied spatial and temporal characteristics were generated. Using the CE method described in Section 2.3, five (5) distinct regions of each simulated chamber were isolated and the vortices in each area were analyzed (Figure 6.4). The TA-DVO value (as explained in 2.1.4) was calculated for each region and their values are reported in Table 6.1.

Flow Area	Disturbed FlowTA-DVO±Standard Deviation
Area 1	0.743±0.11
Area 2	0.763±0.05
Area 3	0.625±0.14
Area 4	0.606±0.20
Area 5	0.672±0.12

Table 6.1
Calculated temporally-averaged DVO values from the simulated disturbed flow chamber. No DVO values were calculated in the laminar chamber simulation as no vortices were generated.

6.1.4 Cell Culture and Flow Chamber Experiment

Passage 4-5 human umbilical vein endothelial cells (HUVECs: Lonza, Walkersville, MD), a cell line prominently used in *in-vitro* studies assessing flow and its impact on ECs, were seeded at a density of 25,000 cells/cm^2 onto a 75x25mm microscope slide (Fisher Scientific, Waltham, WA). Prior to cell seeding, slides were coated with a 20 μg/mL bovine collagen (Sigma Aldrich, St. Louis, MO) solution prepared in 0.01 M hydrochloric acid for 2 hr at room temperature. Cells were cultured in endotheilial cell growth media (EGM, Lonza) which was changed every two days, and were maintained in a 5% CO_2, 20% O_2, 37°C incubator. Upon cells reaching 80% confluence, a slide was placed into the bottom of a flow chamber, the PDMS baffles were place on top of the slide (in the disturbed camber), and the top plate is screwed to the bottom plate, with a silicone gasket between the top and bottom plates to help achieve a water tight seal. The chamber was attached to a closed-loop system: peristaltic pump, cell culture media reservoir with a 2nm pore filter for gas exchange, and flow chamber (see Figure

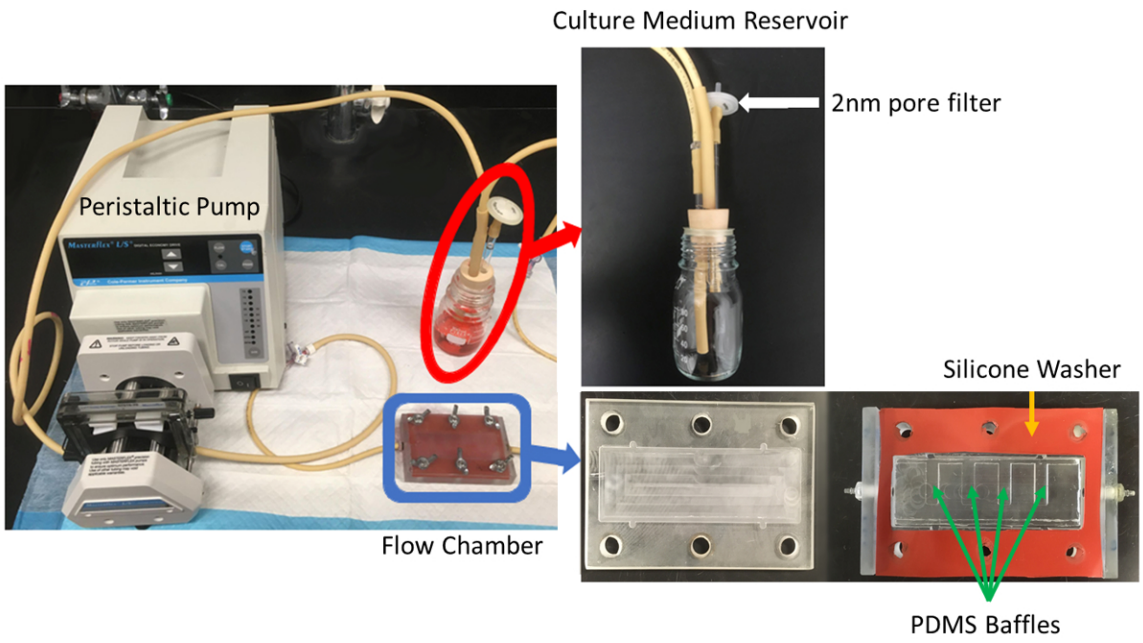

Figure 6.5: Setup of flow chamber for experimentation. A Masterflex L/S peristaltic pump (Cole-Parmer, Vernon Hills IL, USA) generated flow in a closed loop system, drawing cell culture medium out of a reservoir (red circle) with a 2nm pore filter for gas exchange (white arrow) and into the connected disturbed flow chamber (blue square) with inserted PDMS walls (green arrow) and silicone washer (yellow arrow). Two, 3-way stopcocks were added pre and post the flow chamber to allow the removal of any bubbles from the flow system.

6.5). The assembly of the closed loop system was done within a sterile laboratory hood to limit contamination. Flow experiments were carried out for 12 or 24 hrs in a 37 C° incubator with 5% CO_2 humidified atmosphere. For cells used as static flow control, a slide was cultured alongside those used for flow experimentation, and left in the culture dish for an additional 12 or 24 hours (dependent on experimental time point). After said time point was reached, the static cultured slide and flow experiment slides were processed: immunoflourescent staining or extraction and collection of cells (from culture slide) for analyzing protein concentration..

6.1.5 Immunofluorescence

The following procedure was followed for the immunoflourescent staining and imaging of cells. First, the cell slide was removed from the flow chamber post-experiment and rinsed 3 times with phosphate-buffered saline (PBS). Second, cells were fixed with 4% paraformaldehyde for 25 minutes, and nonspecific binding was blocked with a 1% bovine serum albumin, 0.2% Triton X-100 solution in PBS (blocking buffer) for 30 minutes. Third, slides were either incubated with a cleaved caspase-3 mouse monocolonal antibody (Cell Signalling 9664S, 1:100 dilution), VE-cadherin rabbit monoclonal antibody (Cell Signalling 2500S, 1:200 dilution), and-or VCAM-1 mouse monoclonal antibody (ThermoFisher Scientific MA5-11447, 1:100 dilution) overnight at 4°C. Fourth, the slides were rinsed 3 times with blocking buffer and incubated with goat anti-rabbit IgG Alexa fluor 488 (1:200 dilution) and anti-mouse IgG Alexa fluor 594 (1:200 dilution) secondary antibodies (R&D Systems Minneapolis MN) for 1 hour at room temperature. Fifth, cellular nuclei was stained with a 4',6-diamidino-2-phenylindole (DAPI) solution (1:1000 dilution) for 5 min at room temperature. Finally, cells were rinsed in PBS 3 times and the slides were mounted with a glass cover slip and aqueous mounting media. Immunofluorescent images were taken immediately after mounting with an upright BX51 Olympus epifluorescence microscope. For each of the five areas of interest, four sub-regions were selected and images were taken for each antibody at 10x 20x and 60x magnification.

6.1.6 Quantifying Protein Concentration

Commercial enzyme-linked immunosorbent assay (ELISA) kits (R&D systems) were used to detect cleaved caspase-3, VE-cadherin, and VCAM-1 in cell supernatant. After flow experimentation, the 5 areas of the cell slide were isolated with a glass cutter, and the separated areas were placed into individual petri dishes. 200μl cell extraction buffer was applied and cells were scraped off each isolated area. The cell/buffer supernatant was collected into individual microcentrifuge tubes, oscillated for 24 hours at 4°C, then stored in a -80°C freezer till all experiments were completed. Manufacturer's instructions were followed to perform ELISA analysis. Standards were run in triplicate and samples in duplicate. Optical density absorbance was measured at 450-570 nm using an absorbance plate reader (VERSAmax microplate reader, Molecular Devices, San Jose CA, USA). To account for for slight variations in the dimensions of the isolated areas (due to glass cutting), concentrations were normalized by their surface area against the 'ideal' surface area: 375mm^2. Measured values were also normalized by the estimated cell number for each area. As cell counts could not be directly estimated for the experiments in which cells were collected for ELISA analysis, cell counts were instead estimated by assessing the number of DAPI-stained cells in previously collected immunoflourescent images using the ImageJ image processing program. For each area, cells were counted and averaged across their four 20x images, and these averages were used as an assumed cell count(s) for subsequent

experiments per their flow condition: static, laminar, or disturbed. All counts were normalized to the cells slides in 12-hour static culture. Estimated protein concentrations of samples were determined by interpolation from a four-parameter logistic standard calibration curve (https://www.aatbio.com/tools/four-parameter-logistic-4pl-curve-regression-online-calculator). Concentrations were then adjusted for the supernatant dilution factor (5x) as samples were diluted prior to ELISA analysis to allow enough supernatant for all tests. Data were presented as fold change against cells subject to static control for the 12 hour time-point.

6.2 Results

Considering flow conditions within the disturbed flow chamber, Area 1 was markedly different from the other chamber areas. Due to its proximity to the fluid inlet: higher areas of WSS (Figure 6.3) and bifurcated flow pattern occurred within this area (as seen in Figure 6.6). Such characteristics are likely to alter the degree of cellular changes within the cultured HUVEC monolayer in relation to the other flow areas, confounding the interpretation of experimental outcomes. Recalling my work in Chapter 5, the application of quantified vortex characteristics was limited to only IAs of a similar type (bifurcation) and anatomical locale (M1 bifurcation of the MCA) as IA types/locals have been shown to have differing intraneurysmal flow patterns (Figure 6.6) and rupture rates [93]. For the purposes of this work, cells from Area 1 were not

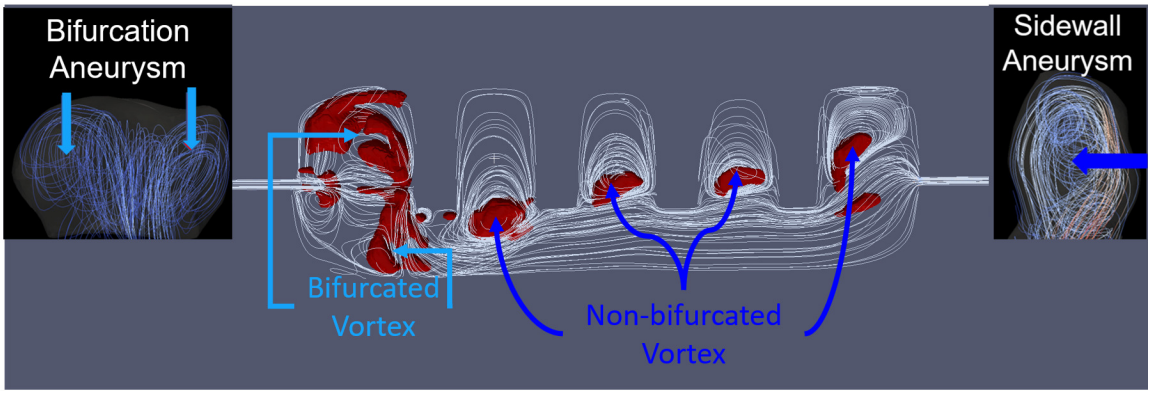

Figure 6.6: Differences in type of vortices between Area 1 and the other areas of the disturbed flow chamber. Area 1 generated a bifurcated vortex (similar to that of bifurcation IAs), as opposed to non-bifurcated vortices in the other areas. Non-bifurcated vortices were similar to patterns in sidewall IAs.

compared alongside the other chamber areas.

Additionally, Area 5 of the disturbed flow chamber was noted as having irregularities in experimental outcomes. Immunoflourescent imaging of cells exposed to disturbed flow noted that significant cellular loss was often noted in Area 5. This loss of cells was not seen across the other areas of the cellular monolayer in the same experiment, nor did this loss in Area 5 occur across all disturbed flow experiments as seen in Figure 6.7. Current rationale to the triggers for such (occasional) loss of cells in Area 5 is that it may result from irregularities in flow conditions near the chamber outlet or weakened adherence of cells towards the outer edge of cultured slides. Weakened initial adherence coupled with slow WSS vortical patterns may cause cells to detach at a higher rate at the edge of a culture slide, even when compared to the other end of the slide (Area 1) with its faster flow rate due to its proximity to flow inlet. Further work is required to determine the cause(s) of cellular detachment in Area 5. As the

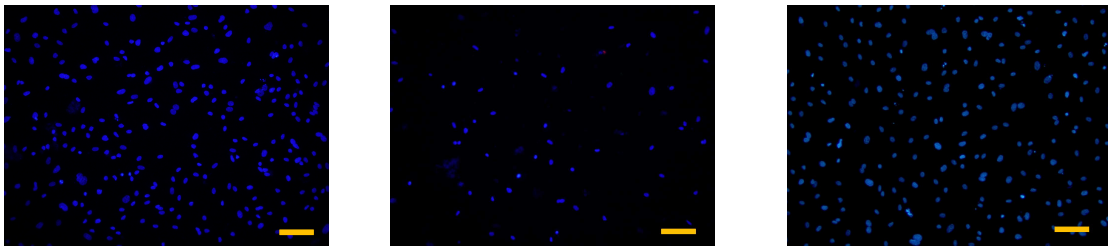

(a) Area 3 (b) Area 5 (detached) (c) Area 5 (attached)

Figure 6.7: Immunoflourescent staining of cellular nuclei via DAPI (blue) an distinct areas of the disturbed flow chamber. Areas **a)** 3 and **b)** 5 of the same experiment, with Area 5 showing significant cellular loss. **c)** Area 5 of a different experiment, showing significant cellular retention versus b). Scale bar is 100μm

degree of cellular loss could not be reliably confirmed for experiments in which cells were collected for ELISA, Area 5 was excluded from analysis for the purposes of this work.

6.2.1 Morphological Alterations to Cells in Flow

Visual analysis of immunoflourescent images reveal morphological alterations for cells dependent on their flow conditions can be seen in Figure 6.9A. In static culture and laminar flow, cells show well-defined cell-cell adhesion complexes (VE-cadherin), whereas disturbed flow causes significant gaps in cell adhesion as seen in Figure 6.9A. After 24 hours of flow exposure, slight cellular loss was seen in laminar flow, yet VE-cadherin still showed aggregation towards cell peripheries and a degree of retention to the well-connected monolayer. Cells exposed to disturbed flow for 12 hours showed significant gaps to be seen within the cellular monolayer, with further exacerbation

after prolonged (24 hour) flow. ECs within healthy areas of the arterial system are also found to be aligned toward flow directionality, while in atherosclerotic-prone regions, ECs do not show distinct orientation to flow. To determine cell's alignment to flow, the angle between the longest distance across the boundary (Feret's diameter) of DAPI stained cell nuclei and the horizontal axis of the image was measured (using ImageJ). Analysis of images reveal HUVECs exposed to laminar flow were highly oriented to the direction of flow with 64.5±1.76% of cells having an orientation angle between -30 and 30deg. Disturbed and static-culture control HUVECs showed no distinct flow orientation, with 31.4±6.58% and 40.5±3.39% cells (respectively) oriented between -30 and 30deg (Figure 6.9B). These changes to cellular orientation to flow is mirrored in previously published work [265, 349]. Additionally, the distinct areas of the disturbed flow chamber were investigated individually to determine if vortex stability alters the degree of orientation. Figure 6.8 shows immunoflourescent staining of cells in Areas 1-4 of a disturbed flow experiment and the resultant circular histograms of their cellular orientations. The normalized entropy value (Equation 2.6) of cell orientation was calculated to assess the variation of (probable) cellular directionality between the areas of vortices: higher entropy values contain a greater degree of variation in cell directions / less distinct orientation. The differing areas of vortical flow where found to have equivalent normalized entropy values, regardless of vortex stability: normalized entropy values can be seen in Table 6.2

In addition to alignment towards flow, ECs demonstrate the capability to elongate

in relation to stressors and flow directionality. Analysis of cellular VE-cadherin in immunoflourescent images demonstrated that HUVEC's aspect ratio (ratio of long axis to short axis) in laminar flow was significantly increased versus those exposed to disturbed flow: t-test p-value < 0.05 as is seen in Figure 6.9 C. In comparison, cells exposed to disturbed flow showed similar aspect ratios to HUVEC in static culture. This was expected as the lack of uniform flow directionality and low shear stress in disturbed flow minimizes the ability of cells to elongate.

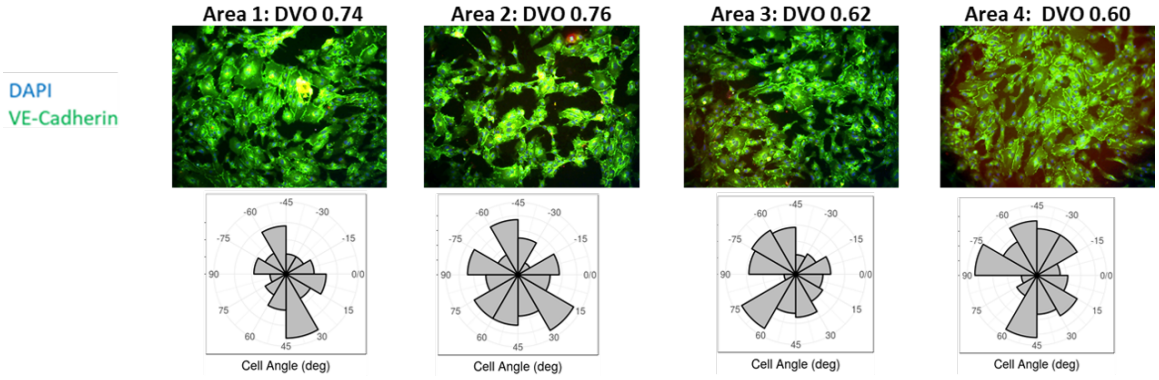

Figure 6.8: Orientation of HUVEC cells exposed to flow vortices of varying stability (TA-DVO) in the designed PPFC. Immunoflourescent staining of VE-cadherin (green) and DAPI (blue) of four (4) distinct areas of flow vortices and their resultant circular histogram of cell nuclei orientation to horizontal axis of images.

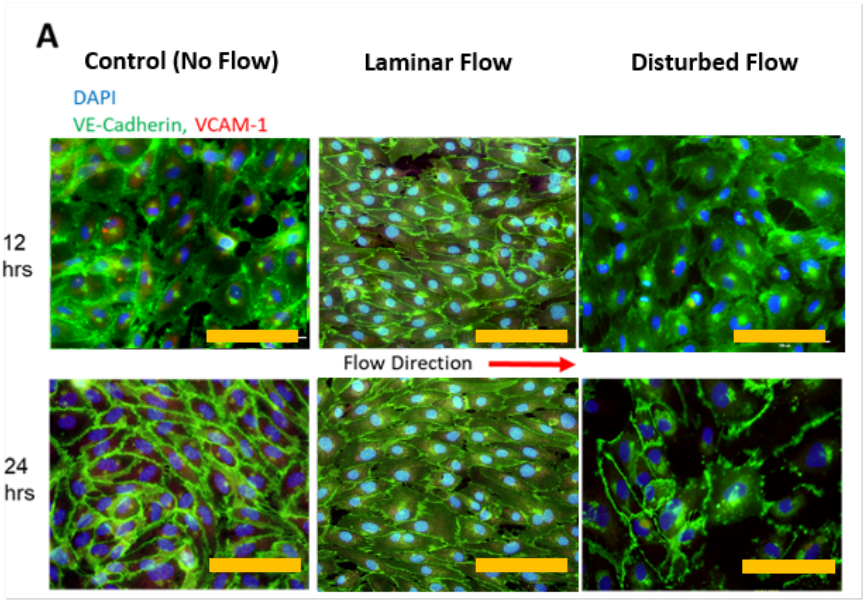
A
Control (No Flow)
Laminar Flow
Disturbed Flow
DAPI
VE-Cadherin, VCAM-1
12 hrs
24 hrs
Flow Direction

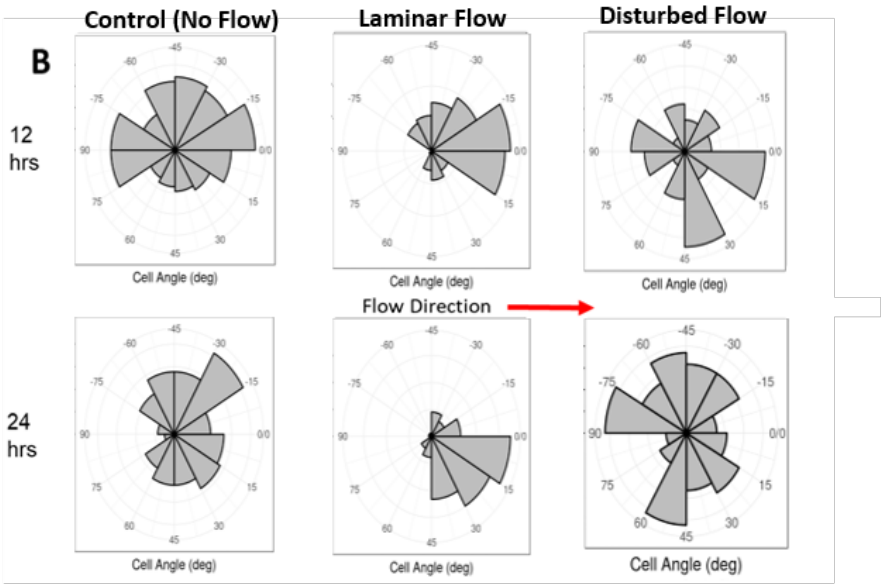
B
Control (No Flow)
Laminar Flow
Disturbed Flow
12 hrs
24 hrs
Flow Direction
Cell Angle (deg)

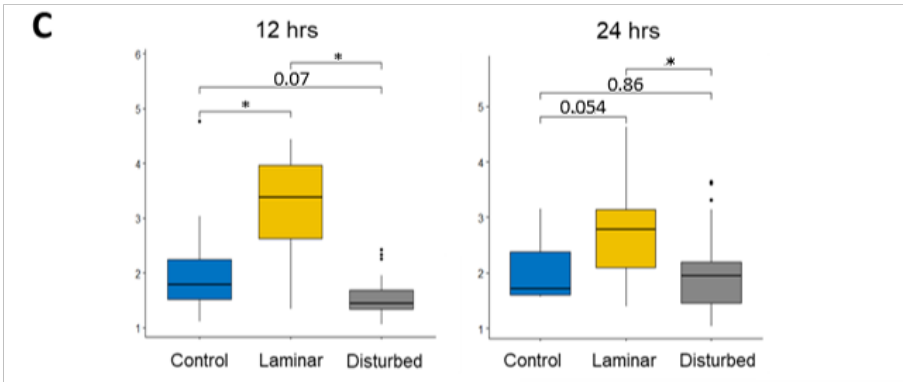
C
12 hrs
24 hrs
0.07
0.86
0.054
Control
Laminar
Disturbed

Flow Area: TA-DVO	Normalized Entropy
Area 1: 0.74	0.967
Area 2: 0.76	0.976
Area 3: 0.62	0.971
Area 4: 0.60	0.973

Table 6.2
Normalized entropy of cellular angle (in relation to the horizontal axis of immunoflourescent images) of HUVECs in 4 areas of disturbed flow with varying temporal stability (TA-DVO).

Figure 6.9: Morphological analysis of changes to HUVEC cells in vortex flow. **A)** Immunoflourescent staining of cells in flow conditions: (blue) DAPI, (green) VE-cadherin, (red) VCAM-1, (yellow) scale bar at 100nm. **B)** Circular histogram of cell angle in relation to flow direction. Histograms are constrained between -90 and 90 °. **C)** Comparative boxplots of cellular aspect ratios: * indicates statistical significance, p-value < 0.05.

6.2.2 Protein Concentration versus Flow Conditions

HUVECs subjected to laminar and disturbed flow were evaluated for their fold change of VE-cadherin, VCAM-1, and cleaved caspase-3 compared to cells in static culture. Outcomes of this analysis can be seen in Figure 6.10

VE-cadherin is of vital importance for the maintenance and control of the endothelial cell monolayer via cell-cell adherence, while also aiding in the maintenance vascular permeability. In this work, expression of VE-cadherin was shown to decrease when exposed to laminar flow in relation to static control. An averaged 0.33 ± 0.12 fold reduction was seen in EC VE-cadherin after 12 hours of laminar flow exposure, whereas exposure for 24 hours resulted in continued and statistically significant (p-value < 0.05) reductions in comparison to its 12 hour counterpart: 0.75 ± 0.07 fold

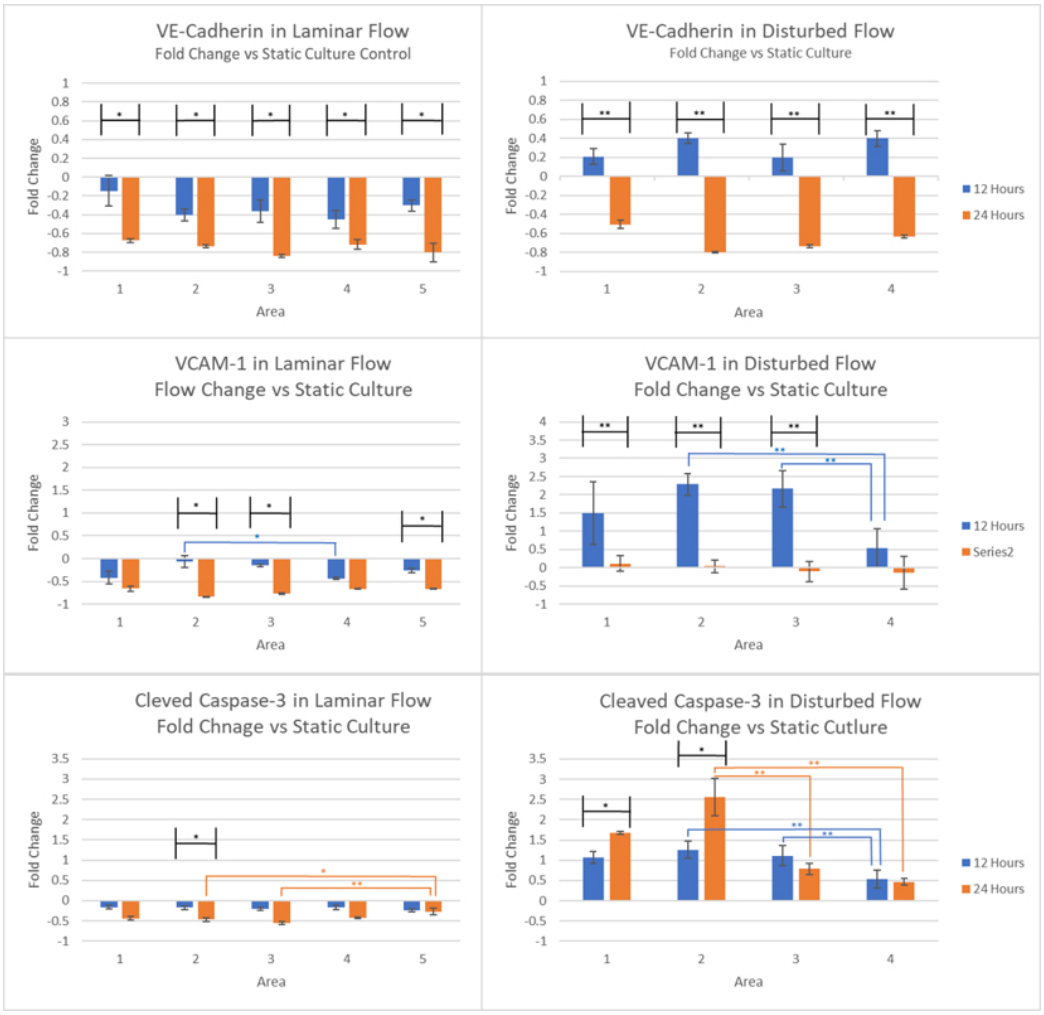

Figure 6.10: Effects of laminar and disturbed upon VE-cadherin, VCAM-1, and cleaved caspase-3 synthesis in HUVEC. Confluent monolayers of HUVECs were exposed for flow for 12 or 24 hrs and estimated protein concentrations were assessed by ELISA kits. Changes were expressed as fold change in relation to the static flow control slides used for the 12 hour experiments: * indicates $p \leq 0.05$ (One-way ANOVA with Tukey posthoc analysis).

average reduction. Differences were also seen in cellular VE-cadherin expression after 12 hours of disturbed flow exposure: a slight (0.09 ± 0.04) average fold increase followed by a marked reduction in its expression post-24 hour flow (0.67 ± 0.13 average fold decrease). The correlation to this degree of change in relation to vortex stability showed a negative trend, with higher stability relating to a greater decrease

in VE-cadherin after 24 hours of disturbed flow exposure, though this trend did not generate statistical significance: -0.848 correlation coefficient,p-value = 0.355.

Under pathological conditions, ECs show marked expression of surface molecules which mediate the adhesion of inflammatory molecules such as lymphocyte, monocyte, eosinophil and basophil adhesion [22, 69]. Heightened inflammatory protein accumulation in the artery can lead to the degradation of the mechanical strength of the vessel wall via increased protease expression which disrupts the internal elastic lamina and collagen matrix of the arterial wall and promotes vSMC proliferation from the media layer into the arterial neointima (thickened layer of arterial intima) [114]. Post-laminar flow exposure, HUVECs showed a reduction of the inflammatory adhesion molecule VCAM-1 in relation to cells in static culture, with a greater reduction as a function of time: 0.266±0.16 and 0.72±0.08 average fold decrease for 12 and 24 hours respectively. Hemodynamic vortices, deemed atheropromotive [68], showed significant increases in VCAM-1 expression after 12 hours of flow: 1.63±0.8 average fold increase. A slight positive trend for the degree of VCAM-1 in relation to flow stability was seen after 12 hours of disturbed flow exposure. Yet due to only slight reductions occurring between Area 2 and 3, no statistical significance was noted: 0.64 correlation coefficient, p-value = 0.558. A reduction in VCAM-1 expression was seen in disturbed flow post-24 flow exposure. While an averaged 0.06±0.09 fold decrease of VCAM-1 in relation to static culture controls was seen in the disturbed flow after 24 hours of disturbed flow exposure, a degree of VCAM-1 change was noted as a

function of vortex stability. Area 2 with a TA-DVO of 0.76 showed slight increases in VCAM-1 (0.04±0.17 fold increase) as opposed to the lower vortex stability of Areas 3 and 4 which showed reductions in VCAM-1 (0.1±0.27 and 0.14±0.45 fold decrease respectively). These changes to VCAM-1 expression after 24 hours of disturbed flow exposure showed a positive trend in relation to vortex stability: 0.99 correlation coefficient, p-value = 0.06.

Vascular cells exposed to pathological hemodynamic conditions for prolonged periods of time exhibit a breakdown of cellular functionality [142]. Disturbed flow induces endoplasmic reticulum stress which alters the proper folding of cellular proteins, with the accumulation of misfolded proteins triggering the release of apoptotic signals such as cleaved caspase-3 [181]. For HUVECs undergoing physiologic laminar flow for 12 hours, a slight reduction in cleaved caspase-3 expression was found in relation to static control cells: 0.19±0.03 average fold reduction. The continuation of laminar flow conditions (24 hours) showed further reductions in the expression of this apoptotic signaling protein, though these changes were not found to be statistically significant: 0.43±0.1 fold decrease in relation to 12 hour static control. When exposed to disturbed flow, a marked increased in the expression of cleaved caspase-3 was noted. After 12 hours disturbed flow exposure, a 0.72±0.32 averaged fold increase of cleaved caspase-3 occurred, with a larger 1.27±1.13 averaged fold increase after 24 hours of flow. Assessing the correlation of changes to this apoptotic signal to vortex

stability noted a positive trend after 12 hours of flow though this trend was not statistically significant: correlation coefficients of 0.74 (p-value = 0.47). Thought after 24 hours of flow exposure, this trend became more prominent and was shown to be statistically significant: correlation coefficients of 0.99 (p-value $<$0.05) for 12 and 24 hours respectively. Yet closer inspection of cleaved caspase-3 expression versus vortex stability showed that after 24 hour disturbed flow exposure Area 2 showed a marked increase over their 12 hour counterpart (1.27±0.21 vs 2.56±0.46, 12 vs 24 hours), whereas Area 3 and 4 had slight reductions after 24 hours compared with their 12 hour counterparts (1.1±0.25 vs 0.78±0.13 for Area 3 and 0.53±0.23 vs 0.47±0.08 for Area 4, 12 vs 24 hours).

While data from Area 1 of the disturbed flow chamber was not taken into account for statistical comparison with the other areas, similar trends in the expression of VCAM-1 and cleaved caspase-3 were seen between 12 and 24 hours as to what occurred in Area 2 of disturbed flow. The expression of VCAM-1 in Area 1 after 24 hours of disturbed flow exposure, while still showing marked reductions in relation to its 12 hour counterpart, maintained an overall increase in relation to the 12 hour static control: 1.5±1.06 vs 0.12±0.21 for 12 and 24 hours respectively. Additionally, an increase in cleaved caspase-3 was seen in Area 1 from 12 to 24 hours akin to what occurred in Area 2, while this trend was not seen in Areas 3 and 4 which had reduction in cleaved caspase-3 from 12 to 24 hours. It is theorized that these differences in outcomes (Areas 1 and 2 vs Areas 3 and 4) may be driven their differences in vortex

Protein: Exposure Time	Correlation Coefficient	p-value
VE-cadherin: 12 Hours	0.412	0.729
VE-cadherin: 24 Hours	-0.848	0.355
VCAM-1: 12 Hours	0.642	0.558
VCAM-1: 24 Hours	0.994	0.0610
Cas-3: 12 Hours	0.739	0.470
Cas-3: 24 Hours	0.999	**0.0213**

Table 6.3
(Pearson's) correlation coefficient of protein concentration in cells exposed to disturbed flow (only Areas 2-4) versus the stability of impacting vortices.

stability. Area 1 and 2 were noted as having a higher degree of vortex stability, 0.74 and 0.76 respectively, versus the lower stability of Areas 3 and 4 at 0.62 and 0.60. Indicating that a higher degree of vortex stability may exacerbate the expression of inflammatory markers and apoptotic signaling, and prolong their heightened expression over less stable vortices. Further analysis of alterations to HUVECs in bifurcated vortices of varied stability would need be performed to assess if this trend persists in such flow patterns.

6.3 Discussion

Swirling hemodynamic flow vortices are associated with degraded vascular physiology via increased inflammation, reduced regulation of macromolecule permeability, and weakened vessel mechanical strength, conditions indicative of the development and rupture of IAs. As the endothelial monolayer is tasked with the regulation of macromolecule permeability and triggering cellular signalling cascades in relation to hemodynamic conditions, alterations to these cells are often studied in

their relation to their role in IA pathology. While studies have highlighted the detrimental impact that flow vortices have on EC health, knowledge concerning the spatial and temporal characteristics of such patterns and how they may alter the degree of EC change is often overlooked. In reference to my work in Chapter 5, the assessment of vortex characteristics improved the differentiation of unrutpured and ruptured IAs, yet gave no insight into the specific underlying cellular/arterial changes which result from such characteristics. Therefore, as a means to broaden the understanding of IA pathology, alterations to ECs under vortices of varying conditions was studied. This work evaluated the impact that flow vortex stability has on HUVEC changes, primarily the expression of VE-cadherin, VCAM-1 and cleaved caspase-3. While the laminar flow conditions applied to HUVECs in this study resulted in their alignment with flow directionality, a decrease in the expression of VE-cadherin was seen when compared with cells in static culture. Even when accounting for cell count/possible cellular loss, this reduction became more pronounced with longer flow exposure (24 hours). When exposed to disturbed flow patterns for 12 hours, HUVEC cells slowed slight increases to VE-cadherin expression compared to static controls, yet prolonged exposure to detrimental flow conditions caused a significant (p=0.002) decrease in expression even after accounting for estimated cellular loss/detachment. Additionally, a trend was seen in the degree of this degradation in relation to vortex stability, with more stable vortices leading to a larger reduction in this protein after 24 hours though such differences were not statistically significant. It is worth noting,

that regardless of flow conditions, the dampening of VE-cadherin between 12 and 24 hours may be due to a time-delayed response via a needed down-regulation of cell-cell adhesion to allow for cellular elongation and reorientation to flow conditions. In a a study by Rami et al. VE-cadherin fluorescent intensity was shown to down-regulate in the initial exposure to flow and can take upwards of 48 hours post-flow exposure to be of a greater value than static control counterparts [273]. Experimentation with longer flow exposure would help to bolster trends (concerning VE-cadherin) seen in this work.

As inflammation is known to play a significant role in IA formation, assessing the impact flow characteristics have on the expression of inflammatory adhesion molecules can improve the understanding of IA pathology. When exposed to laminar flow at 7.5 dynes/cm^2, HUVECs showed a reduction in the inflammatory adhesion molecule VCAM-1, a molecule known to be elevated in aneurysmal tissue [104, 294]. Prolonged exposure to laminar flow conditions, from 12 to 24 hours, showed a statistically significant reduction in VCAM-1 (p=0.013). Such reductions were expected due to the atheroprotective nature of laminar flow concerning vascular cells [33]. The assessment of VCAM-1 in relation to disturbed flow conditions after 12 hours showed a significant increase when compared to cells in both static culture and laminar flow. In addition, a trend was seen when comparing VCAM-1 and the level of vortex stability when comparing areas 2, 3, and 4 of the disturbed chamber. Increased vortex stability coincided with a higher expression of this inflammatory adhesion molecule

after 12 hours of flow exposure, indicating that a more stable/stagnant flow vortex exacerbates inflammatory conditions though this trend was not found to be statistically significant and requires additional experimentation for confirmation. In terms of prolonged exposure to vortical flow, a significant reduction in VCAM-1 expression overall was noted after 24 hours compared to 12 hours. The degree of this reduction was seen to relate to vortex stability, with the greatest degree of VCAM-1 depression seen in Areas 3 and 4 of lower vortex stability, even showing a slight fold-decrease in expression than cells in the 12 hour static culture control. Meanwhile, cells exposed to vortices of higher stability in Area 2 for 24 hours, while still having reduced VCAM-1 expression in relation to their 12 hour counterparts, had a greater degree of expression than those in lower vortex stability (Areas 3 and 4). While reductions in inflammatory markers have been shown to reduce as a function of time after a degree of cellular damage [201], data from this study suggests that highly stable vortices may prolong the expression of this protein, whereas less stable vortices may have a reduced period of heightened VCAM-1 expression. Continued study with both additional flow experiments and longer time points may help bolster seen trends of inflammatory adhesion protein expression in relation to vortex stability.

The breakdown of EC functionality as a result of disturbed hemodynamic flow patterns is known to trigger cellular apoptosis [158, 160], which is elevated in areas of vessel remodeling [100, 216, 391] and IAs [127, 160]. Excessive cellular apoptosis exacerbates the aforementioned changes indicative of IA development and possible

rupture: alterations in macromolecule permeability due to degraded EC monolayer, increased infiltration of inflammatory proteins into the vessel media, and a breakdown of the mechanical characteristics of the vessel wall. Having a better understanding of the degree of cellular death in relation to hemodyanmic conditions within the aneurysmal sac could help improve clinical assessment of IA rupture risk. Similar to the atheroprotective nature of laminar flow, the apoptotic signal cleaved caspase-3 was shown to be down-regulated for HUVECs in relation to static culture control. Prolonged exposure to laminar flow (24 hours), showed further reduction of this apototic signal in relation to 12 hour static control cells. Similar to VCAM-1 expression in disturbed flow, cleaved caspase-3 showed a marked increased in relation to static cultured control. When exposed disturbed flow for 12 hours, a statistically significant difference was seen between Area 2 and 4, and Areas 3 and 4. In these areas, greater vortex stability was related to elevated cleaved caspase-3, though the differences between Area 2 and 3 was not found to be statistically significant. It is worth noting that while cleaved caspase-3 was still found to be elevated in areas of disturbed flow after 24 hours in relation to HUVECs in static control, expressions in Areas 3 and 4 were lower than their 12 hour counterparts, while Area 2 showed a marked increase. As previously noted, the flow vortex in Area 2 had the highest level of stability within the flow chamber (0.76), whereas Areas 3 and 4 we markedly lower at 0.62 and 0.60 respectively. Such a difference in outcomes indicate that a stability 'threshold' may

exist which leads to exacerbated cleaved caspase-3 production over a longer time period. While cells analyzed from Area 1 are excluded from comparisons to Areas 2, 3, and 4 due to the differing nature of its flow conditions, a similar pattern of cleaved caspase-3 increase between 12 and 24 hours was seen in this area (with a TA-DVO value of 0.72). This similar trend of increased cleaved caspase-3 in Area 1 and 2 bolster this theory that heightened vortex stability may trigger increased expression of this apoptotic signal over a longer period of time then less stable vortices.

6.4 Conclusion

Recent studies into hemodynamic conditions and their impact on IA development and rupture indicate that disturbed blood flow creates a proatherogenic in the cerebral arterial system: degraded vascular permeability by down-regulation of cell-cell adhesion molecules, and increased expression of inflammatory adhesion markers. Significant alterations to arterial cells can induce cellular apoptosis, triggering further breakdown of cellular/arterial functionality, degrading the overall mechanical strength of the arterial wall. In the realm of computational simulation alongside PPFCs, based on literature analyzed, this is the first study attempt to quantify the spatial and temporal stability of vortices within a modified PPFC and relate these levels to differing levels cellular changes. The initial data provided from this work showes that vortices of greater spatial and temporal stability may worsen alterations to ECs than more unstable flow patterns. While this work is still in its early stages,

it signifies the importance of continued analysis of complex flow patterns of varied characteristics to further understand the impact that hemodyanamic conditions have on IA development and possible rupture. While this work indicates that heightened vortex stability is linked with heightened levels of pathologic cellular changes, continued application these methods should be applied to assessing changes to a broader range of cellular proteins, and further modified PPFCs capable of creating differing vortex characteristics should be utilized to further understand cellular alterations in disturbed flow.

6.5 Acknowledgements

Kevin Sunderland was supported during this project in part by a American Heart Predoctoral Fellowship (18PRE33990321), and by a Finishing Fellowship from the Michigan Technological University for his final semester.

Chapter 7

Conclusion and Future Work

7.1 Conclusion

Assessment of the hemodynamic environment has shown to be beneficial in identifying conditions that promote the development and potential rupture of IAs. Yet a significant portion of this research focuses solely on the near-wall shear stressors (WSS) within arteries or a developed IA, overlooking bulk flow patterns and how their characteristics may impact this arterial pathology. The foci of this dissertation were to (1) develop a novel method for the identification of swirling flow patterns (vortices) within the bulk arterial flow, (2) determine if quantifying and analyzing the spatial and temporal characteristics of vortices can be utilized to improve the understanding of IAs and (3) unravel the mechanistic links between swirling flow patterns and changes observed in the endothelium. In the first aim of this work (Chapter 2) a

method to both identify vortices and quantify their spatial and temporal characteristics (i.e: size and stability) was developed using aspects of informational entropy. This Combined Entropy method was found be to be better suited for the study of vortices within the bulk flow of IAs than methods solely reliant on only identifying the center-most critical point of vortex patterns. The CE method was more robust against varying data quality (resolution), as well as identifying a broader area of the vortical pattern(s) as opposed to vortices identified using critical point methods. Utilizing this developed method, the second Aim (Chapter 3) of this dissertation showed that the addition of quantified vortex characteristics alongside the assessment of near-wall WSS improved the strength of statistical predictive models to determine areas of IA development. The third Aim (Chapter 4) of this dissertation, showed that the surgical repair of one IA may elicit significant hemodynamic alterations onto remaining IAs in a closely-spaced, multiple IA system. In particular, alterations to hemodynamic vortex stability were identified using the developed CE method, with such changes being otherwise overlooked without the proper assessment of bulk-flow vortices. Clinicians may weigh such alterations in flow conditions in relation to the risks they pose to patient health when deciding patient treatment options. The fourth Aim of this work (Chapter 5) found that relying on both IA/arterial geometric characteristics and WSS metrics have significant limitations when attempting to differentiate ruptured from unruptured IAs. Incorporating the spatial and temporal characteristics of flow vortices within the IA sac alongside (often used) IA geometric and WSS metrics

improved the accuracy of predictive models, giving new insight into the conditions that may impact IA rupture. In the final aim of this work, Chapter 6, vortices of varied characteristics were introduced onto cultured vascular cells utilizing a modified parallel plate flow chamber capable of creating distinct areas of swirling flow. This work found that vortices of increased spatial and temporal stability tended to trigger worsening alterations to cells versus cells exposed to more unstable vortices: increased expression of the inflammatory adhesion protein VCAM-1, and the apoptosis signal cleaved caspase-3 in stable vortices versus their unstable counterparts. Such findings help understand the alterations to the cellular environment that occur due to vortices of varied characteristics and how such vortices may play a role in IA pathology.

7.2 Future work

Collectively, my dissertation research has shown that the identification of hemodynamic vortices and quantification of their spatial and temporal characteristics improve the understanding of conditions indicative of intracranial aneurysm pathology. However, the body of work presented here is not meant as the culmination of this topic. The majority of the work conducted gives credence to the needed continued assessment of the vortical flow characteristics in this arterial pathology.

Of primary interest for future work is the application of the developed method of vortex identification/quantification onto a broader range of aneurysm types and locales. In this current work, analysis of hemodynamic patters was limited to the vessels

and/or aneurysms of either the internal carotid artery as in Chapters 2, 3, and 4 or middle cerebral artery as in Chapter 5. In addition to extending the techniques developed into other areas of the human body, further improvements need to be performed via the assessment of clinically measured flow data. A significant degree of analysis in this work, while performed on patient-specific vascular structures, flow data itself was generated utilizing generalized human flow waveforms. While it is possible to gain insight into the impact of flow characteristics on IAs using such data, reliance on generalized waveforms may cause a restrictive view of vortex characteristics within the vasculature. Especially in the case of Chapter 5, patient flow characteristics can vary based on health factors (e.g. heart rates), and these changes could alter flow conditions indicative of aneurysm rupture. Future application of the developed vortex analysis technique onto clinically-derived patient flow data should be seen as a high priority to better understand the specific conditions that led to a patient's aneurysm development/rupture.

Additionally, while findings in Chapter 6 showed vortices of varying stability impart differing levels of cellular changes (to cultured HUVECs), this was only analyzed for a limited number of proteins and for only two chosen time points. A broad array of cellular proteins are thought to play a role in the development and possible rupture of IAs, stressing the need to further expand upon work of this nature. Also, future variations to PPFC chamber (and baffle) design should be explored as to generate differing vortex characteristics onto cultured cells, giving further insight into how

vortex patterns impact IA pathology.

References

[1] Abboud, T., Rustom, J., Bester, M., Czorlich, P., Vittorazzi, E., Pinnschmidt, H. O., Westphal, M., and Regelsberger, J. Morphology of ruptured and unruptured intracranial aneurysms. *World neurosurgery 99* (2017), 610–617.

[2] Adib, M. A. H. M., Ii, S., Watanabe, Y., and Wada, S. Minimizing the blood velocity differences between phase-contrast magnetic resonance imaging and computational fluid dynamics simulation in cerebral arteries and aneurysms. *Medical & biological engineering & computing 55*, 9 (2017), 1605–1619.

[3] Ahmed, S., and Warren, D. T. Vascular smooth muscle cell contractile function and mechanotransduction. *Vessel Plus 2*, 11 (2018).

[4] Aird, W. Spatial and temporal dynamics of the endothelium. *Journal of Thrombosis and Haemostasis 3*, 7 (2005), 1392–1406.

[5] Al-Soudi, A., Kaaij, M., and Tas, S. Endothelial cells: From innocent

bystanders to active participants in immune responses. *Autoimmunity Reviews 16*, 9 (2017), 951 – 962.

[6] Alfano, J. M., Kolega, J., Natarajan, S. K., Xiang, J., Paluch, R. A., Levy, E. I., Siddiqui, A. H., and Meng, H. Intracranial aneurysms occur more frequently at bifurcation sites that typically experience higher hemodynamic stresses. *Neurosurgery 73*, 3 (2013), 497–505.

[7] Alimohammadi, M., Sherwood, J. M., Karimpour, M., Agu, O., Balabani, S., and Díaz-Zuccarini, V. Aortic dissection simulation models for clinical support: fluid-structure interaction vs. rigid wall models. *Biomedical engineering online 14*, 1 (2015), 1–16.

[8] Alnæs, M. S., Isaksen, J., Mardal, K.-A., Romner, B., Morgan, M. K., and Ingebrigtsen, T. Computation of hemodynamics in the circle of willis. *Stroke 38*, 9 (2007), 2500–2505.

[9] Amenta, P. S., Valle, E., Dumont, A. S., Medel, R., et al. Inflammation and intracranial aneurysms: mechanisms of initiation, growth, and rupture. *Neuroimmunology and Neuroinflammation 2*, 2 (2015), 68.

[10] Antiga, L., and Steinman, D. A. Robust and objective decomposition and mapping of bifurcating vessels. *IEEE transactions on medical imaging 23*, 6 (2004), 704–713.

[11] Aoki, T., Kataoka, H., Morimoto, M., Nozaki, K., and Hashimoto, N. Macrophage-derived matrix metalloproteinase-2 and -9 promote the progression of cerebral aneurysms in rats. *Stroke 38* (2007), 162–169.

[12] Aoki, T., Yamamoto, K., Fukuda, M., Shimogonya, Y., Fukuda, S., and Narumiya, S. Sustained expression of mcp-1 by low wall shear stress loading concomitant with turbulent flow on endothelial cells of intracranial aneurysm. *Acta Neuropathologica Communications 4*, 1 (2016), 48.

[13] Ashina, K., Tsubosaka, Y., Nakamura, T., Omori, K., Kobayashi, K., Hori, M., Ozaki, H., and Murata, T. Histamine induces vascular hyperpermeability by increasing blood flow and endothelial barrier disruption in vivo. *Plos one 10*, 7 (2015).

[14] Augst, A., Ariff, B., McG. Thom, S., Xu, X., and Hughes, A. D. Analysis of complex flow and the relationship between blood pressure, wall shear stress, and intima-media thickness in the human carotid artery. *American Journal of Physiology-heart and circulatory physiology 293*, 2 (2007), H1031–H1037.

[15] Backes, D., Rinkel, G. J., Laban, K. G., Algra, A., and Vergouwen, M. D. Patient- and aneurysm-specific risk factors for intracranial aneurysm growth. *Stroke 47*, 4 (2016), 951–957.

[16] Backes, D., Rinkel, G. J., Laban, K. G., Algra, A., and Vergouwen, M. D. Patient- and aneurysm-specific risk factors for intracranial aneurysm growth. *Stroke 47*, 4 (2016), 951–957.

[17] Backes, D., Vergouwen, M. D., Tiel Groenestege, A. T., Bor, A. S. E., Velthuis, B. K., Greving, J. P., Algra, A., Wermer, M. J., van Walderveen, M. A., terBrugge, K. G., et al. Phases score for prediction of intracranial aneurysm growth. *Stroke 46*, 5 (2015), 1221–1226.

[18] Backes, D., Vergouwen, M. D., Velthuis, B. K., van der Schaaf, I. C., Bor, A. S. E., Algra, A., and Rinkel, G. J. Difference in aneurysm characteristics between ruptured and unruptured aneurysms in patients with multiple intracranial aneurysms. *Stroke 45*, 5 (2014), 1299–1303.

[19] Baek, H., Jayaraman, M., Richardson, P., and Karniadakis, G. Flow instability and wall shear stress variation in intracranial aneurysms. *Journal of the Royal Society Interface* (2009), rsif20090476.

[20] Baeriswyl, D. C., Prionisti, I., Peach, T., Tsolkas, G., Chooi, K. Y., Vardakis, J., Morel, S., Diagbouga, M. R., Bijlenga, P., Cuhlmann, S., et al. Disturbed flow induces a sustained, stochastic nf-κb activation which may support intracranial aneurysm growth in vivo. *Scientific reports 9*, 1 (2019), 1–14.

[21] Baeyens, N., Bandyopadhyay, C., Coon, B. G., Yun, S., and Schwartz, M. A. Endothelial fluid shear stress sensing in vascular health and disease. *The Journal of clinical investigation 126*, 3 (2016), 821–828.

[22] Bailey, K. A., Moreno, E., Haj, F. G., Simon, S. I., and Passerini, A. G. Mechanoregulation of p38 activity enhances endoplasmic reticulum stress–mediated inflammation by arterial endothelium. *The FASEB Journal 33*, 11 (2019), 12888–12899.

[23] Balaguru, U. M., Sundaresan, L., Manivannan, J., Majunathan, R., Mani, K., Swaminathan, A., Venkatesan, S., Kasiviswanathan, D., and Chatterjee, S. Disturbed flow mediated modulation of shear forces on endothelial plane: A proposed model for studying endothelium around atherosclerotic plaques. *Scientific reports 6* (2016), 27304.

[24] Baratchi, S., Khoshmanesh, K., Woodman, O. L., Potocnik, S., Peter, K., and McIntyre, P. Molecular sensors of blood flow in endothelial cells. *Trends in molecular medicine 23*, 9 (2017), 850–868.

[25] Baráth, K., Cassot, F., Rüfenacht, D. A., and Fasel, J. H. Anatomically shaped internal carotid artery aneurysm in vitro model for flow analysis to evaluate stent effect. *American Journal of Neuroradiology 25*, 10 (2004), 1750–1759.

[26] Barry, A. K., Wang, N., and Leckband, D. E. Local ve-cadherin mechanotransduction triggers long-ranged remodeling of endothelial monolayers. *J Cell Sci 128*, 7 (2015), 1341–1351.

[27] Bazilevs, Y., Hsu, M.-C., Zhang, Y., Wang, W., Kvamsdal, T., Hentschel, S., and Isaksen, J. Computational vascular fluid–structure interaction: methodology and application to cerebral aneurysms. *Biomechanics and modeling in mechanobiology 9*, 4 (2010), 481–498.

[28] Becker, B. F., Jacob, M., Leipert, S., Salmon, A. H., and Chappell, D. Degradation of the endothelial glycocalyx in clinical settings: searching for the sheddases. *British journal of clinical pharmacology 80*, 3 (2015), 389–402.

[29] Bekelis, K., Missios, S., MacKenzie, T. A., Labropoulos, N., and Roberts, D. W. A predictive model of hospitalization cost after cerebral aneurysm clipping. *Journal of NeuroInterventional Surgery 8*, 3 (2016), 316–322.

[30] Bell, J. D., Rhind, S. G., Di Battista, A. P., Macdonald, R. L., and Baker, A. J. Biomarkers of glycocalyx injury are associated with delayed cerebral ischemia following aneurysmal subarachnoid hemorrhage: a case series supporting a new hypothesis. *Neurocritical care 26*, 3 (2017), 339–347.

[31] Benn, A., Bredow, C., Casanova, I., Vukičević, S., and Knaus, P. Ve-cadherin facilitates bmp-induced endothelial cell permeability and signaling. *Journal of cell science 129*, 1 (2016), 206–218.

[32] Benndorf, G., Wellnhofer, E., Lanksch, W., and Felix, R. Intraaneurysmal flow: evaluation with doppler guidewires. *American journal of neuroradiology 17*, 7 (1996), 1333–1337.

[33] Berk, B. C. Atheroprotective signaling mechanisms activated by steady laminar flow in endothelial cells. *Circulation 117*, 8 (2008), 1082–1089.

[34] Biasetti, J., Hussain, F., and Gasser, T. C. Blood flow and coherent vortices in the normal and aneurysmatic aortas: a fluid dynamical approach to intra-luminal thrombus formation. *Journal of The Royal Society Interface* (2011), rsif20110041.

[35] Bibli, S.-I., Hu, J., Leisegang, M. S., Wittig, J., Zukunft, S., Kapasakalidi, A., Fisslthaler, B., Tsilimigras, D., Zografos, G., Filis, K., et al. Shear stress regulates cystathionine γ lyase expression to preserve endothelial redox balance and reduce membrane lipid peroxidation. *Redox biology 28* (2020), 101379.

[36] Bijlenga, P., Gondar, R., Schilling, S., Morel, S., Hirsch, S., Cuony, J., Corniola, M.-V., Perren, F., Rüfenacht, D., and Schaller, K. Phases score for the management of intracranial aneurysm:

a cross-sectional population-based retrospective study. *Stroke 48*, 8 (2017), 2105–2112.

[37] Bogunovic, N., Meekel, J. P., Micha, D., Blankensteijn, J. D., Hordijk, P. L., and Yeung, K. K. Impaired smooth muscle cell contractility as a novel concept of abdominal aortic aneurysm pathophysiology. *Scientific reports 9*, 1 (2019), 1–14.

[38] Boussel, L., Rayz, V., McCulloch, C., Martin, A., Acevedo-Bolton, G., Lawton, M., Higashida, R., Smith, W. S., Young, W. L., and Saloner, D. Aneurysm growth occurs at region of low wall shear stress: patient-specific correlation of hemodynamics and growth in a longitudinal study. *Stroke 39*, 11 (2008), 2997–3002.

[39] Brinjikji, W., Kallmes, D. F., Lanzino, G., and Cloft, H. Hospitalization costs for endovascular and surgical treatment of unruptured cerebral aneurysms in the united states are substantially higher than medicare payments. *American Journal of Neuroradiology 33*, 1 (2012), 49–51.

[40] Brinjikji, W., Zhu, Y.-Q., Lanzino, G., Cloft, H., Murad, M., Wang, Z., and Kallmes, D. Risk factors for growth of intracranial aneurysms: A systematic review and meta-analysis. *American Journal of Neuroradiology* (2015).

[41] Brisman, J. L., Song, J. K., and Newell, D. W. Cerebral aneurysms. *New England journal of medicine 355*, 9 (2006), 928–939.

[42] Byrne, G., and Cebral, J. Vortex dynamics in cerebral aneurysms. *arXiv preprint arXiv:1309.7875* (2013).

[43] Byrne, G., Mut, F., and Cebral, J. Quantifying the large-scale hemodynamics of intracranial aneurysms. *American Journal of Neuroradiology 35*, 2 (2014), 333–338.

[44] Cahill, P. A., and Redmond, E. M. Vascular endothelium–gatekeeper of vessel health. *Atherosclerosis 248* (2016), 97–109.

[45] Can, A., and Du, R. Association of hemodynamic factors with intracranial aneurysm formation and rupture: systematic review and meta-analysis. *Neurosurgery 78*, 4 (2015), 510–520.

[46] Cancel, L. M., Ebong, E. E., Mensah, S., Hirschberg, C., and Tarbell, J. M. Endothelial glycocalyx, apoptosis and inflammation in an atherosclerotic mouse model. *Atherosclerosis 252* (2016), 136–146.

[47] Caolo, V., Peacock, H. M., Kasaai, B., Swennen, G., Gordon, E., Claesson-Welsh, L., Post, M. J., Verhamme, P., and Jones, E. A. Shear stress and ve-cadherin: the molecular mechanism of vascular fusion. *Arteriosclerosis, thrombosis, and vascular biology 38*, 9 (2018), 2174–2183.

[48] Castro, M. A., Olivares, M. C. A., Putman, C. M., and Cebral, J. R. Wall motion and hemodynamics in intracranial aneurysms. In *Journal of Physics: Conference Series* (2013), vol. 477, IOP Publishing, p. 012004.

[49] Cebral, J., Detmer, F., Chung, B., Choque-Velasquez, J., Rezai, B., Lehto, H., Tulamo, R., Hernesniemi, J., Niemela, M., Yu, A., Williamson, R., Aziz, K., Sakur, S., Amin-Hanjani, S., Charbel, F., Tobe, Y., Robertson, A., and Frösen, J. Local hemodynamic conditions associated with focal changes in the intracranial aneurysm wall. *American Journal of Neuroradiology 40*, 3 (2019), 510–516.

[50] Cebral, J., Ollikainen, E., Chung, B. J., Mut, F., Sippola, V., Jahromi, B. R., Tulamo, R., Hernesniemi, J., Niemelä, M., Robertson, A., and Frösen, J. Flow conditions in the intracranial aneurysm lumen are associated with inflammation and degenerative changes of the aneurysm wall. *American Journal of Neuroradiology 38*, 1 (2017), 119–126.

[51] Cebral, J. R., Mut, F., Weir, J., and Putman, C. M. Association of hemodynamic characteristics and cerebral aneurysm rupture. *American Journal of Neuroradiology 32*, 2 (2011), 264–270.

[52] Cecchi, E., Giglioli, C., Valente, S., Lazzeri, C., Gensini, G. F., Abbate, R., and Mannini, L. Role of hemodynamic shear stress in cardiovascular disease. *Atherosclerosis 214*, 2 (2011), 249–256.

[53] Cha, S.-H., Hwang, Y., Kim, K.-N., and Jun, H.-S. Palmitate induces nitric oxide production and inflammatory cytokine expression in zebrafish. *Fish & shellfish immunology 79* (2018), 163–167.

[54] Chalouhi, N., Ali, M. S., Jabbour, P. M., Tjoumakaris, S. I., Gonzalez, L. F., Rosenwasser, R. H., Koch, W. J., and Dumont, A. S. Biology of intracranial aneurysms: role of inflammation. *Journal of Cerebral Blood Flow & Metabolism 32*, 9 (2012), 1659–1676.

[55] Chalouhi, N., Hoh, B. L., and Hasan, D. Review of cerebral aneurysm formation, growth, and rupture. *Stroke 44*, 12 (2013), 3613–3622.

[56] Chalouhi, N., Zanaty, M., Whiting, A., Yang, S., Tjoumakaris, S., Hasan, D., Starke, R. M., Hann, S., Hammer, C., Kung, D., and et. al. Safety and efficacy of the pipeline embolization device in 100 small intracranial aneurysms. *Journal of neurosurgery 122*, 6 (2015), 1498–1502.

[57] Chatterjee, S. Endothelial mechanotransduction, redox signaling and the regulation of vascular inflammatory pathways. *Frontiers in physiology 9* (2018), 524.

[58] Chattopadhyay, R., Dyukova, E., Singh, N. K., Ohba, M., Mobley,

J. A., and Rao, G. N. Vascular endothelial tight junctions and barrier function are disrupted by 15 (s)-hydroxyeicosatetraenoic acid partly via protein kinase cϵ-mediated zona occludens-1 phosphorylation at threonine 770/772. *Journal of Biological Chemistry 289*, 6 (2014), 3148–3163.

[59] Chatzizisis, Y. S., Coskun, A. U., Jonas, M., Edelman, E. R., Feldman, C. L., and Stone, P. H. Role of endothelial shear stress in the natural history of coronary atherosclerosis and vascular remodeling: Molecular, cellular, and vascular behavior. *Journal of the American College of Cardiology 49*, 25 (2007), 2379 – 2393.

[60] Chen, C.-N., Chang, S.-F., Lee, P.-L., Chang, K., Chen, L.-J., Usami, S., Chien, S., and Chiu, J.-J. Neutrophils, lymphocytes, and monocytes exhibit diverse behaviors in transendothelial and subendothelial migrations under coculture with smooth muscle cells in disturbed flow. *Blood 107*, 5 (2006), 1933–1942.

[61] Chen, H., Selimovic, A., Thompson, H., Chiarini, A., Penrose, J., Ventikos, Y., and Watton, P. N. Investigating the influence of haemodynamic stimuli on intracranial aneurysm inception. *Annals of biomedical engineering 41*, 7 (2013), 1492–1504.

[62] Chen, J., Green, J., Yurdagul Jr, A., Albert, P., McInnis, M. C.,

and Orr, A. W. $\alpha v\beta 3$ integrins mediate flow-induced nf-κb activation, proinflammatory gene expression, and early atherogenic inflammation. *The American journal of pathology 185*, 9 (2015), 2575–2589.

[63] Chen, Z., and Tzima, E. Pecam-1 is necessary for flow-induced vascular remodeling. *Arteriosclerosis, thrombosis, and vascular biology 29*, 7 (2009), 1067–1073.

[64] Cheng, Z., Zhou, Y.-z., Wu, Y., Wu, Q.-y., Liao, X.-b., Fu, X.-m., and Zhou, X.-m. Diverse roles of macrophage polarization in aortic aneurysm: destruction and repair. *Journal of translational medicine 16*, 1 (2018), 354.

[65] Chien, S. Mechanotransduction and endothelial cell homeostasis: the wisdom of the cell. *American Journal of Physiology-Heart and Circulatory Physiology 292*, 3 (2007), H1209–H1224.

[66] Chistiakov, D. A., Melnichenko, A. A., Myasoedova, V. A., Grechko, A. V., and Orekhov, A. N. Mechanisms of foam cell formation in atherosclerosis. *Journal of Molecular Medicine 95*, 11 (2017), 1153–1165.

[67] Chistiakov, D. A., Orekhov, A. N., and Bobryshev, Y. V. Effects of shear stress on endothelial cells: go with the flow. *Acta physiologica 219*, 2 (2017), 382–408.

[68] Chiu, J.-J., and Chien, S. Effects of disturbed flow on vascular endothelium: pathophysiological basis and clinical perspectives. *Physiological reviews 91*, 1 (2011), 327–387.

[69] Chung, H., Ji, S. C., Lee, S., Yu, K.-S., Jang, I.-J., Cho, J.-Y., et al. Ursodeoxycholic acid exerts hepatoprotective effects by regulating amino acid, flavonoid, and fatty acid metabolic pathways. *Metabolomics 15*, 3 (2019), 30.

[70] Chung, J., Kim, K. H., Lee, S. C., An, S. H., and Kwon, K. Ursodeoxycholic acid (udca) exerts anti-atherogenic effects by inhibiting endoplasmic reticulum (er) stress induced by disturbed flow. *Molecules and cells 38*, 10 (2015), 851.

[71] Claesson-Welsh, L. Vascular permeability—the essentials. *Upsala journal of medical sciences 120*, 3 (2015), 135–143.

[72] Codelia, V. A., Sun, G., and Irvine, K. D. Regulation of yap by mechanical strain through jnk and hippo signaling. *Current biology 24*, 17 (2014), 2012–2017.

[73] Conway, D. E., and Schwartz, M. A. Mechanotransduction of shear stress occurs through changes in ve-cadherin and pecam-1 tension: implications for cell migration. *Cell adhesion & migration 9*, 5 (2015), 335–339.

[74] Cook-Mills, J. M., Marchese, M. E., and Abdala-Valencia, H. Vascular cell adhesion molecule-1 expression and signaling during disease: regulation

by reactive oxygen species and antioxidants. *Antioxidants & redox signaling 15*, 6 (2011), 1607–1638.

[75] Cooper, S., Emmott, A., McDonald, K. K., Campeau, M.-A., and Leask, R. L. Increased mmp activity in curved geometries disrupts the endothelial cell glycocalyx creating a proinflammatory environment. *PloS one 13*, 8 (2018).

[76] Cooper, S., McDonald, K., Burkat, D., and Leask, R. L. Stenosis hemodynamics disrupt the endothelial cell glycocalyx by mmp activity creating a proinflammatory environment. *Annals of biomedical engineering 45*, 9 (2017), 2234–2243.

[77] Cornelissen, B., Schneiders, J., Potters, W., van den Berg, R., Velthuis, B., Rinkel, G., Slump, C., VanBavel, E., Majoie, C., and Marquering, H. Hemodynamic differences in intracranial aneurysms before and after rupture. *American Journal of Neuroradiology 36*, 10 (2015), 1927–1933.

[78] Crompton, M. Mechanism of growth and rupture in cerebral berry aneurysms. *British medical journal 1*, 5496 (1966), 1138.

[79] Dale, M. A., Xiong, W., Carson, J. S., Suh, M. K., Karpisek, A. D., Meisinger, T. M., Casale, G. P., and Baxter, B. T. Elastin-derived peptides promote abdominal aortic aneurysm formation by modulating m1/m2

macrophage polarization. *The Journal of Immunology 196*, 11 (2016), 4536–4543.

[80] Darby, R., Darby, R., and Chhabra, R. P. *Chemical engineering fluid mechanics, revised and expanded*. CRC Press, 2017.

[81] Demartini, L. C., Vielmo, H. A., and Möller, S. Numeric and experimental analysis of the turbulent flow through a channel with baffle plates. *Journal of the Brazilian Society of Mechanical Sciences and Engineering 26*, 2 (2004), 153–159.

[82] Dempere-Marco, L., Oubel, E., Castro, M., Putman, C., Frangi, A., and Cebral, J. Cfd analysis incorporating the influence of wall motion: application to intracranial aneurysms. In *International Conference on Medical Image Computing and Computer-Assisted Intervention* (2006), Springer, pp. 438–445.

[83] Deplano, V., Knapp, Y., Bertrand, E., and Gaillard, E. Flow behaviour in an asymmetric compliant experimental model for abdominal aortic aneurysm. *Journal of biomechanics 40*, 11 (2007), 2406–2413.

[84] Detmer, F. J., Chung, B. J., Mut, F., Pritz, M., Slawski, M., Hamzei-Sichani, F., Kallmes, D., Putman, C., Jimenez, C., and Cebral, J. R. Development of a statistical model for discrimination of rupture status in posterior communicating artery aneurysms. *Acta neurochirurgica 160*, 8 (2018), 1643–1652.

[85] Detmer, F. J., Fajardo-Jiménez, D., Mut, F., Juchler, N., Hirsch, S., Pereira, V. M., Bijlenga, P., and Cebral, J. R. External validation of cerebral aneurysm rupture probability model with data from two patient cohorts. *Acta neurochirurgica 160*, 12 (2018), 2425–2434.

[86] Di Achille, P., Tellides, G., and Humphrey, J. Hemodynamics-driven deposition of intraluminal thrombus in abdominal aortic aneurysms. *International journal for numerical methods in biomedical engineering 33*, 5 (2017), e2828.

[87] Diagbouga, M. R., Morel, S., Bijlenga, P., and Kwak, B. R. Role of hemodynamics in initiation/growth of intracranial aneurysms. *European journal of clinical investigation 48*, 9 (2018), e12992.

[88] Doddasomayajula, R., Chung, B. J., Mut, F., Jimenez, C. M., Hamzei-Sichani, F., Putman, C. M., and Cebral, J. R. Hemodynamic characteristics of ruptured and unruptured multiple aneurysms at mirror and ipsilateral locations. *American Journal of Neuroradiology 38*, 12 (2017), 2301–2307.

[89] Dolan, J. M., Kolega, J., and Meng, H. High wall shear stress and spatial gradients in vascular pathology: a review. *Annals of biomedical engineering 41*, 7 (2013), 1411–1427.

[90] Dolan, J. M., Meng, H., Sim, F. J., and Kolega, J. Differential gene expression by endothelial cells under positive and negative streamwise gradients of high wall shear stress. *American Journal of Physiology-Cell Physiology 305*, 8 (2013), C854–C866.

[91] Dolan, J. M., Meng, H., Singh, S., Paluch, R., and Kolega, J. High fluid shear stress and spatial shear stress gradients affect endothelial proliferation, survival, and alignment. *Annals of biomedical engineering 39*, 6 (2011), 1620–1631.

[92] Dorland, Y. L., and Huveneers, S. Cell–cell junctional mechanotransduction in endothelial remodeling. *Cellular and Molecular Life Sciences 74*, 2 (2017), 279–292.

[93] Duan, Z., Li, Y., Guan, S., Ma, C., Han, Y., Ren, X., We, L., Li, W., Lo, J., and Yang, Z. Morphological parameters and anatomical locations associated with rupture status of small intracranial aneurysms. *Scientific reports 8* (2018).

[94] Duca, L., Blaise, S., Romier, B., Laffargue, M., Gayral, S., El Btaouri, H., Kawecki, C., Guillot, A., Martiny, L., Debelle, L., et al. Matrix ageing and vascular impacts: focus on elastin fragmentation. *Cardiovascular research 110*, 3 (2016), 298–308.

[95] Dunzendorfer, S., Lee, H.-K., and Tobias, P. S. Flow-dependent regulation of endothelial toll-like receptor 2 expression through inhibition of sp1 activity. *Circulation Research 95*, 7 (2004), 684–691.

[96] Efron, B., Hastie, T., Johnstone, I., Tibshirani, R., and et. al. Least angle regression. *The Annals of statistics 32*, 2 (2004), 407–499.

[97] Einav, S., and Bluestein, D. Dynamics of blood flow and platelet transport in pathological vessels. *Annals of the New York Academy of Sciences 1015*, 1 (2004), 351–366.

[98] Elad, D., and Einav, S. Physical and flow properties of blood. *Standard handbook of biomedical engineering and design* (2004), 3–1.

[99] Ellamushi, H. E., Grieve, J. P., Jäger, H. R., and Kitchen, N. D. Risk factors for the formation of multiple intracranial aneurysms. *Journal of neurosurgery 94*, 5 (2001), 728–732.

[100] Emrich, F. C., Okamura, H., Dalal, A. R., Penov, K., Merk, D. R., Raaz, U., Hennigs, J. K., Chin, J. T., Miller, M. O., Pedroza, A. J., et al. Enhanced caspase activity contributes to aortic wall remodeling and early aneurysm development in a murine model of marfan syndrome. *Arteriosclerosis, thrombosis, and vascular biology 35*, 1 (2015), 146–154.

[101] Enzmann, D. R., Ross, M. R., Marks, M. P., and Pelc, N. J. Blood flow in major cerebral arteries measured by phase-contrast cine mr. *American journal of neuroradiology 15*, 1 (1994), 123–129.

[102] Etminan, N., Brown, R. D., Beseoglu, K., Juvela, S., Raymond, J., Morita, A., Torner, J. C., Derdeyn, C. P., Raabe, A., Mocco, J., and et. al. The unruptured intracranial aneurysm treatment score a multidisciplinary consensus. *Neurology 85*, 10 (2015), 881–889.

[103] Familiari, P., Maldaner, N., Kursumovic, A., Rath, S., Vajkoczy, P., Raco, A., and Dengler, J. Cost comparison of surgical and endovascular treatment of unruptured giant intracranial aneurysms. *Neurosurgery 77*, 5 (2015), 733–743.

[104] Fan, J., Li, X., Zhong, L., Hao-Tong, Di, J., Liu, F., Zhao, H.-H., and Bai, S.-L. Mcp-1, icam-1 and vcam-1 are present in early aneurysmal dilatation in experimental rats. *Folia histochemica et cytobiologica - Polish Academy of Sciences, Polish Histochemical and Cytochemical Society 48* (11 2010), 455–61.

[105] Febina, J., Sikkandar, M. Y., and Sudharsan, N. Wall shear stress estimation of thoracic aortic aneurysm using computational fluid dynamics. *Computational and Mathematical Methods in Medicine 2018* (2018).

[106] Feliciani, G., Potters, W. V., van Ooij, P., Schneiders, J. J., Nederveen, A. J., van Bavel, E., Majoie, C. B., and Marquering, H. A.

Multiscale 3-d+ t intracranial aneurysmal flow vortex detection. *IEEE Trans. Biomed. Engineering 62*, 5 (2015), 1355–1362.

[107] Fennell, V. S., Kalani, M. Y. S., Atwal, G., Martirosyan, N. L., and Spetzler, R. F. Biology of saccular cerebral aneurysms: a review of current understanding and future directions. *Frontiers in surgery 3* (2016), 43.

[108] Ferns, S. P., Sprengers, M. E., van Rooij, W. J. J., van den Berg, R., Velthuis, B. K., de Kort, G. A., Sluzewski, M., van Zwam, W. H., Rinkel, G. J., and Majoie, C. B. De novo aneurysm formation and growth of untreated aneurysms. *Stroke 42*, 2 (2011), 313–318.

[109] Finch, H. A comparison of methods for group prediction with high dimensional data. *Journal of Modern Applied Statistical Methods 13*, 2 (2014), 5.

[110] Ford, M., Hoi, Y., Piccinelli, M., Antiga, L., and Steinman, D. An objective approach to digital removal of saccular aneurysms: technique and applications. *The British Journal of Radiology 82*, special_issue_1 (2009), S55–S61.

[111] Ford, M. D., Alperin, N., Lee, S. H., Holdsworth, D. W., and Steinman, D. A. Characterization of volumetric flow rate waveforms in the normal internal carotid and vertebral arteries. *Physiological measurement 26*, 4 (2005), 477.

[112] Ford, M. D., Nikolov, H. N., Milner, J. S., Lownie, S. P., DeMont, E. M., Kalata, W., Loth, F., Holdsworth, D. W., and Steinman, D. A. Piv-measured versus cfd-predicted flow dynamics in anatomically realistic cerebral aneurysm models. *Journal of biomechanical engineering 130*, 2 (2008), 021015.

[113] Förstermann, U., and Sessa, W. C. Nitric oxide synthases: regulation and function. *Eur Heart J 33*, 7 (2012), 829–37.

[114] Frösen, J., Cebral, J., Robertson, A. M., and Aoki, T. Flow-induced, inflammation-mediated arterial wall remodeling in the formation and progression of intracranial aneurysms. *Neurosurgical Focus FOC 47*, 1 (01 Jul. 2019), E21.

[115] Fukuda, S., Shimogonya, Y., and Yonemoto, N. Differences in cerebral aneurysm rupture rate according to arterial anatomies depend on the hemodynamic environment. *American Journal of Neuroradiology 40*, 5 (2019), 834–839.

[116] Fung, J. C. H. Residence time of inertial particles in a vortex. *Journal of Geophysical Research: Oceans 105*, C6 (2000), 14261–14272.

[117] Gabriel, S. A., Ding, Y., and Feng, Y. Quantifying the influence of oscillatory flow disturbances on blood flow. *Journal of Theoretical Biology 430* (2017), 195 – 206.

[118] Gallo, D., Steinman, D. A., and Morbiducci, U. An insight into the mechanistic role of the common carotid artery on the hemodynamics at the carotid bifurcation. *Annals of biomedical engineering 43*, 1 (2015), 68–81.

[119] Gambaruto, A., and João, A. Flow structures in cerebral aneurysms. *Computers and Fluids 65*, Supplement C (2012), 56 – 65. Sixth International Conference on Computational Fluid Dynamics (ICCFD6).

[120] Geers, A., Morales, H., Larrabide, I., Butakoff, C., Bijlenga, P., and Frangi, A. Wall shear stress at the initiation site of cerebral aneurysms. *Biomechanics and modeling in mechanobiology 16*, 1 (2017), 97–115.

[121] Ghim, M., Alpresa, P., Yang, S.-W., Braakman, S. T., Gray, S. G., Sherwin, S. J., van Reeuwijk, M., and Weinberg, P. D. Visualization of three pathways for macromolecule transport across cultured endothelium and their modification by flow. *American Journal of Physiology-Heart and Circulatory Physiology 313*, 5 (2017), H959–H973.

[122] Go, Y.-M., Son, D. J., Park, H., Orr, M., Hao, L., Takabe, W., Kumar, S., Kang, D. W., Kim, C. W., Jo, H., et al. Disturbed flow enhances inflammatory signaling and atherogenesis by increasing thioredoxin-1 level in endothelial cell nuclei. *PloS one 9*, 9 (2014).

[123] Gomez-Garcia, M. J., Doiron, A. L., Steele, R. R., Labouta, H. I., Vafadar, B., Shepherd, R. D., Gates, I. D., Cramb, D. T., Childs,

S. J., and Rinker, K. D. Nanoparticle localization in blood vessels: dependence on fluid shear stress, flow disturbances, and flow-induced changes in endothelial physiology. *Nanoscale 10*, 32 (2018), 15249–15261.

[124] Gourbesville, P., Cunge, J., and Caignaert, G. *Advances in Hydroinformatics: SIMHYDRO 2012–New Frontiers of Simulation*. Springer Science & Business Media, 2013.

[125] Greving, J. P., Wermer, M. J., Jr, M. J. B., Morit, A., Juvela, S., Yonekura, M., Ishibashi, T., Torner, J. C., Nakayama, T., Rinkel, G. J., and et. al. Development of the phases score for prediction of risk of rupture of intracranial aneurysms: a pooled analysis of six prospective cohort studies. *The Lancet Neurology 13*, 1 (2014), 59–66.

[126] gsam Kim, Y., Par, Y., and Lim, S. 3d simulations of blood flow dynamics in compliant vessels: normal, aneurysmal, and stenotic arteries. *Communications in Computational Physics 19*, 5 (2016), 1167–1190.

[127] Guo, D., Wang, Y.-W., Ma, J., Yan, L., Li, T.-F., Han, X.-W., and Shui, S.-F. Study on the role of cathepsin b and jnk signaling pathway in the development of cerebral aneurysm. *Asian Pacific journal of tropical medicine 9*, 5 (2016), 499–502.

[128] Gwilliam, M. N., Hoggard, N., Capener, D., Singh, P., Marzo, A., Verma, P. K., and Wilkinson, I. D. Mr derived volumetric flow rate

waveforms at locations within the common carotid, internal carotid, and basilar arteries. *Journal of Cerebral Blood Flow & Metabolism 29*, 12 (2009), 1975–1982.

[129] Ha, H., Kim, G. B., Kweon, J., Lee, S. J., Kim, Y.-H., Lee, D. H., Yang, D. H., and Kim, N. Hemodynamic measurement using four-dimensional phase-contrast mri: quantification of hemodynamic parameters and clinical applications. *Korean journal of radiology 17*, 4 (2016), 445–462.

[130] Hackenberg, K. A., Hänggi, D., and Etminan, N. Unruptured intracranial aneurysms: Contemporary data and management. *Stroke 49*, 9 (2018), 2268–2275.

[131] Hahn, C., and Schwartz, M. A. Mechanotransduction in vascular physiology and atherogenesis. *Nature reviews Molecular cell biology 10*, 1 (2009), 53–62.

[132] Haimes, R., and Kenwright, D. On the velocity gradient tensor and fluid feature extraction. In *14th Computational Fluid Dynamics Conference* (1999), p. 3288.

[133] Hanczar, B., Hu, J., Sim, C., Weinstein, J., Bittner, M., and RDougherty, E. Small-sample precision of roc-related estimates. *Bioinformatics 26*, 6 (2010), 822–830.

[134] Hanley, J. A., and McNeil, B. J. The meaning and use of the area under a receiver operating characteristic (roc) curve. *Radiology 143*, 1 (1982), 29–36.

[135] Hansen, K. L., Møller-Sørensen, H., Kjaergaard, J., Jensen, M. B., Jensen, J. A., and Nielsen, M. B. Aortic valve stenosis increases helical flow and flow complexity: A study of intra-operative cardiac vector flow imaging. *Ultrasound in Medicine & Biology 43*, 8 (2017), 1607 – 1617.

[136] Harding, I. C., Mitra, R., Mensah, S. A., Herman, I. M., and Ebong, E. E. Pro-atherosclerotic disturbed flow disrupts caveolin-1 expression, localization, and function via glycocalyx degradation. *Journal of translational medicine 16*, 1 (2018), 1–20.

[137] Harrell, F. E., Lee, K. L., and Mark, D. B. Multivariable prognostic models: issues in developing models, evaluating assumptions and adequacy, and measuring and reducing errors. *Statistics in medicine 15*, 4 (1996), 361–387.

[138] Hasan, D. M., Nadareyshvili, A. I., Hoppe, A. L., Mahane, K. B., Kung, D. K., and Raghavan, M. L. Cerebral aneurysm sac growth as the etiology of recurrence after successful coil embolization. *Stroke 43*, 3 (2012), 866–868.

[139] Hashimoto, T., Meng, H., and Young, W. Intracranial aneurysms: links among inflammation, hemodynamics and vascular remodeling. *Neurol Res 28* (2006), 372–380.

[140] He, X., and Ku, D. N. Pulsatile Flow in the Human Left Coronary Artery Bifurcation: Average Conditions. *Journal of Biomechanical Engineering 118*, 1 (02 1996), 74–82.

[141] Helmke, B. P. Molecular control of cytoskeletal mechanics by hemodynamic forces. *Physiology 20*, 1 (2005), 43–53.

[142] Heo, K.-S., Le, N.-T., Cushman, H. J., Giancursio, C. J., Chang, E., Woo, C.-H., Sullivan, M. A., Taunton, J., Yeh, E. T., Fujiwara, K., et al. Disturbed flow-activated p90rsk kinase accelerates atherosclerosis by inhibiting senp2 function. *The Journal of clinical investigation 125*, 3 (2015), 1299–1310.

[143] Hochmuth, R., Mohandas, N., Spaeth, E., Williamson, J., Blackshear Jr, P., and Johnson, D. Surface adhesion, deformation and detachment at low shear of red cells and white cells. *ASAIO Journal 18*, 1 (1972), 325–332.

[144] Hoi, Y., Wasserman, B. A., Xie, Y. J., Najjar, S. S., Ferruci, L., Lakatta, E. G., Gerstenblith, G., and Steinman, D. A. Characterization of volumetric flow rate waveforms at the carotid bifurcations of older adults. *Physiological measurement 31*, 3 (2010), 291.

[145] Holdsworth, D., Norley, C., Frayne, R., Steinman, D., and Rutt, B. Characterization of common carotid artery blood-flow waveforms in normal human subjects. *Physiological measurement 20*, 3 (1999), 219.

[146] Hoppe, A. L., Raghava, M. L., and Hasan, D. M. Comparison of the association of sac growth and coil compaction with recurrence in coil embolized cerebral aneurysms. *PloS one 10*, 4 (2015), e0123017.

[147] Huang, Z.-Q., Meng, Z.-H., Hou, Z.-J., Huang, S.-Q., Chen, J.-N., Yu, H., Feng, L.-J., Wang, Q.-J., Li, P.-A., and Wen, Z.-B. Geometric parameter analysis of ruptured and unruptured aneurysms in patients with symmetric bilateral intracranial aneurysms: A multicenter ct angiography study. *American Journal of Neuroradiology 37*, 8 (2016), 1413–1417.

[148] Hughes, J. D., Bond, K. M., Mekary, R. A., Dewan, M. C., Rattani, A., Baticulon, R., Kato, Y., Azevedo-Filho, H., Morcos, J. J., and Park, K. B. Estimating the global incidence of aneurysmal subarachnoid hemorrhage: a systematic review for central nervous system vascular lesions and meta-analysis of ruptured aneurysms. *World neurosurgery 115* (2018), 430–447.

[149] Humphrey, J. D., Schwartz, M. A., Tellides, G., and Milewicz, D. M. Role of mechanotransduction in vascular biology: focus on thoracic

aortic aneurysms and dissections. *Circulation research 116*, 8 (2015), 1448–1461.

[150] Hunt, J., Wray, A., and Moin, P. Eddies, streams, and convergence zones in turbulent flows. *Studying Turbulence Using Numerical Simulation Databases 1* (11 1988), 193–208.

[151] Huo, Y., Choy, J. S., Svendsen, M., Sinha, A. K., and Kassab, G. S. Effects of vessel compliance on flow pattern in porcine epicardial right coronary arterial tree. *Journal of biomechanics 42*, 5 (2009), 594–602.

[152] Ildiko, F. E., and Friedman, J. H. A statistical view of some chemometrics regression tools. *Technometrics 35*, 2 (1993), 109–135.

[153] Investigators, U. J. The natural course of unruptured cerebral aneurysms in a japanese cohort. *New England Journal of Medicine 366*, 26 (2012), 2474–2482.

[154] Irace, C., Carallo, C., De Franceschi, M. S., Scicchitano, F., Milano, M., Tripolino, C., Scavelli, F., and Gnasso, A. Human common carotid wall shear stress as a function of age and gender: a 12-year follow-up study. *Age 34*, 6 (2012), 1553–1562.

[155] Jain, K. Mechanism of rupture of intracranial saccular aneurysms. *Surgery 54*, 2 (1963), 347–350.

[156] Jain, K., Jiang, J., Strother, C., and Mardal, K.-A. Transitional hemodynamics in intracranial aneurysms—comparative velocity investigations with high resolution lattice boltzmann simulations, normal resolution ansys simulations, and mr imaging. *Medical physics 43*, 11 (2016), 6186–6198.

[157] James, G., Witten, D., Hastie, T., and Tibshirani, R. *An introduction to statistical learning*, vol. 112. Springer, 2013.

[158] Jenkins, N. T., Padilla, J., Boyle, L. J., Credeur, D. P., Laughlin, M. H., and Fadel, P. J. Disturbed blood flow acutely induces activation and apoptosis of the human vascular endothelium. *Hypertension 61*, 3 (2013), 615–621.

[159] Jeong, J., and Hussain, F. On the identification of a vortex. *Journal of fluid mechanics 285* (1995), 69–94.

[160] Jia, L.-X., Zhang, W.-M., Zhang, H.-J., Li, T.-T., Wang, Y.-L., Qin, Y.-W., Gu, H., and Du, J. Mechanical stretch-induced endoplasmic reticulum stress, apoptosis and inflammation contribute to thoracic aortic aneurysm and dissection. *The Journal of pathology 236*, 3 (2015), 373–383.

[161] Jiang, J., and Strother, C. M. Interactive decomposition and mapping of saccular cerebral aneurysms using harmonic functions: its first application with "patient-specific" computational fluid dynamics (cfd) simulations. *IEEE transactions on medical imaging 32*, 2 (2013), 153–164.

[162] Jiang, M., Machiraju, R., and Thompson, D. Detection and visualization of vortices. *The visualization handbook 295* (2005).

[163] Jiang, P., Liu, Q., Wu, J., Chen, X., Li, M., Li, Z., Yang, S., Guo, R., Gao, B., Cao, Y., et al. A novel scoring system for rupture risk stratification of intracranial aneurysms: a hemodynamic and morphological study. *Frontiers in neuroscience 12* (2018), 596.

[164] Jing, L., Fan, J., Wang, Y., Li, H., Wang, S., Yang, X., and Zhang, Y. Morphologic and hemodynamic analysis in the patients with multiple intracranial aneurysms: Ruptured versus unruptured. *PLOS ONE 10*, 7 (07 2015), 1–12.

[165] Johnston, R., Jones, K., and Manley, D. Confounding and collinearity in regression analysis: a cautionary tale and an alternative procedure, illustrated by studies of british voting behaviour. *Quality & quantity 52*, 4 (2018), 1957–1976.

[166] Jou, L., and Britz, G. Correlation between aneurysm size and hemodynamics in one individual with multiple small intracranial aneurysms. *Cureus 8*, 7 (2016).

[167] Jou, L.-D., Lee, D., Morsi, H., and Mawad, M. Wall shear stress on ruptured and unruptured intracranial aneurysms at the internal carotid artery. *American Journal of Neuroradiology 29*, 9 (2008), 1761–1767.

[168] Jr, M. A. G., and García-Cardeña, G. Endothelial cell dysfunction and the pathobiology of atherosclerosis. *Circulation research 118*, 4 (2016), 620–636.

[169] Jr, T. R. F., Benitez, R., Veznedaroglu, E., Sharan, A., Mitchell, W., Silva, M., and Rosenwasser, R. H. A review of size and location of ruptured intracranial aneurysms. *Neurosurgery 49*, 6 (2001), 1322–1326.

[170] Jung, K.-H. New pathophysiological considerations on cerebral aneurysms. *Neurointervention 13*, 2 (2018), 73.

[171] Juvela, S. Risk factors for multiple intracranial aneurysms. *Stroke 31*, 2 (2000), 392–397.

[172] Juvela, S., Poussa, K., Lehto, H., and Porras, M. Natural history of unruptured intracranial aneurysms: a long-term follow-up study. *Stroke 44*, 9 (2013), 2414–2421.

[173] Karino, T., and Goldsmith, H. Flow behaviour of blood cells and rigid spheres in an annular vortex. *Phil. Trans. R. Soc. Lond. B 279*, 967 (1977), 413–445.

[174] Kashiwazaki, D., and Kuroda, S. Size ratio can highly predict rupture risk in intracranial small ($<$ 5 mm) aneurysms. *Stroke 44*, 8 (2013), 2169–2173.

[175] Kaufmann, B. A., Sanders, J. M., Davis, C., Xie, A., Aldred, P., Sarembock, I. J., and Lidner, J. R. Molecular imaging of inflammation

in atherosclerosis with targeted ultrasound detection of vascualr cell adhesion molecule-1. *Circulation 116*, 3 (2007), 276–284.

[176] Kaur, H., Carriveau, R., and Mutus, B. A simple parallel plate flow chamber to study effects of shear stress on endothelial cells. *Am. J. Biomed. Sci 4*, 1 (2012), 70–78.

[177] Kelsey, L. J., Powell, J. T., Norman, P. E., Miller, K., and Doyle, B. J. A comparison of hemodynamic metrics and intraluminal thrombus burden in a common iliac artery aneurysm. *International journal for numerical methods in biomedical engineering 33*, 5 (2017), e2821.

[178] Khan, M., Valen-Sendstad, K., and Steinman, D. Narrowing the expertise gap for predicting intracranial aneurysm hemodynamics: impact of solver numerics versus mesh and time-step resolution. *American Journal of Neuroradiology* (2015).

[179] Khandelwal, N., Simpson, J., Taylor, G., Rafique, S., Whitehouse, A., Hiscox, J., and Stark, L. Nucleolar nf-κ b/rela mediates apoptosis by causing cytoplasmic relocalization of nucleophosmin. *Cell Death & Differentiation 18*, 12 (2011), 1889–1903.

[180] Kim, M.-C., Nam, J. H., and Lee, C.-S. Near-wall deposition probability of blood elements as a new hemodynamic wall parameter. *Annals of Biomedical Engineering 34*, 6 (Jun 2006), 958–970.

[181] Kim, S., and Woo, C.-H. Laminar flow inhibits er stress-induced endothelial apoptosis through pi3k/akt-dependent signaling pathway. *Molecules and cells 41*, 11 (2018), 964.

[182] Klaus, V., Tanios-Schmies, F., Reeps, C., Trenner, M., Matevossian, E., Eckstein, H.-H., and Pelisek, J. Association of matrix metalloproteinase levels with collagen degradation in the context of abdominal aortic aneurysm. *European Journal of Vascular and Endovascular Surgery 53*, 4 (2017), 549–558.

[183] Kocur, D., Przybyłko, N., Niedbała, M., and Rudnik, A. Alternative definitions of cerebral aneurysm morphologic parameters have an impact on rupture risk determination. *World neurosurgery 126* (2019), e157–e164.

[184] Köhler, B., Gasteiger, R., Preim, U., Theisel, H., Gutberlet, M., and Preim, B. Semi-automatic vortex extraction in 4d pc-mri cardiac blood flow data using line predicates. *IEEE Transactions on Visualization and Computer Graphics 19*, 12 (2013), 2773–2782.

[185] Kolář, V. Vortex identification: New requirements and limitations. *International journal of heat and fluid flow 28*, 4 (2007), 638–652.

[186] Komotar, R. J., Mocco, J., and Solomon, R. A. Guidelines for the surgical treatment of unruptured intracranial aneurysms: the first annual j.

lawrence pool memorial research symposium—controversies in the management of cerebral aneurysms. *Neurosurgery 62*, 1 (2008), 183–194.

[187] Korja, M., Lehto, H., and Juvela, S. Lifelong rupture risk of intracranial aneurysms depends on risk factors. *Stroke 45*, 7 (2014), 1958–1963.

[188] Kosierkiewicz, T., Factor, S., and Dickson, D. Immunocytochemical studies of atherosclerotic lesions of cerebral berry aneurysms. *J Neuropathol Exp Neurol 53*, 4 (1994), 399–406.

[189] Kotowski, M., Naggara, O., Darsaut, T. E., Nolet, S., Gevry, G., Kouznetsov, E., and Raymond, J. Safety and occlusion rates of surgical treatment of unruptured intracranial aneurysms: a systematic review and meta-analysis of the literature from 1990 to 2011. *Journal of Neurology, Neurosurgery & Psychiatry 84*, 1 (2013), 42–48.

[190] Ku, D., Gidden, D., Phillips, D., and Jr, D. S. Hemodynamics of the normal human carotid bifurcation: in vitro and in vivo studies. *Ultrasound in medicine & biology 11*, 1 (1985), 13–26.

[191] Ku, D., Giddens, D. P., Zarins, C. K., and Glagov, S. Pulsatile flow and atherosclerosis in the human carotid bifurcation. positive correlation between plaque location and low oscillating shear stress. *Arteriosclerosis: An Official Journal of the American Heart Association, Inc. 5*, 3 (1985), 293–302.

[192] Kulcsár, Z., Ugron, A., Berentei, Z., Paál, G., Szikora, I., and et al. Hemodynamics of cerebral aneurysm initiation: the role of wall shear stress and spatial wall shear stress gradient. *American Journal of neuroradiology* (2011).

[193] Kumar, D., Vinoth, R., and Raviraj Adhikari, V. S. Non-newtonian and newtonian blood flow in human aorta: a transient analysis. *Biomedical Research 28* (2017).

[194] Landry, A. P., Balas, M., Spears, J., and Zador, Z. Microenvironment of ruptured cerebral aneurysms discovered using data driven analysis of gene expression. *PLOS ONE 14*, 7 (07 2019), 1–12.

[195] Lasheras, J. C. The biomechanics of arterial aneurysms. *Annual Review of Fluid Mechanics 39*, 1 (2007), 293–319.

[196] Lauric, A., Safain, M. G., Hippelheuser, J., and Malek, A. M. High curvature of the internal carotid artery is associated with the presence of intracranial aneurysms. *Journal of neurointerventional surgery 6*, 10 (2014), 733–739.

[197] Lay, A. J., Coleman, P. R., Formaz-Preston, A., Ting, K. K., Roediger, B., Weninger, W., Schwartz, M. A., Vadas, M. A., and Gamble, J. R. Arhgap18: A flow-responsive gene that regulates endothelial cell

alignment and protects against atherosclerosis. *Journal of the American Heart Association 8*, 2 (2019), e010057.

[198] Leach, J. R., Kao, E., Zhu, C., Saloner, D., and Hope, M. D. On the relative impact of intraluminal thrombus heterogeneity on abdominal aortic aneurysm mechanics. *Journal of biomechanical engineering 141*, 11 (2019).

[199] Lee, G., Eom, K., Lee, C., Kim, D., and Kang, S. Rupture of very small intracranial aneurysms: Incidence and clinical characteristics. *J Cerebrovasc Endovasc Neurosurg 17(3)* (2015), 217–222.

[200] Lee, J., Packard, R. R. S., and Hsiai, T. K. Blood flow modulation of vascular dynamics. *Current opinion in lipidology 26*, 5 (2015), 376.

[201] Lee, W. H., Kang, S., Vlachos, P. P., and Lee, Y. W. A novel in vitro ischemia/reperfusion injury model. *Archives of pharmacal research 32*, 3 (2009), 421–429.

[202] Leopardi, P. A partition of the unit sphere into regions of equal area and small diameter. *Electron. Trans. Numer. Anal. 25* (01 2006).

[203] Li, H., Lin, K., and Shahmirzadi, D. Fsi simulations of pulse wave propagation in human abdominal aortic aneurysm: The effects of sac geometry and stiffness. *Biomedical engineering and computational biology 7* (2016), BECB–S40094.

[204] Li, S., Xu, J., Yao, W., Li, H., Liu, Q., Xiao, F., Irwin, M. G., Xia, Z., and Ruan, W. Sevoflurane pretreatment attenuates tnf-α-induced human endothelial cell dysfunction through activating enos/no pathway. *Biochemical and biophysical research communications 460*, 3 (2015), 879–886.

[205] Li, T., Wang, H., Li, X., Ge, H., Sun, H., and Ma, D. Predictive significance of vegfa variations in intracranial aneurysm. *Int J Clin Exp Med 10*, 9 (2017), 13802–13807.

[206] Li, W., and Wang, W. Structural alteration of the endothelial glycocalyx: contribution of the actin cytoskeleton. *Biomechanics and modeling in mechanobiology 17*, 1 (2018), 147–158.

[207] Li, X., Fang, Q., Tian, X., Wang, X., Ao, Q., Hou, W., Tong, H., Fan, J., and Bai, S. Curcumin attenuates the development of thoracic aortic aneurysm by inhibiting vegf expression and inflammation. *Molecular medicine reports 16*, 4 (2017), 4455–4462.

[208] Liu, J., Jing, L., Wang, C., Zhang, Y., and Yang, X. Recanalization, regrowth, and delayed rupture of a previously coiled unruptured anterior communicating artery aneurysm: a longitudinal hemodynamic analysis. *World neurosurgery 89* (2016), 726–e5.

[209] Liu, P., Song, Y., Zhou, Y., Liu, Y., Qiu, T., An, Q., Song, J., Li, P., Shi, Y., Li, S., et al. Cyclic mechanical stretch induced smooth muscle cell

changes in cerebral aneurysm progress by reducing collagen type iv and collagen type vi levels. *Cellular Physiology and Biochemistry 45*, 3 (2018), 1051–1060.

[210] Liu, X., Sun, A., Fan, Y., and Deng, X. Physiological significance of helical flow in the arterial system and its potential clinical applications. *Annals of Biomedical Engineering 43*, 1 (Jan 2015), 3–15.

[211] Longo, M., Granata, F., Racchiusa, S., Mormina, E., Grasso, G., Longo, G. M., Garufi, G., Salpietro, F. M., and Alafaci, C. Role of hemodynamic forces in unruptured intracranial aneurysms: An overview of a complex scenario. *World Neurosurgery 105* (2017), 632 – 642.

[212] Lorensen, W. E., and Cline, H. E. Marching cubes: A high resolution 3d surface construction algorithm. In *ACM siggraph computer graphics* (1987), vol. 21, ACM, pp. 163–169.

[213] Ma, D., Tremmel, M., Paluch, R. A., Levy, E. L. I., Meng, H., and Mocco, J. Size ratio for clinical assessment of intracranial aneurysm rupture risk. *Neurological research 32*, 5 (2010), 482–486.

[214] Ma, J., Wang, C., Shene, C.-K., and Jiang, J. A graph-based interface for visualanalytics of 3d streamlines and pathlines. *IEEE transactions on visualization and computer graphics 20*, 8 (2014), 1127–1140.

[215] Maamoun, H., Abdelsalam, S. S., Zeidan, A., Korashy, H. M., and Agouni, A. Endoplasmic reticulum stress: A critical molecular driver of endothelial dysfunction and cardiovascular disturbances associated with diabetes. *International journal of molecular sciences 20*, 7 (2019), 1658.

[216] Mahmoud, M., Kim, R., de Luca, A., Gauci, I., Hsiao, S., and Evans, P. 189 disturbed flow promotes endothelial cell injury via the induction of developmental genes. *Heart 100*, Suppl 3 (2014), A105–A105.

[217] Mannino, R. G., Myers, D. R., Ahn, B., Wang, Y., Rollins, M., Gole, H., Lin, A. S., Guldberg, R. E., Giddens, D. P., Timmins, L. H., and et. al. Do-it-yourself in vitro vasculature that recapitulates in vivo geometries for investigating endothelial-blood cell interactions. *Scientific reports 5* (2015), 12401.

[218] Mantha, A., Karmonik, C., Benndorf, G., Strother, C., and Metcalfe, R. Hemodynamics in a cerebral artery before and after the formation of an aneurysm. *American Journal of Neuroradiology 27*, 5 (2006), 1113–1118.

[219] Mao, X., Xie, L., Greenberg, R. B., Greenberg, J. B., Peng, B., Mieling, I., Jin, K., and Greenberg, D. A. Flow-induced regulation of brain endothelial cells in vitro. *Vascular pharmacology 62*, 2 (2014), 82–87.

[220] Markl, M., Wegent, F., Zech, T., Bauer, S., Strecker, C., Schumacher, M., Weiller, C., Hennig, J., and Harloff, A. In vivo wall

shear stress distribution in the carotid artery: effect of bifurcation geometry, internal carotid artery stenosis, and recanalization therapy. *Circulation: Cardiovascular Imaging 3*, 6 (2010), 647–655.

[221] Martin, D., Li, Y., Yang, J., Wang, G., Margariti, A., Jiang, Z., Yu, H., Zampetaki, A., Hu, Y., Xu, Q., et al. Unspliced x-box-binding protein 1 (xbp1) protects endothelial cells from oxidative stress through interaction with histone deacetylase 3. *Journal of Biological Chemistry 289*, 44 (2014), 30625–30634.

[222] Mascitelli, J. R., Oermann, E. K., Leacy, R. A. D., Moyle, H., Mocco, J., and Patel, A. B. Predictors of treatment failure following coil embolization of intracranial aneurysms. *Journal of Clinical Neuroscience 22*, 8 (2015), 1275–1281.

[223] McDonald, K. K., Cooper, S., Danielzak, L., and Leask, R. L. Glycocalyx degradation induces a proinflammatory phenotype and increased leukocyte adhesion in cultured endothelial cells under flow. *PloS one 11*, 12 (2016).

[224] McDowell, M. M., Zhao, Y., Kellner, C. P., Barton, S. M., Sussman, E., Claassen, J., Ducruet, A. F., and Connolly, E. S. Demographic and clinical predictors of multiple intracranial aneurysms in patients with subarachnoid hemorrhage. *Journal of Neurosurgery JNS 128*, 4 (2018), 961 – 968.

[225] McDowell, M. M., Zhao, Y., Kellner, C. P., Barton, S. M., Sussman, E., Claassen, J., Ducruet, A. F., and Connolly, E. S. Demographic and clinical predictors of multiple intracranial aneurysms in patients with subarachnoid hemorrhage. *Journal of neurosurgery 128*, 4 (2018), 961–968.

[226] McIlwain, D. R., Berger, T., and Mak, T. W. Caspase functions in cell death and disease. *Cold Spring Harbor perspectives in biology 5*, 4 (2013), a008656.

[227] Meckel, S., Stalder, A. F., Santini, F., Radü, E.-W., Rüfenacht, D. A., Markl, M., and Wetzel, S. G. In vivo visualization and analysis of 3-d hemodynamics in cerebral aneurysms with flow-sensitized 4-d mr imaging at 3 t. *Neuroradiology 50*, 6 (2008), 473–484.

[228] Meng, H., Tutino, V. M., Xiang, J., and Siddiqui, A. High wss or low wss? complex interactions of hemodynamics with intracranial aneurysm initiation, growth, and rupture: Toward a unifying hypothesis. *American Journal of Neuroradiology 35*, 7 (2014), 1254–1262.

[229] Miao, H., Hu, Y.-L., Shiu, Y.-T., Yuan, S., Zhao, Y., Kaunas, R., Wang, Y., Jin, G., Usami, S., and Chien, S. Effects of flow patterns on the localization and expression of ve-cadherin at vascular endothelial cell junctions: In vivo and in vitro investigations. *Journal of vascular research 42* (01 2005), 77–89.

[230] Michel, J.-B., Jondeau, G., and Milewicz, D. M. From genetics to response to injury: vascular smooth muscle cells in aneurysms and dissections of the ascending aorta. *Cardiovascular research 114*, 4 (2018), 578–589.

[231] Milln, J., Cain, R. J., Reglero-Real, N., Bigarella, C., Marcos-Ramiro, B., Fernndez-Martn, L., Correas, I., and Ridley, A. J. Adherens junctions connect stress fibres between adjacent endothelial cells. *BMC biology 8*, 1 (2010), 11.

[232] Mitra, R., Qiao, J., Madhavan, S., O'Neil, G. L., Ritchie, B., Kulkarni, P., Sridhar, S., van de Ven, A. L., Kemmerling, E. M. C., Ferris, C., et al. The comparative effects of high fat diet or disturbed blood flow on glycocalyx integrity and vascular inflammation. *Translational medicine communications 3*, 1 (2018), 1–15.

[233] Miura, Y., Ishida, F., Umeda, Y., Tanemura, H., Suzuki, H., Matsushima, S., Shimosaka, S., and Taki, W. Low wall shear stress is independently associated with the rupture status of middle cerebral artery aneurysms. *Stroke 44*, 2 (2013), 519–521.

[234] Mocco, J., Brown Jr, R. D., Torner, J. C., Capuano, A. W., Fargen, K. M., Raghavan, M. L., Piepgras, D. G., Meissner, I., III, J. H., and of Unruptured Intracranial Aneurysms Investigators, I. S. Aneurysm morphology and prediction of rupture: an international study of

unruptured intracranial aneurysms analysis. *Neurosurgery 82*, 4 (2018), 491–496.

[235] Mohan, D., Munteanu, V., Coman, T., and Ciurea, A. Genetic factors involves in intracranial aneurysms–actualities. *Journal of medicine and life 8*, 3 (2015), 336.

[236] Molyneux, A., Kerr, R., Group, I. S. A. T. I. C., et al. International subarachnoid aneurysm trial (isat) of neurosurgical clipping versus endovascular coiling in 2143 patients with ruptured intracranial aneurysms: a randomized trial. *Journal of stroke and cerebrovascular diseases 11*, 6 (2002), 304–314.

[237] Morbiducci, U., Kok, A. M., Kwak, B. R., Stone, P. H., Steinman, D. A., and Wentzel, J. J. Atherosclerosis at arterial bifurcations: evidence for the role of haemodynamics and geometry. *Thrombosis and haemostasis 115*, 03 (2016), 484–492.

[238] Moriguchi, T., and Sumpio, B. E. Pecam-1 phosphorylation and tissue factor expression in huvecs exposed to uniform and disturbed pulsatile flow and chemical stimuli. *Journal of vascular surgery 61*, 2 (2015), 481–488.

[239] Mullin, T., Shipton, S., and Tavener, S. Flow in a symmetric channel with an expanded section. *Fluid dynamics research 33*, 5-6 (2003), 433.

[240] Munarriz, P. M., Gómez, P. A., Paredes, I., Castaño-Leon, A. M., Cepeda, S., and Lagares, A. Basic principles of hemodynamics and cerebral aneurysms. *World neurosurgery 88* (2016), 311–319.

[241] Mundi, S., Massaro, M., Scoditti, E., Carluccio, M. A., van Hinsbergh, V. W., Iruela-Arispe, M. L., and De Caterina, R. Endothelial permeability, ldl deposition, and cardiovascular risk factors—a review. *Cardiovascular research 114*, 1 (2018), 35–52.

[242] Mundi, S., Massaro, M., Scoditti, E., Carluccio, M. A., van Hinsbergh, V. W. M., Iruela-Arispe, M. L., and De Caterina, R. Endothelial permeability, LDL deposition, and cardiovascular risk factors—a review. *Cardiovascular Research 114*, 1 (12 2017), 35–52.

[243] Mussbacher, M., Salzmann, M., Brostjan, C., Hoesel, B., Schoergenhofer, C., Datler, H., Hohensinner, P., Basílio, J., Petzelbauer, P., Assinger, A., et al. Cell type-specific roles of nf-κb linking inflammation and thrombosis. *Frontiers in immunology 10* (2019).

[244] Mut, F., Löhner, R., Chien, A., Tateshima, S., Viñuela, F., Putman, C., and Cebral, J. R. Computational hemodynamics framework for the analysis of cerebral aneurysms. *International Journal for Numerical Methods in Biomedical Engineering 27*, 6 (2011), 822–839.

[245] Mynard, J. P., Wasserman, B. A., and Steinman, D. A. Errors in the estimation of wall shear stress by maximum doppler velocity. *Atherosclerosis 227*, 2 (2013), 259 – 266.

[246] Nakajima, H., and Mochizuki, N. Flow pattern-dependent endothelial cell responses through transcriptional regulation. *Cell Cycle 16*, 20 (2017), 1893–1901.

[247] Nakazaki, M., Nonaka, T., Nomura, T., Onda, T., Yonemasu, Y., Takahashi, A., Hashimoto, Y., Honda, O., Oka, S., Sasaki, M., Daibo, M., and Honmou, O. Cerebral aneurysm neck diameter is an independent predictor of progressive occlusion after stent-assisted coiling. *Acta Neurochirurgica 159*, 7 (Jul 2017), 1313–1319.

[248] Nazari-Jahantigh, M., Egea, V., Schober, A., and Weber, C. Microrna-specific regulatory mechanisms in atherosclerosis. *Journal of molecular and cellular cardiology 89* (2015), 35–41.

[249] Ngok, S. P., Geyer, R., Liu, M., Kourtidis, A., Agrawal, S., Wu, C., Seerapu, H. R., Lewis-Tuffin, L. J., Moodie, K. L., Huveldt, D., et al. Vegf and angiopoietin-1 exert opposing effects on cell junctions by regulating the rho gef syx. *Journal of Cell Biology 199*, 7 (2012), 1103–1115.

[250] Nobari, S., Mongrain, R., Leask, R., and Cartier, R. The effect of aortic wall and aortic leaflet stiffening on coronary hemodynamic: a fluid–structure interaction study. *Medical & biological engineering & computing 51*, 8 (2013), 923–936.

[251] Nowicki, K. W., Hosaka, K., He, Y., McFetridge, P. S., Scott, E. W., and Hoh, B. L. Novel high-throughput in vitro model for identifying hemodynamic-induced inflammatory mediators of cerebral aneurysm formation. *Hypertension 64*, 6 (2014), 1306–1313.

[252] Oeltze-Jafra, S., Cebral, J. R., Janig, G., and Preim, B. Cluster analysis of vortical flow in simulations of cerebral aneurysm hemodynamics. *IEEE transactions on visualization and computer graphics 22*, 1 (2016), 757–766.

[253] Ollikainen, E., Tulamo, R., Lehti, S., Lee-Rueckert, M., Hernesniemi, J., Niemelä, M., Ylä-Herttuala, S., Kovanen, P. T., and Frösen, J. Smooth muscle cell foam cell formation, apolipoproteins, and abca1 in intracranial aneurysms: Implications for lipid accumulation as a promoter of aneurysm wall rupture. *Journal of Neuropathology and Experimental Neurology 75*, 7 (2016), 689–699.

[254] Otani, T., Nakamura, M., Fujinaka, T., Hirata, M., Kuroda, J., Shibano, K., and Wada, S. Computational fluid dynamics of blood flow in

coil-embolized aneurysms: effect of packing density on flow stagnation in an idealized geometry. *Medical & biological engineering & computing 51*, 8 (2013), 901–910.

[255] Oubel, E., Craene, M. D., Putman, C. M., Cebral, J. R., and Frangi, A. F. Analysis of intracranial aneurysm wall motion and its effects on hemodynamic patterns. In *Medical Imaging 2007: Physiology, Function, and Structure from Medical Images* (2007), vol. 6511, International Society for Optics and Photonics, p. 65112A.

[256] Pan, L., Hong, Z., Yu, L., Gao, Y., Zhang, R., Feng, H., Su, L., and Wang, G. Shear stress induces human aortic endothelial cell apoptosis via interleukin-1 receptor-associated kinase 2-induced endoplasmic reticulum stress. *Molecular medicine reports 16*, 5 (2017), 7205–7212.

[257] Papaioannou, T. G., and Stefanadis, C. Vascular wall shear stress: basic principles and methods. *Hellenic J Cardiol 46*, 1 (2005), 9–15.

[258] peng Xiao, Z., lan Zhao, J., lin Rong, W., wen Jiang, J., and hua Li, M. Role of vascular endothelialâ^'cadherin and p120-catenin in the formation of experimental intracranial aneurysm in animals. *World Neurosurgery 128* (2019), e177 – e184.

[259] Penn, D. L., Witte, S. R., Komotar, R. J., and Jr, E. S. C. The role of vascular remodeling and inflammation in the pathogenesis of intracranial aneurysms. *Journal of clinical neuroscience 21*, 1 (2014), 28–32.

[260] Pera, J., Korostynski, M., Krzyszkowski, T., Czopek, J., Slowik, A., Dziedzic, T., Piechota, M., Stachura, K., Moskala, M., Przewlocki, R., and Szczudlik, A. Gene expression profiles in human ruptured and unruptured intracranial aneurysms. *Stroke 41*, 2 (2010), 224–231.

[261] Perrin, M. Venous aneurysms. *Phlebolymphology 13*, 3 (2006), 172.

[262] Perrone, R. D., Malek, A. M., and Watnick, T. Vascular complications in autosomal dominant polycystic kidney disease. *Nature Reviews Nephrology 11*, 10 (2015), 589.

[263] Peshkova, I. O., Schaefer, G., and Koltsova, E. K. Atherosclerosis and aortic aneurysm–is inflammation a common denominator? *The FEBS journal 283*, 9 (2016), 1636–1652.

[264] Piccinelli, M., Steinman, D. A., Hoi, Y., Tong, F., Veneziani, A., and Antiga, L. Automatic neck plane detection and 3d geometric characterization of aneurysmal sacs. *Annals of BIomedical Engineering 40*, 10 (2012), 2188–2211.

[265] Poduri, A., Chang, A. H., Raftrey, B., Rhee, S., Van, M., and Red-Horse, K. Endothelial cells respond to the direction of mechanical stimuli

through smad signaling to regulate coronary artery size. *Development 144*, 18 (2017), 3241–3252.

[266] Poethke, J., Spuler, A., Petz, C., Hege, H.-C., Goubergrits, L., Affeld, K., and Kertzscher, U. Cerebral aneurysm hemodynamics and a length of parent vessel. In *World Congress on Medical Physics and Biomedical Engineering, September 7-12, 2009, Munich, Germany* (2009), Springer, pp. 1608–1611.

[267] Potter, D. R., and Damiano, E. R. The hydrodynamically relevant endothelial cell glycocalyx observed in vivo is absent in vitro. *Circulation research 102*, 7 (2008), 770–776.

[268] Potters, W. V., Marquering, H. A., VanBavel, E., and Nederveen, A. J. Measuring wall shear stress using velocity-encoded mri. *Current Cardiovascular Imaging Reports 7*, 4 (2014), 9257.

[269] Qian, Z., Kang, H., Tang, K., Jiang, C., Wu, Z., Li, Y., and Liu, A. Assessment of risk of aneurysmal rupture in patients with normotensives, controlled hypertension, and uncontrolled hypertension. *Journal of Stroke and Cerebrovascular Diseases 25*, 7 (2016), 1746–1752.

[270] Qin, H., Yang, Q., Zhuang, Q., Long, J., Yang, F., and Zhang, H. Morphological and hemodynamic parameters for middle cerebral artery bifurcation

aneurysm rupture risk assessment. *Journal of Korean Neurosurgical Society 60*, 5 (2017), 504.

[271] Qiu, J., Zheng, Y., Hu, J., Liao, D., Gregersen, H., Deng, X., Fan, Y., and Wang, G. Biomechanical regulation of vascular smooth muscle cell functions: from in vitro to in vivo understanding. *Journal of The Royal Society Interface 11*, 90 (2014), 20130852.

[272] Ramella, M., Bernardi, P., Fusaro, L., Manfredi, M., Casella, F., Porta, C. M., Nicolai, L., Galeazzi, E., Boldorini, R., Settembrini, A. M., et al. Relevance of inflammation and matrix remodeling in abdominal aortic aneurysm (aaa) and popliteal artery aneurysm (paa) progression. *American journal of translational research 10*, 10 (2018), 3265.

[273] Rami, L., Auguste, P., Thebaud, N. B., Bareille, R., Daculsi, R., Ripoche, J., and Bordenave, L. Iq domain gtpase-activating protein 1 is involved in shear stress-induced progenitor-derived endothelial cell alignment. *PloS one 8*, 11 (2013), e79919.

[274] Rayz, V., Boussel, L., Lawton, M., Acevedo-Bolton, G., Ge, L., Young, W., Higashida, R., and Saloner, D. Numerical modeling of the flow in intracranial aneurysms: prediction of regions prone to thrombus formation. *Annals of biomedical engineering 36*, 11 (2008), 1793.

[275] Reglero-Real, N., Colom, B., Bodkin, J. V., and Nourshargh, S. Endothelial cell junctional adhesion molecules: role and regulation of expression in inflammation. *Arteriosclerosis, thrombosis, and vascular biology 36*, 10 (2016), 2048–2057.

[276] Revilla-Pacheco, F., Escalante-Seyffert, M. C., Herrada-Pineda, T., Manrique-Guzman, S., Perez-Zuniga, I., Rangel-Suarez, S., Rubalcava-Ortega, J., and Loyo-Varela, M. Prevalence of incidental clinoid segment saccular aneurysms. *World neurosurgery 115* (2018), e244–e251.

[277] Rinne, J., Hernesniemi, J., Puranen, M., and Saari, T. Multiple intracranial aneurysms in a defined population: prospective angiographic and clinical study. *Neurosurgery 35*, 5 (1994), 803–808.

[278] Robertson, A. M., Duan, X., Aziz, K. M., Hill, M. R., Watkins, S. C., and Cebral, J. R. Diversity in the strength and structure of unruptured cerebral aneurysms. *Annals of biomedical engineering 43*, 7 (2015), 1502–1515.

[279] Rodríguez-Pérez, R., Vogt, M., and Bajorath, J. Influence of varying training set composition and size on support vector machine-based prediction of active compounds. *Journal of chemical information and modeling 57*, 4 (2017), 710–716.

[280] Rossitti, S. Shear stress in cerebral arteries carrying saccular aneurysms: a preliminary study. *Acta Radiologica 39*, 6 (1998), 711–717.

[281] Sato, M., Nagayama, K., Kataoka, N., Sasaki, M., and Hane, K. Local mechanical properties measured by atomic force microscopy for cultured bovine endothelial cells exposed to shear stress. *Journal of biomechanics 33*, 1 (2000), 127–135.

[282] Savastano, L. E., Bhambri, A., Wilkinson, D. A., and Pandey, A. S. Biology of cerebral aneurysm formation, growth, and rupture. In *Intracranial Aneurysms*. Elsevier, 2018, pp. 17–32.

[283] Sawyer, D. M., Pace, L. A., Pascale, C. L., Kutchin, A. C., O'Neill, B. E., Starke, R. M., and Dumont, A. S. Lymphocytes influence intracranial aneurysm formation and rupture: role of extracellular matrix remodeling and phenotypic modulation of vascular smooth muscle cells. *Journal of neuroinflammation 13*, 1 (2016), 185.

[284] Schafhitzel, T., Vollrath, J. E., Gois, J. P., Weiskopf, D., Castelo, A., and Ertl, T. Topology-preserving λ_2-based vortex core line detection for flow visualization. *Computer Graphics Forum 27*, 3 (2008), 1023–1030.

[285] Schiffrin, E. L. Novel mechanisms of hypertension and vascular dysfunction. *Nature Reviews Nephrology 14*, 2 (2018), 73–74.

[286] Schneiders, J., Marquering, H., Van den Berg, R., VanBavel, E., Velthuis, B., Rinkel, G., and Majoie, C. Rupture-associated changes

of cerebral aneurysm geometry: high-resolution 3d imaging before and after rupture. *American Journal of Neuroradiology 35*, 7 (2014), 1358–1362.

[287] Seebach, J., Donnert, G., Kronstein, R., Werth, S., Wojciak-Stothard, B., Falzarano, D., Mrowietz, C., Hell, S. W., and Schnittler, H.-J. Regulation of endothelial barrier function during flow-induced conversion to an arterial phenotype. *Cardiovascular research 75*, 3 (2007), 598–607.

[288] Serbanovic-Canic, J., de Luca, A., Warboys, C., Ferreira, P. F., Luong, L. A., Hsiao, S., Gauci, I., Mahmoud, M., Feng, S., Souilhol, C., et al. Zebrafish model for functional screening of flow-responsive genes. *Arteriosclerosis, thrombosis, and vascular biology 37*, 1 (2017), 130–143.

[289] Sforza, D. M., Putman, C. M., and Cebral, J. R. Hemodynamics of cerebral aneurysms. *Annual review of fluid mechanics 41* (2009), 91–107.

[290] Shabadi, V., Shabadi, S., and Chandramohan, J. Aneurysmal subarachnoid hemorrhage and its practical implications in a peripheral set-up. *International Journal of Advanced Research 5* (02 2017), 821–826.

[291] Shannon, C. E. A mathematical theory of communication. *Bell system technical journal 27*, 3 (1948), 379–423.

[292] Shannon, C. E. A mathematical theory of communication. *ACM SIGMOBILE Mobile Computing and Communications Review 5*, 1 (2001), 3–55.

[293] Shav, D., Gotlieb, R., Zaretsky, U., Elad, D., and Einav, S. Wall shear stress effects on endothelial-endothelial and endothelial-smooth muscle cell interactions in tissue engineered models of the vascular wall. *PLoS One 9*, 2 (2014).

[294] Sheinberg, D. L., McCarthy, D. J., Elwardany, O., Bryant, J.-P., Luther, E., Chen, S. H., Thompson, J. W., and Starke, R. M. Endothelial dysfunction in cerebral aneurysms. *Neurosurgical focus 47*, 1 (2019), E3.

[295] Shihata, W. A., Michell, D. L., Andrews, K. L., and Chin-Dusting, J. P. F. Caveolae: A role in endothelial inflammation and mechanotransduction? *Frontiers in Physiology 7* (2016), 628.

[296] Shimizu, K., Kushamae, M., Mizutani, T., and Aoki, T. Intracranial aneurysm as a macrophage-mediated inflammatory disease. *Neurologia medico-chirurgica 59*, 4 (2019), 126.

[297] Shimogonya, Y., Ishikawa, T., Imai, Y., Matsuki, N., and Yamaguchi, T. Can temporal fluctuation in spatial wall shear stress gradient initiate a cerebral aneurysm? a proposed novel hemodynamic index, the gradient oscillatory number (gon). *Journal of biomechanics 42*, 4 (2009), 550–554.

[298] Shimogonya, Y., Ishikawa, T., Imai, Y., Matsuki, N., and Yamaguchi, T. A realistic simulation of saccular cerebral aneurysm formation: focussing

on a novel haemodynamic index, the gradient oscillatory number. *International Journal of Computational Fluid Dynamics 23*, 8 (2009), 583–593.

[299] Shojima, M., Oshima, M., Takagi, K., Torii, R., Hayakawa, M., Katada, K., Morita, A., and Kirino, T. Magnitude and role of wall shear stress on cerebral aneurysm: computational fluid dynamic study of 20 middle cerebral artery aneurysms. *Stroke 35*, 11 (2004), 2500–2505.

[300] Si, H. Tetgen, a delaunay-based quality tetrahedral mesh generator. *ACM Trans. Math. Softw. 41*, 2 (Feb. 2015).

[301] Si, H., and Gärtner, K. 3d boundary recovery by constrained delaunay tetrahedralization. *International Journal for Numerical Methods in Engineering 85*, 11 (2011), 1341–1364.

[302] Signorelli, F., Sela, S., Gesualdo, L., Chevrel, S., Tollet, F., Pailler-Mattei, C., Tacconi, L., Turjman, F., Vacca, A., and Schul, D. B. Hemodynamic stress, inflammation, and intracranial aneurysm development and rupture: A systematic review. *World Neurosurgery 115* (2018), 234 – 244.

[303] Siogkas, P., Sakellarios, A., Exarchos, T., Stefanou, K., Fotiadis, D., Naka, K., Michalis, L., Filipovic, N., and Parodi, O. Blood flow in arterial segments: rigid vs. deformable walls simulations. *Journal of the Serbian Society for Computational Mechanics 5*, 1 (2011), 69–77.

[304] Siu, K. L., Li, Q., Zhang, Y., Guo, J., Youn, J. Y., Du, J., and Cai, H. Nox isoforms in the development of abdominal aortic aneurysm. *Redox biology 11* (2017), 118–125.

[305] Skodvin, T. Ø., Johnsen, L.-H., Gjertsen, Ø., Isaksen, J. G., and Sorteberg, A. Cerebral aneurysm morphology before and after rupture: nationwide case series of 29 aneurysms. *Stroke 48*, 4 (2017), 880–886.

[306] Smola, A. J., and Schölkopf, B. A tutorial on support vector regression. *Statistics and computing 14*, 3 (2004), 199–222.

[307] Soldozy, S., Norat, P., Elsarrag, M., Chatrath, A., Costello, J. S., Sokolowski, J. D., Tvrdik, P., Kalani, M. Y. S., and Park, M. S. The biophysical role of hemodynamics in the pathogenesis of cerebral aneurysm formation and rupture. *Neurosurgical focus 47*, 1 (2019), E11.

[308] Staarmann, B., Smith, M., and Prestigiacomo, C. J. Shear stress and aneurysms: a review. *Neurosurgical focus 47*, 1 (2019), E2.

[309] staff, B. Medical gallery of blausen medical 2014, 2014. File:Blausen 0055 ArteryWallStructure.png.

[310] Stanger, O. H., Pepper, J. R., and Svensson, L. G. *Surgical Management of Aortic Pathology: Current Fundamentals for the Clinical Management of Aortic Disease*. Springer, 2019.

[311] Starke, R. M., Raper, D. M., Ding, D., Chalouhi, N., Owens, G. K., Hasan, D. M., Medel, R., and Dumont, A. S. Tumor necrosis factor-α modulates cerebral aneurysm formation and rupture. *Translational stroke research 5*, 2 (2014), 269–277.

[312] Steiner, T., Juvela, S., Unterberg, A., Jung, C., Forsting, M., and Rinkel, G. European stroke organization guidelines for the management of intracranial aneurysms and subarachnoid haemorrhage. *Cerebrovascular diseases (Basel, Switzerland) 35* (02 2013), 93–112.

[313] Steinman, D. A. Image-based computational fluid dynamics modeling in realistic arterial geometries. *Annals of biomedical engineering 30*, 4 (2002), 483–497.

[314] Steinman, D. A., Milner, J. S., Norley, C. J., Lownie, S. P., and Holdsworth, D. W. Image-based computational simulation of flow dynamics in a giant intracranial aneurysm. *American Journal of Neuroradiology 24*, 4 (2003), 559–566.

[315] Sträter, A., Huber, A., Rudolph, J., Berndt, M., Rasper, M., Rummeny, E. J., and Nadjiri, J. 4d-flow mri: Technique and applications. In *RöFo-Fortschritte auf dem Gebiet der Röntgenstrahlen und der bildgebenden Verfahren* (2018), vol. 190, © Georg Thieme Verlag KG, pp. 1025–1035.

[316] Sujudi, D., and Haimes, R. Identification of swirling flow in 3-d vector fields. In *12th Computational Fluid Dynamics Conference* (1995), p. 1715.

[317] Sun, H. T., Sze, K. Y., Tang, A. Y. S., Tsang, A. C. O., Yu, A. C. H., and Chow, K. W. Effects of aspect ratio, wall thickness and hypertension in the patient-specific computational modeling of cerebral aneurysms using fluid-structure interaction analysis. *Engineering Applications of Computational Fluid Mechanics 13*, 1 (2019), 229–244.

[318] Sun, X., Fu, Y., Gu, M., Zhang, L., Li, D., Li, H., Chien, S., Shyy, J. Y.-J., and Zhu, Y. Activation of integrin $\alpha 5$ mediated by flow requires its translocation to membrane lipid rafts in vascular endothelial cells. *Proceedings of the National Academy of Sciences 113*, 3 (2016), 769–774.

[319] Sunderland, K., Haferman, C., Chintalapani, G., and Jiang, J. Vortex analysis of intra-aneurismal flow in cerebral aneurysms. *Computational and Mathematical Methods in Medicine 2016* (2016).

[320] Sunderland, K., Huang, Q., Strother, C., and Jiang, J. Two closely spaced aneurysms of the supraclinoid internal carotid artery: How does one influence the other? *Journal of biomechanical engineering 141*, 11 (2019).

[321] Sunderland, K., and Jiang, J. Multivariate analysis of hemodynamic parameters on intracranial aneurysm initiation of the internal carotid artery. *Medical engineering & physics 74* (2019), 129–136.

[322] Sunderland, K., Wang, M., Pandey, A., Gemmete, J., Huang, Q., Goudge, A., and Jiang, J. Quantitative analysis of flow vortices: differentiation of unruptured and ruptured medium-sized middle cerebral artery aneurysms. *Acta Neurochirurgica* (10 2020).

[323] Tat, J., Psaromiligkos, I. N., and Daskalopoulou, S. S. Carotid atherosclerotic plaque alters the direction of longitudinal motion in the artery wall. *Ultrasound in Medicine & Biology 42*, 9 (2016), 2114 – 2122.

[324] Texakalidis, P., Sweid, A., Mouchtouris, N., Peterson, E. C., Sioka, C., Rangel-Castilla, L., Reavey-Cantwell, J., and Jabbour, P. Aneurysm formation, growth, and rupture: The biology and physics of cerebral aneurysms. *World Neurosurgery 130* (2019), 277 – 284.

[325] Thenier-Villa, J. L., Rodríguez], A. R., Martínez-Rolán, R. M., Gelabert-González, M., González-Vargas, P. M., Campoverde], R. A. G., Molina], J. D., Zaragoza], A. D. L. L., Martínez-Cueto, P., Pou, J., and Alonso], C. C. Hemodynamic changes in the treatment of multiple intracranial aneurysms: A computational fluid dynamics study. *World Neurosurgery 118* (2018), e631 – e638.

[326] Theodotou, C. B., Snelling, B. M., Sur, S., Haussen, D. C., Peterson, E. C., and Elhammady, M. S. Genetic associations of intracranial

aneurysm formation and sub-arachnoid hemorrhage. *Asian journal of neurosurgery 12*, 3 (2017), 374.

[327] Thomas, A., Ou-Yang, H. D., Lowe-Krentz, L., Muzykantov, V. R., and Liu, Y. Biomimetic channel modeling local vascular dynamics of pro-inflammatory endothelial changes. *Biomicrofluidics 10*, 1 (2016), 014101.

[328] Thompson, G. B., Brown, R. D., Amin-Hanjani, S., Broderick, J. P., Cockroft, K. M., Connolly, E. S., Duckwiler, G. R., Harris, C. C., Howard, V. J., Johnston, S. C. C., and et. al. Guidelines for the management of patients with unruptured intracranial aneurysms: a guideline for healthcare professionals from the american heart association/american stroke association. *Stroke* (2015), STR–0000000000000070.

[329] Tibshirani, R. Regression shrinkage and selection via the lasso. *Journal of the Royal Statistical Society. Series B (Methodological)* (1996), 267–288.

[330] Tibshirani, R., Hastie, T., Narasimhan, B., and Chu, G. Diagnosis of multiple cancer types by shrunken centroids of gene expression. *Proceedings of the National Academy of Sciences 99*, 10 (2002), 6567–6572.

[331] Toczek, J., Meadows, J. L., and Sadeghi, M. M. Novel molecular imaging approaches to abdominal aortic aneurysm risk stratification. *Circulation: Cardiovascular Imaging 9*, 1 (2016), e003023.

[332] Tojkander, S., Gateva, G., and Lappalainen, P. Actin stress fibers – assembly, dynamics and biological roles. *Journal of Cell Science 125*, 8 (2012), 1855–1864.

[333] Tronic, F., Mallat, Z., Lehoux, S., Wassef, M., Esposito, B., and Tedgui, A. Role of matrix metalloproteinases in blood flow-induced arterial enlargement: interacdtion with no. *Arterioscler Thromb Vasc Biol 20*, 12 (2000), E120–E126.

[334] Tsuji, M., Ishikawa, T., Ishida, F., Furukawa, K., Miura, Y., Shiba, M., Sano, T., Tanemura, H., Umeda, Y., Shimosaka, S., et al. Stagnation and complex flow in ruptured cerebral aneurysms: a possible association with hemostatic pattern. *Journal of neurosurgery 126*, 5 (2017), 1566–1572.

[335] Tupin, S., Saqr, K. M., and Ohta, M. Effects of wall compliance on multiharmonic pulsatile flow in idealized cerebral aneurysm models: comparative piv experiments. *Experiments in Fluids 61*, 7 (2020), 1–11.

[336] Turjma, A. S., Turjman, F., and Edelman, E. R. Role of fluid dynamics and inflammation in intracranial aneurysm formation. *Circulation 129*, 3 (2014), 373–382.

[337] Tzima, E., Irani-Tehrani, M., Kiosses, W. B., Dejana, E., Schultz, D. A., Engelhardt, B., Cao, G., DeLisser, H., and Schwartz, M. A.

A mechanosensory complex that mediates the endothelial cell response to fluid shear stress. *Nature 437*, 7057 (2005), 426.

[338] Uchimido, R., Schmidt, E. P., and Shapiro, N. I. The glycocalyx: a novel diagnostic and therapeutic target in sepsis. *Critical Care 23*, 1 (2019), 16.

[339] uhana Frösen, Tulamo, R., Paetau, A., Laaksamo, E., Korja, M., Laakso, A., MikaNiemelä, and Hernesniemi, J. Saccular intracranial aneurysm: pathology and mechanisms. *Acta Neuropathologica 123*, 6 (Jun 2012), 773–786.

[340] Uzarski, J. S., Scott, E. W., and McFetridge, P. S. Adaptation of endothelial cells to physiologically-modeled, variable shear stress. *PloS one 8*, 2 (2013), e57004.

[341] Valen-Sendstad, K., and Steinman, D. Mind the gap: impact of computational fluid dynamics solution strategy on prediction of intracranial aneurysm hemodynamics and rupture status indicators. *American Journal of Neuroradiology* (2013).

[342] van der Meer, A. D., Poot, A. A., Feijen, J., and Vermes, I. Analyzing shear stress-induced alignment of actin filaments in endothelial cells with a microfluidic assay. *Biomicrofluidics 4*, 1 (2010), 011103.

[343] Vanhoutte, P. M., Shimokawa, H., Tang, E. H., and Feletou, M. Endothelial dysfunction and vascular disease. *Acta physiologica 196*, 2 (2009), 193–222.

[344] Vanrossomme, A., Eker, O. F., Thiran, J.-P., Courbebaisse, G., and Boudjeltia, K. Z. Intracranial aneurysms: Wall motion analysis for prediction of rupture. *American journal of neuroradiology 36*, 10 (2015), 1796–1802.

[345] Varble, N., Trylesinski, G., Xiang, J., Snyder, K., and Meng, H. Identification of vortex structures in a cohort of 204 intracranial aneurysms. *Journal of The Royal Society Interface 14*, 130 (2017), 20170021.

[346] Varble, N., Tutino, V., Yu, J., Sonig, A., Siddiqui, A., Davies, J., and Meng, H. Shared and distinct rupture disciminants of small and large intracranial. *Stroke 49* (2018), 856–864.

[347] Versteeg, H., and Malalasekera, W. *An introduction to computational fluid dynamics: the finite volume method*. Pearson, 2007.

[348] Villablanca, J. P., Duckwile, G. R., Jahan, R., Tateshima, S., Martin, N. A., Frazee, J., Gonzalez, N. R., Sayre, J., and Vinuela, F. V. Natural history of asymptomatic unruptured cerebral aneurysms evaluated at ct angiography: growth and rupture incidence and correlation with epidemiologic risk factors. *Radiology 269*, 1 (2013), 258–265.

[349] Vion, A.-C., Kheloufi, M., Hammoutene, A., Poisson, J., Lasselin, J., Devue, C., Pic, I., Dupont, N., Busse, J., Stark, K., et al. Autophagy is required for endothelial cell alignment and atheroprotection under physiological blood flow. *Proceedings of the National Academy of Sciences 114*, 41 (2017), E8675–E8684.

[350] Vlak, M. H., Algra, A., Brandenburg, R., and Rinkel, G. J. Prevalence of unruptured intracranial aneurysms, with emphasis on sex, age, comorbidity, country, and time period: a systematic review and meta-analysis. *The Lancet Neurology 10*, 7 (2011), 626–636.

[351] Vozzi, F., Campolo, J., Cozzi, L., Politano, G., Di Carlo, S., Rial, M., Domenici, C., and Parodi, O. Computing of low shear stress-driven endothelial gene network involved in early stages of atherosclerotic process. *BioMed research international 2018* (2018).

[352] Vu, H., Kotla, S., Ko, K., Fujii, Y., Tao, Y., Medina, J., Thomas, T., Hada, M., Sood, A., Singh, P., Milgrom, S., Krishnan, S., Fujiwara, K., Le, N.-T., and Abe, J. Ionizing radiation induces endothelial inflammation and apoptosis via p90rsk-mediated erk5 s496 phosphorylation. *Frontiers in Cardiovascular Medicine 5* (03 2018).

[353] Wang, C., Baker, B. M., Chen, C. S., and Schwartz, M. A. Endothelial cell sensing of flow directionsignificance. *Arteriosclerosis, thrombosis, and*

vascular biology 33, 9 (2013), 2130–2136.

[354] Wang, F., Xu, B., Sun, Z., Wu, C., and Zhang, X. Wall shear stress in intracranial aneurysms and adjacent arteries. *Neural regeneration research 8*, 11 (2013), 1007.

[355] Wang, G.-x., Wang, S., Liu, L.-l., Gong, M.-f., Zhang, D., Yang, C.-y., and Wen, L. A simple scoring model for prediction of rupture risk of anterior communicating artery aneurysms. *Frontiers in Neurology 10* (2019), 520.

[356] Wang, G.-x., Zhang, D., Wang, Z.-p., Yang, L.-q., Zhang, L., and Wen, L. Risk factors for the rupture of bifurcation intracranial aneurysms using ct angiography. *Yonsei Medical Journal 57*, 5 (2016), 1178–1184.

[357] Wang, L., Luo, J.-Y., Li, B., Tian, X. Y., Chen, L.-J., Huang, Y., Liu, J., Deng, D., Lau, C. W., Wan, S., et al. Integrin-yap/taz-jnk cascade mediates atheroprotective effect of unidirectional shear flow. *Nature 540*, 7634 (2016), 579–582.

[358] Wang, M., Monticone, R. E., and McGraw, K. R. Proinflammatory arterial stiffness syndrome: a signature of large arterial aging. *Journal of vascular research 55*, 4 (2018), 210–223.

[359] Wang, S., Dai, D., Parameswaran, P. K., Kadirvel, R., Ding, Y.-H., Robertson, A. M., and Kallmes, D. F. Rabbit aneurysm models mimic

histologic wall types identified in human intracranial aneurysms. *Journal of neurointerventional surgery 10*, 4 (2018), 411–415.

[360] Watton, P., Selimovic, A., Raberger, N. B., Huang, P., Holzapfel, G., and Ventikos, Y. Modelling evolution and the evolving mechanical environment of saccular cerebral aneurysms. *Biomechanics and modeling in mechanobiology 10*, 1 (2011), 109–132.

[361] Weir, B. Unruptured intracranial aneurysms: a review. *Journal of neurosurgery 96*, 1 (2002), 3–42.

[362] Weir, B., Disney, L., and Karrison, T. Sizes of ruptured and unruptured aneurysms in relation to their sites and the ages of patients. *Journal of neurosurgery 96*, 1 (2002), 64–70.

[363] Wen, J., Ding, G., Jiang, W., Wang, Q., and Zheng, T. Numerical simulation of compliant artery bypass grafts using fluid–structure interaction framework. *Asaio Journal 60*, 5 (2014), 533–540.

[364] Wermer, M. J., van der Schaaf, I. C., Algra, A., and Rinkel, G. J. Risk of rupture of unruptured intracranial aneurysms in relation to patient and aneurysm characteristics: an updated meta-analysis. *Stroke 38*, 4 (2007), 1404–1410.

[365] Wermer, M. J. H., van der Schaaf, I. C., Velthuis, B. K., Algra, A., Buskens, E., and Rinkel, G. J. E. Follow-up screening after subarachnoid

haemorrhage: frequency and determinants of new aneurysms and enlargement of existing aneurysms. *Brain 128*, 10 (2005), 2421–2429.

[366] Williams, L. N., and Brown, R. D. Management of unruptured intracranial aneurysms. *Neurology: Clinical Practice 3*, 2 (2013), 99–108.

[367] Wolf, F., Vogt, F., Schmitz-Rode, T., Jockenhoevel, S., and Mela, P. Bioengineered vascular constructs as living models for in vitro cardiovascular research. *Drug discovery today 21*, 9 (2016), 1446–1455.

[368] Wong, A. K., LLanos, P., Boroda, N., Rosenberg, S. R., and Rabbany, S. Y. A parallel-plate flow chamber for mechanical characterization of endothelial cells exposed to laminar shear stress. *Cellular and molecular bioengineering 9*, 1 (2016), 127–138.

[369] Xanthis, I., Souilhol, C., Serbanovic-Canic, J., Roddie, H., Kalli, A. C., Fragiadaki, M., Wong, R., Shah, D. R., Askari, J. A., Canham, L., et al. β1 integrin is a sensor of blood flow direction. *Journal of cell science 132*, 11 (2019), jcs229542.

[370] Xiang, J., Natarajan, S. K., Tremmel, M., Ma, D., Mocco, J., Hopkins, L. N., Siddiqui, A. H., Levy, E. I., and Meng, H. Hemodynamic–morphologic discriminants for intracranial aneurysm rupture. *Stroke 42*, 1 (2011), 144–152.

[371] Xiang, J., Natarajan, S. K., Tremmel, M., Ma, D., Mocco, J., Hopkins, L. N., Siddiqui, A. H., Levy, E. I., and Meng, H. Hemodynamic–morphologic discriminants for intracranial aneurysm rupture. *Stroke 42*, 1 (2011), 144–152.

[372] Xiang, J., Natarajan, S. K., Tremmel, M., Ma, D., Mocco, J., Hopkins, L. N., Siddiqui, A. H., Levy, E. I., and Meng, H. Hemodynamic–morphologic discriminants for intracranial aneurysm rupture. *Stroke 42*, 1 (2011), 144–152.

[373] Xiang, J., Siddiqui, A., and Meng, H. The effect of inlet waveforms on computational hemodynamics of patient-specific intracranial aneurysms. *Journal of biomechanics 47*, 16 (2014), 3882–3890.

[374] Xiang, J., Tutino, V., Snyder, K., and Meng, H. Cfd: Computational fluid dynamics or confounding factor dissemination? the role of hemodynamics in intracranial aneurysm rupture risk assessment. *American Journal of Neuroradiology 35*, 10 (2014), 1849–1857.

[375] Xiong, G., Figueroa, C. A., Xiao, N., and Taylor, C. A. Simulation of blood flow in deformable vessels using subject-specific geometry and spatially varying wall properties. *International journal for numerical methods in biomedical engineering 27*, 7 (2011), 1000–1016.

[376] Xu, L., Gu, L., and Liu, H. Exploring potential association between flow instability and rupture in patients with matched-pairs of ruptured–unruptured intracranial aneurysms. *Biomedical engineering online 15*, 2 (2016), 166.

[377] Xu, L., Lee, T.-Y., and Shen, H.-W. An information-theoretic framework for flow visualization. *IEEE Transactions on Visualization and Computer Graphics 16*, 6 (2010), 1216–1224.

[378] Yasuda, R., Strother, C. M., Taki, W., Shinki, K., Royalty, K., Pulfer, K., and Karmonik, C. Aneurysm volume-to-ostium area ratio: a parameter useful for discriminating the rupture status of intracranial aneurysms. *Neurosurgery 68*, 2 (2011), 310–318.

[379] Ye, G. J., Nesmith, A. P., and Parker, K. K. The role of mechanotransduction on vascular smooth muscle myocytes cytoskeleton and contractile function. *The Anatomical Record 297*, 9 (2014), 1758–1769.

[380] Yoo, W., Mayberry, R., Bae, S., Singh, K., He, Q. P., and Lillard Jr, J. W. A study of effects of multicollinearity in the multivariable analysis. *International journal of applied science and technology 4*, 5 (2014), 9.

[381] Yun, S., Budatha, M., Dahlman, J. E., Coon, B. G., Cameron, R. T., Langer, R., Anderson, D. G., Baillie, G., and Schwartz, M. A. Interaction between integrin α 5 and pde4d regulates endothelial inflammatory signalling. *Nature cell biology 18*, 10 (2016), 1043–1053.

[382] Zeng, Y. Endothelial glycocalyx as a critical signalling platform integrating the extracellular haemodynamic forces and chemical signalling. *Journal of cellular and molecular medicine 21*, 8 (2017), 1457–1462.

[383] Zeng, Z., Durka, M. J., Kallmes, D. F., Ding, Y., and Robertson, A. M. Can aspect ratio be used to categorize intra-aneurysmal hemodynamics?—a study of elastase induced aneurysms in rabbit. *Journal of biomechanics 44*, 16 (2011), 2809–2816.

[384] Zhang, X., Karuna, T., Yao, Z.-Q., Duan, C.-Z., Wang, X.-M., Jiang, S.-T., Li, X.-F., Yin, J.-H., He, X.-Y., Guo, S.-Q., Chen, Y.-C., Liu, W.-C., Li, R., and Fan, H.-Y. High wall shear stress beyond a certain range in the parent artery could predict the risk of anterior communicating artery aneurysm rupture at follow-up. *Journal of Neurosurgery JNS 131*, 3 (2018), 868 – 875.

[385] Zhang, Y., Jing, L., Liu, J., Li, C., Fan, J., Wang, S., Li, H., and Yang, X. Clinical, morphological, and hemodynamic independent characteristic factors for rupture of posterior communicating artery aneurysms. *Journal of neurointerventional surgery 8*, 8 (2016), 808–812.

[386] Zhang, Y., Jing, L., Zhang, Y., Liu, J., and Yang, X. Low wall shear stress is associated with the rupture of intracranial aneurysm with known rupture point: case report and literature review. *BMC Neurol 16* (2016).

[387] Zhang, Y., Takao, H., Murayama, Y., and Qian, Y. Propose a wall shear stress divergence to estimate the risks of intracranial aneurysm rupture. *The Scientific World Journal 2013* (2013).

[388] Zhang, Y., and Yang, W.-X. Tight junction between endothelial cells: the interaction between nanoparticles and blood vessels. *Beilstein journal of nanotechnology 7*, 1 (2016), 675–684.

[389] Zhao, F., and Ma, T. Perfusion bioreactor system for human mesenchymal stem cell tissue engineering: Dynamic cell seeding and construct development. *Biotechnology and Bioengineering 91*, 4 (2005), 482–493.

[390] Zhao, M., Amin-Hanjani, S., Ruland, S., Curcio, A., Ostergren, L., and Charbel, F. Regional cerebral blood flow using quantitative mr angiography. *American Journal of Neuroradiology 28*, 8 (2007), 1470–1473.

[391] Zhao, W., Zhang, H., and Su, J.-Y. Microrna-29a contributes to intracranial aneurysm by regulating the mitochondrial apoptotic pathway. *Molecular medicine reports 18*, 3 (2018), 2945–2954.

[392] Zhou, G., Zhu, Y., Yin, Y., Su, M., and Li, M. Association of wall shear stre ss with intracranial aneurysm rupture: Systematic review and meta-analysis. *Scientific Reports 7* (12 2017).

[393] Zhou, G., Zhu, Y., Yin, Y., Su, M., and Li, M. Association of wall shear stress with intracranial aneurysm rupture: systematic review and meta-analysis. *Scientific reports 7*, 1 (2017), 5331.

[394] Zou, H., and Hastie, T. Regularization and variable selection via the elastic net. *J.R. Statist. Soc. B* (2005), 301–320.

Appendix A

Statistics: Logistic Regression

In logistic regression, there exists an input-output dataset (X,Y) $\in XxY$ with an unknown probability distribution P. The goal is to find a function $f_n : X \rightarrow Y$, that is determined using a training set (X_1, Y_1,...,(X_n, Y_n) of n random pairs distributed as (X,Y). A desirable solution of f_n is one that, given a new data-point $x \in X$, the resultant $f_n(x)$ is an accurate prediction of the true output $y \in Y$. This desired outcome not only relies on the chosen function, but also of the selecting of relevant variables that are capable of achieving desired predictive accuracy. For models, it is often preferred to find the function that achieves the desired accuracy while using the minimal amount of variables required: i.e a *parsimonious* model. Brute-force methods of testing all variable combinations becomes increasingly unviable, especially when the number of variables in a dataset is larger than the number of n data points (cases) available for analysis. One type of methodology to determine a desired model is through the use of sparsity-based regularization methods [152, 329, 330, 394]

A.1 Multiple Logistic Regression

Multiple logistic regression (MLR) analysis looks both to estimate the odds of a dichotomous outcome occurring, and to determine the impact of an individual variable (covariate) in relation to the other covariates in a model. The probability of an outcome occurring in MLR can be calculated as such:

$$\hat{p} = \frac{exp(b_0 + b_1X_1 + b_2X_2 + ... + b_pX_p)}{1 + exp(b_0 + b_1X_1 + b_2X_2 + ... + b_pX_p)} \tag{A.1}$$

$\hat{p}$ being the probability of the desired outcome, X_1 through X_p as the individual dependent variables applied to the model, and b_1 to b_p being each variable's (respective) regression coefficients. To determine the expected log odds ratios of the model's variables, the *logit* function of the above equation can be calculated:

$$\begin{aligned} logit[\hat{p}] &= ln[\frac{\hat{p}}{1-\hat{p}}] \\ &= ln\left[\frac{\frac{exp(b_0+b_1X_1+b_2X_2+...+b_pX_p)}{1+exp(b_0+b_1X_1+b_2X_2+...+b_pX_p)}}{1-\frac{exp(b_0+b_1X_1+b_2X_2+...+b_pX_p)}{1+exp(b_0+b_1X_1+b_2X_2+...+b_pX_p)}}\right] \\ &= ln\left[\frac{\frac{exp(b_0+b_1X_1+b_2X_2+...+b_pX_p}{1+exp(b_0+b_1X_1+b_2X_2+...+b_pX_p}}{\frac{1}{1+exp(b_0+b_1X_1+b_2X_2+...+b_pX_p}}\right] \\ &= ln[exp(b_0 + b_1X_1 + b_2X_2 + ... + b_pX_p] \\ &= b_0 + b_1X_1 + b_2X_2 + ... + b_pX_p \end{aligned} \tag{A.2}$$

Taking the *logit* of the desired outcome's probability, transforms the occurrence of the event given Xs into a simplified linear function.

For each variable added to a regression model, the resultant R^2 (coefficient of multiple determination) may increase, indicating an improved fit of the data. However applying a large number of variables to a predictive model may result in over-fitting without a significantly large dataset: large p, small n paradigm. In such an event, the R^2 values, regression coefficients, and any statistical significance (p-values) determined may be misleading. To reduce the initial choices of variables in assessed predictive models, the correlation between variables are determined by:

$$r_{jk} = \frac{s_{jk}}{s_j s_k} = \frac{\sum_{i=1}^{n}(x_{ij} - \overline{x}_j)(x_{ik} - \overline{x}_k)}{\sqrt{\sum_{i=1}^{n}(x_{ij} - \overline{x}_j)^2}\sqrt{\sum_{i=1}^{n}(x_{ik} - \overline{x}_k)^2}} \tag{A.3}$$

with r as the Pearson correlation coefficient between variables x_j and x_k, n as the sample size, and $\overline{x}$ is a variable sample mean. Correlations between the variables are often displayed via a correlation table:

$$R = \begin{bmatrix} 1 & r_{12} & r_{13} & \dots & r_{1p} \\ r_{21} & 1 & r_{23} & \dots & r_{2p} \\ r_3 1 & r_{32} & 1 & \dots & r_{3p} \\ \vdots & \vdots & \vdots & \ddots & \dots \\ r_{p1} & r_{p2} & r_{p3} & \dots & 1 \end{bmatrix}$$

Initial correlation analysis of all available variables is performed to eliminate highly correlated variables from analysis: i.e aneurysm volume and surface area are highly correlated so surface area could be removed from analysis.

From the remaining variables, stepwise MLR determines the parsimonious model. In stepwise regression, linear regression is first performed for each variable one at a time, and the variable with the highest R^2 is kept for the model. Next, a multiple regression step is performed with the kept variable and each remaining variable. The variable with the largest increase in R_2, if the p value of the R^2 is below a desired cuttoff (<0.05), is added to the model. The calculation of the p value of an increase in R^2 resulting from the increasing of X variable(s) from a to b is as follows:

$$p_{ab} = \frac{(R_b^2 - R_a^2)/(b-a)}{(1-R_b^2)/(n-b-1)} \tag{A.4}$$

with the total sample size n.

Each time a new variable is added to the model, the impact of removing any of the other variables (already added to the model) on outcomes is tested. The chosen (removed) variable is excluded from the model if it does not make R^2 significantly worse. This process is continued till adding any new variables does not increase R^2 and removing any variable does not significantly decrease R^2

In the event that all of the independent variables in the model are completely uncorrelated with each other, the interpretation of coefficients are as such:

$$OR = exp(b_1)^z \tag{A.5}$$

Where z is the number of unit changes for a variable X, and OR is the odds ratio

resultant from said change. When the variables are not uncorrelated, the $OR = exp^z b_1$ is expressed as the change of unit z for a variable *adjusted in relation to the impacts of the other variables in the model.* This stresses the need to assess collinearity between variables prior to model assessment.

A.1.1 Reciever Operator Characterisitics

To assess the diagnostic ability of predictive model(s), a receiver operating characteristic curve (ROC) is deployed [134]. To determine the overall predictive strength of a model, a ROC curve assesses a model's predictive true positive rate (TPR) against its false positive rate (FPR) (Equation A.6) as a discrimination threshold is varied as a means to determine overall predictive strength.

$$\begin{aligned} TPR &= \frac{\Sigma TruePositive}{\Sigma ConditionPositive} \\ FPR &= \frac{\Sigma FalsePositive}{\Sigma ConditionNegative} \\ FNR &= \frac{\Sigma FalseNegative}{\Sigma ConditionPositive} \\ Specificity &= \frac{\Sigma TrueNegative}{\Sigma ConditionNegative} \end{aligned} \tag{A.6}$$

When dealing with a binary classification, the predictive test measure for each instance is denoted by a continuous random variable (x). Given a desired threshold (T), each instance is positive if x>T and negative if x<T. Setting the probability distribution functions of the positive and negative values of x to $f_p(x)$ and $f_n(x)$ respectively.

$$TPR(T) = \int_{T}^{\infty} f_p(x)dx \tag{A.7}$$

and the FNR as:

$$FPR(T) = 1 - \int_{T}^{\infty} f_n(x)dx \tag{A.8}$$

The ROC curve is generated by plotting TPR(T) against FPR(T) parametrically, varying across T, or as a plot of:

$$ROC(T) = 1 - f_p(f_n^{-1}(1-T)) \tag{A.9}$$

over T from [0,1] where $f_p$$^{-1}$(1-T) = inf

Comparing the resultant ROC curves provides the selection of the desired model based off of varying predictive accuracy. To quantify the predictive accuracy, the area under the curve (AUC) of the ROC curve is calculated, as it equals the probability of a classifier ranking a positive instance higher than a negative instance (both chosen at random).

$$\begin{aligned} A &= \int_{\infty}^{-\infty} TPR(T)FPR'(T)dT \\ &= \int_{-\infty}^{\infty}\int_{-\infty}^{\infty} I(T' > T)f_1(T')f_0(T)dT'dT = P(X_1 > X_0) \end{aligned} \tag{A.10}$$

The initial integral has reversed boundaries due to larger T values having a lower value on the x-axis.

Appendix B

Statistics: Support Vector Machine

Support-vector machine (SVM) is a supervised machine learning method utilizing algorithms to analyze classification data for regression analysis.

Formally, a given training dataset has the following condition:

$$(x_1, y_1), ..., (x_n, y_n), \vec{x_i} \in R^d and y_i \in (-1, +1) \tag{B.1}$$

where $\vec{x_i}$ and y_i are a (feature) vector representing prediction parameters and a class label (i.e. unruptured[-1] vs. ruptured[1]) for the i_th case. The goal of SVM is to decide which class a given data point should be in by viewing a data point as a dimensional vector, and if such points can be separated with a (p-1)-dimensional hyperplane. The hyperplane can be written as the set of points $\vec{x}$, with $\vec{w} \cdot \vec{x} - b = 0$, where $\vec{w}$ is the normal vector to the hyperplane and $\frac{b}{||\vec{w}||}$ is the offset of the hyperplane from the origin along $\vec{w}$. Optimization of the hyperplane is obtained by finding the

minimum of:

$$\phi(w) = \frac{1}{2}||w^2||subject y_i(w \cdot x_i + b) \geq 1, \forall(x_i, y_i) \tag{B.2}$$

The $y_i(w \cdot x_i + b) \geq 1$ constraint means the predicted outcome isolated by the hyperplane is on the same side with the known rupture status.

The mapping of non-linear data to a hyperplane is done via a kernel function, defining an inner product in higher dimensional space:

$$f(x) = sgn(\sum_{i=1}^{N_s} a_i y_i K(\vec{x_i}, \vec{x}) + b) \tag{B.3}$$

The kernel function allows the calculation of the scalar product between data points in high dimensional space without the need for directly calculating the mapping from the input space to higher-dimensional space. A kernel function is valid if there is a feature mapping ϕ in which:

$$K(\vec{x_i}, \vec{x_j}) = \phi(\vec{x_i} \cdot \vec{x_j}) \tag{B.4}$$

B.0.1 SVM Kernel Selection

Four popular kernels are often used in the training of models and prediction outcomes: linear, polynomial, radial basis, and sigmoid. These four kernels were tested to assess their impact on model accuracy (for this work). Fig.B.1 shows the performance

outcome of models (resultant AUC values) for each kernel. Each test was performed using all available variables and 10-fold cross-validation was performed to determine the idea gamma and cost value for each function. Of the tested functions, the radial basis function kernel resulted in the strongest outcomes. The radial basis function is calculated as:

$$K_{RBF}(x, y, z) = exp(-\gamma||x - y||^2) : \gamma = \frac{1}{2\sigma} \tag{B.5}$$

With $||x - y||^2$ as the squared Euclidean distance between two feature vectors. A low γ results in a low decision boundary (for the hyperplane) creating broad decision regions. The cost parameter of SVM acts as a penalty for data point misclassification: a small cost weakens the impact of misclassified data (high bias, low variance) whereas a large cost results in a low bias, high variance in decision parameters.

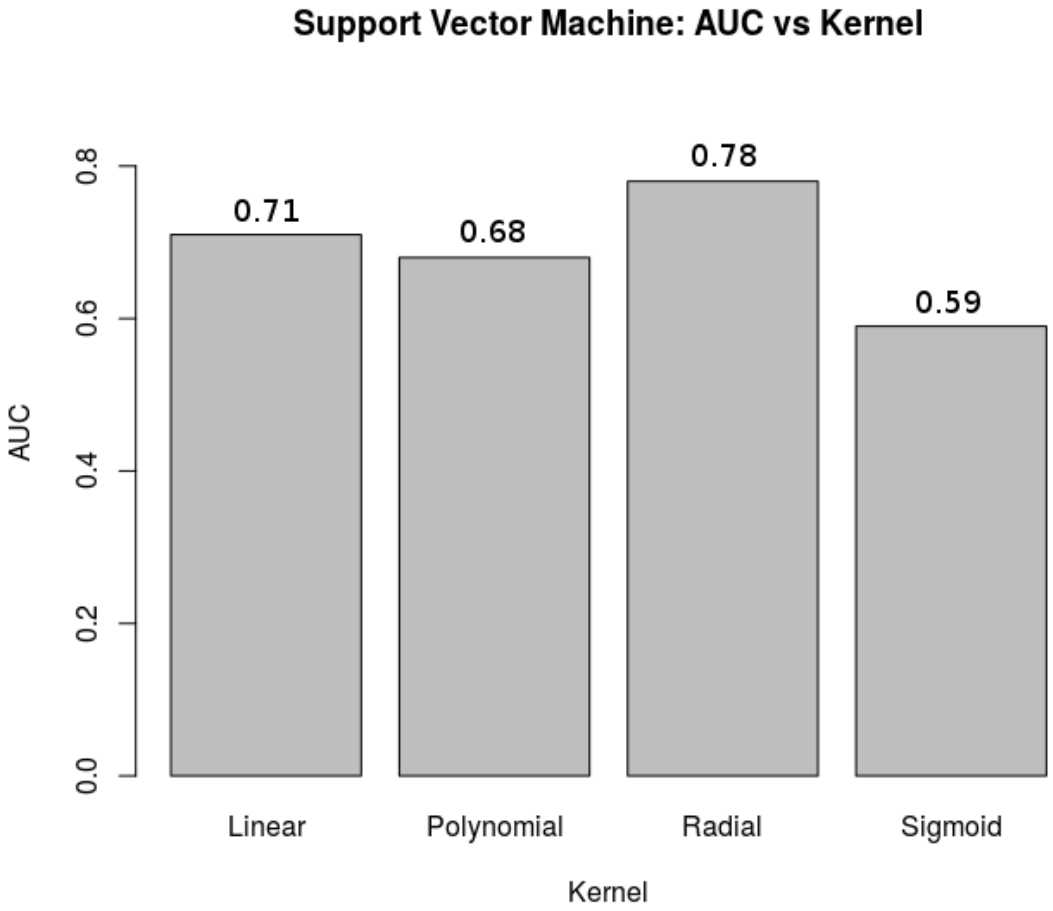

Figure B.1: Outcome of predictive model (using the geometric+WSS+vortex model) generated under varying SVM kernels: linear, polynomial, radial basis function, and sigmoid. Cross-validation determined ideal gamma and cost values for models. The AUC for each kernel was: 0.71, 0.68, 0.78 and 0.59 respectively.

Appendix C

Documentation of Copyright Permissions

C.1 Permission for Chapter 2

C.2 Permission for Chapter 3

Taken from Rightslink Copyright Clearance Center `https://s100.copyright.com/AppDispatchServlet?publisherName=ELS&contentID=S1350453319301766&`

orderBeanReset=true:

”Please note that, as the author of this Elsevier article, you retain the right to include it in a thesis or dissertation, provided it is not published commercially. Permission is not required, but please ensure that you reference the journal as the original source. For more information on this and on your other retained rights, please visit: https://www.elsevier.com/about/our-business/policies/copyright#Author-rights"

C.3 Permission for Chapter 4

COPYRIGHT AGREEMENT (as of February 2010)

ASME Publishing • Two Park Avenue • New York, NY 10016
For questions about Conference paper copyright, please e-mail copyright@asme.org
For questions about Journal paper copyright, please email journalcopyright@asme.org

Before publication of your paper in a conference proceedings or journal, ASME must receive a signed Copyright Agreement. For conference papers, this form should be received by the deadline indicated by the Conference. Other forms may NOT be substituted for this form, nor may any wording on the form be changed.

PAPER NUMBER (for conference/journal papers): BIO-17-1393

TITLE: Two closely-spaced Aneurysms of the Supraclinoid Internal Carotid Artery: How Does One Influence the Other?

AUTHOR(s): Kevin Sunderland

CONFERENCE NAME:

JOURNAL NAME: Journal of Biomechanical Engineering

ASME requests that authors/copyright owners assign copyright to ASME in order for a conference or journal paper to be published by ASME. Authors exempt from this request are direct employees of the U.S. Government, whereby papers are not subject to copyright protection in the U.S., or non-U.S. government employees, whose governments hold the copyright to the paper. Otherwise, the author/ copyright owner(s) of the Paper should sign this form as instructed below. Please refer to the section below "Who Should Sign" and also to ASME's FAQ page for more information regarding copyright ownership and the copyright process.

WHO SHOULD SIGN

Only the copyright owner(s) of the Paper, or an authorized representative, can sign this form. If one of the following applies, you may not own the copyright to the paper, or you may not be authorized to sign this agreement, and you may need to have the appropriate copyright owner(s) or organization representative sign this Agreement:
(1) You created the Paper within the scope of your employment, and your employer is the copyright owner
(2) You created the Paper under an independent contractor agreement**
(3) You received a grant that funded your Paper.

Please review your company policies regarding copyright, and if you are not authorized to sign this agreement, please forward to the appropriate organization representative. Please review applicable company, institutional, and grant policies and your employment/independent contractor agreement to determine who holds the rights to your Paper. For more information, please refer to the FAQs.

****Note to U.S. Government Contractors:** If you created the Paper under contract with the U.S. Government, e.g., U.S. Government labs, the paper may be subject to copyright, and you or your employer may own the copyright. Please review your company/institutional policies and your contractor agreement. Your Paper may also require a footer acknowledging contract information and also the following statement:

"The United States Government retains, and by accepting the article for publication, the publisher acknowledges that the United States Government retains, a non-exclusive, paid-up, irrevocable, worldwide license to publish or reproduce the published form of this work, or allow others to do so, for United States Government purposes."

It is your responsibility to ensure that the final PDF version of the Paper you submit includes all necessary footers and statements required under your contract.

COPYRIGHT ASSIGNMENT

The following terms of copyright assignment refer to Sections 1, 2, and 3. Sections 4 and 5 may not be subject to copyright.

The undersigned hereby assigns irrevocably to ASME all worldwide rights under copyright in the Paper.

Authors retain all proprietary rights in any idea, process, procedure, or articles of manufacture described in the Paper, including the right to seek patent protection for them. Authors may perform, lecture, teach, conduct related research, display all

or part of the Paper, and create derivative works in print or electronic format. Authors may reproduce and distribute the Paper for non-commercial purposes only. Non-commercial applies only to the sale of the paper per se. For all copies of the Paper made by Authors, Authors must acknowledge ASME as original publisher and include the names of all author(s), the publication title, and an appropriate copyright notice that identifies ASME as the copyright holder.

PLEASE READ THE TERMS AND CONDITIONS WHICH ARE FULLY INCORPORATED IN THIS AGREEMENT.

PAPERS OWNED BY ONE AUTHOR OR JOINT AUTHORS; DESIGNATED AUTHORS (For jointly authored works, all authors should submit a signed Agreement, or one Designated Author may sign on behalf of the other authors, but ONLY IF the designated author has secured written authorization to do so from all other authors. The designated author must be able to produce such written authorization if requested.)

Author, Co-Author, or Designated Author

Name: Kevin Sunderland Signature: Kevin Sunderland Date: 10 Sep 2017

Affiliation: Michigan Technological University (Company or Institution) Title: Graduate Student

Street Address: 309 M&M, 1400 Townsend Drive Dept. of Biomedical Engineering

Houghton (City) MI (State) 49931 (Zip Code) United States (Country)

Phone: 9064877272 Fax: Email: kwsunder@mtu.edu

Author: (Applied only if you are signing for other)

Name: Signature: Date:

Affiliation: (Company or Institution) Title:

Street Address:

(City) (State) (Zip Code) (Country)

Phone: Fax: Email:

ASME COPYRIGHT FORM TERMS AND CONDITIONS

The following terms and conditions are fully incorporated into the Copyright Form. Please read them carefully.

REPRESENTATIONS, OBLIGATIONS, ACKNOWLEDGEMENTS, AND INDEMNIFICATION

You represent and acknowledge that:

(A) This Paper represents: either the first publication of material or the first publication of an original compilation of information from a number of sources as specifically noted by footnotes and/or bibliography.

(B) You have the right to enter into this Copyright Form and to make the assignment of rights to ASME. If the Paper contains excerpts from other copyrighted material (including without limitation any diagrams, photographs, figures or text), you have acquired in writing all necessary rights from third parties to include those materials in the Paper, and have provided appropriate credit for that third-party material in footnotes or in a bibliography.

(C) If you are signing this Form on behalf of any co-authors or other copyright holders, you have obtained express authorizations from all those authors and/or copyright holders to make this assignment of rights to ASME.

(D) To the best of the author's knowledge, all statements contained in the Paper purporting to be facts are true or supported by reasonable scientific research, the Paper does not contain any defamatory or libelous material and does not infringe any third party's copyright, patent, trade secret, or other proprietary rights and does not violate the right of privacy or publicity of any third party or otherwise violate any other applicable law; furthermore that to the best of your ability, you are responsible for ensuring the accuracy of your research and the Paper's content.

(E) If the Paper was produced in the course of an author's employment by, or contractual relationship with, the U.S. Federal or State Government and/or contains classified material, it has been appropriately cleared for public release and such is indicated in the paper.

(F) The Paper is not subject to any prior claim, encumbrance or form and is not under consideration for publication elsewhere.

(G) You have appropriately cited and acknowledged all third parties who have contributed significantly in the Paper's technical aspects.

(H) ASME is not responsible for any misrepresentation, errors or omissions by those signing this copyright form.

(I) All print and electronic copies of the Paper submitted to ASME become ASME's physical property regardless of whether or not ASME publishes the Paper, and that ASME is not obligated to publish your paper (see the Termination Section below if your paper is not published).

(J) ASME is not responsible for any of your expenses incurred in connection with preparing the Paper or attending meetings to present it, nor will ASME pay you any financial compensation if it publishes your Paper.

(K) Subject to and to the maximum extent permitted by law, you agree to indemnify and hold harmless ASME from any damage or expense related to a breach of any of the representations and warranties above.

TERMINATION

If ASME decides not to publish your Paper, this Form, including all of ASME's rights in your Paper, terminates and you are thereafter free to offer the Paper for publication elsewhere.

GENERAL PROVISIONS

This Copyright Form, the Terms & Conditions, and ASME Copyright Guidelines, constitutes the entire agreement between you and ASME, and supersedes all prior or current negotiations, understandings and representations, whether oral or written, between you and ASME concerning the Paper.

This Agreement is governed by, and should be construed in accordance with, the laws of the State of New York, United States of America, applicable to agreements made and performed there, except to the extent that your institution is prohibited by law from entering contracts governed by New York law, in which limited case this Agreement is governed by, and should be construed in accordance with, the laws of the jurisdiction in which your institution is located. Any claim, dispute, action or proceeding relating to this Agreement may be brought only in the applicable state and federal courts in the State and County of New York, and you expressly consent to personal jurisdiction and venue in any of those courts.

C.4 Permission for Chapter 5

Michigan Tech

Kevin Sunderland <kwsunder@mtu.edu>

Fwd: Copyright Transfer Statement (CTS) for your article in Acta Neurochirurgica (4616)

2 messages

Jingfeng Jiang <jjiang1@mtu.edu> Fri, Oct 9, 2020 at 3:03 PM
To: Kevin Sunderland <kwsunder@mtu.edu>

I think you need that for your dissertation so please keep it.
--JJ

---------- Forwarded message ---------
From: **Springer** <springerauthorquery@springeronline.com>
Date: Fri, Oct 9, 2020 at 2:58 PM
Subject: Copyright Transfer Statement (CTS) for your article in Acta Neurochirurgica (4616)
To: <jjiang1@mtu.edu>

Springer

Copyright Transfer 09.10.2020

visit us at springer.com

Confirmation of your Copyright Transfer

Dear Author,

Please note: This e-mail is a confirmation of your copyright transfer and was sent to you only for your own records.

1. Publication
The copyright to this article, (including any supplementary information and graphic elements therein (e.g. illustrations, charts, moving images) (the 'Article'), is hereby assigned for good and valuable consideration to Springer-Verlag GmbH Austria, part of Springer Nature (the 'Assignee'). Headings are for convenience only.

2. Grant of Rights
In consideration of the Assignee evaluating the Article for publication, the Author(s) grant the Assignee without limitation the exclusive (except as set out in clauses 3, 4 and 5 a) iv), assignable and sub-licensable right, unlimited in time and territory, to copy-edit, reproduce, publish, distribute, transmit, make available and store the Article, including abstracts thereof, in all forms of media of expression now known or developed in the future, including pre- and reprints, translations, photographic reproductions and extensions. Furthermore, to enable additional publishing services, such as promotion of the Article, the Author(s) grant the Assignee the right to use the Article (including the use of any graphic elements on a stand-alone basis) in whole or in part in electronic form, such as for display in databases or data networks (e.g. the Internet), or for print or download

to stationary or portable devices. This includes interactive and multimedia use as well as posting the Article in full or in part or its abstract on social media, and the right to alter the Article to the extent necessary for such use. The Assignee may also let third parties share the Article in full or in part or its abstract on social media and may in this context sub-license the Article and its abstract to social media users. Author(s) grant to Assignee the right to re-license Article metadata without restriction (including but not limited to author name, title, abstract, citation, references, keywords and any additional information as determined by Assignee).

3. Self-Archiving
Author(s) are permitted to self-archive a pre-print and an Author's accepted manuscript version of their Article.

a. A pre-print is the Author's version of the Article before peer-review has taken place ("Pre-Print"). Prior to acceptance for publication, Author(s) retain the right to make a Pre-Print of their Article available on any of the following: their own personal, self-maintained website; a legally compliant pre-print server such as but not limited to arXiv and bioRxiv. Once the Article has been published, the Author(s) should update the acknowledgement and provide a link to the definitive version on the publisher's website: "This is a pre-print of an article published in [insert journal title]. The final authenticated version is available online at: https://doi.org/[insert DOI]".
b. An Author's Accepted Manuscript (AAM) is the version accepted for publication in a journal following peer review but prior to copyediting and typesetting that can be made available under the following conditions:
    a. Author(s) retain the right to make an AAM of their Article available on their own personal, self-maintained website immediately on acceptance,
    b. Author(s) retain the right to make an AAM of their Article available for public release on any of the following 12 months after first publication ("Embargo Period"): their employer's internal website; their institutional and/or funder repositories. AAMs may also be deposited in such repositories immediately on acceptance, provided that they are not made publicly available until after the Embargo Period.

An acknowledgement in the following form should be included, together with a link to the published version on the publisher's website: "This is a post-peer-review, pre-copyedit version of an article published in [insert journal title]. The final authenticated version is available online at: http://dx.doi.org/[insert DOI]".

4. Authors' Retained Rights
Author(s) retain the following non-exclusive rights for the published version provided that, when reproducing the Article or extracts from it, the Author(s) acknowledge and reference first publication in the Journal:

a. to reuse graphic elements created by the Author(s) and contained in the Article, in presentations and other works created by them;
b. they and any academic institution where they work at the time may reproduce the Article for the purpose of course teaching (but not for inclusion in course pack material for onward sale by libraries and institutions); and
c. to reproduce, or to allow a third party Licensee to reproduce the Article in whole or in part in any printed volume (book or thesis) written by the Author(s).
d. To reproduce, or to allow a third party Licensee to reproduce the Article, in whole or in part, in any other type of work (other than thesis) written by the Author(s) for distribution by a publisher after an embargo period of 12 months.

5. Warranties
The Author(s) warrant and represent that:

a. (i) the Author(s) are the sole copyright owners or have been authorised by any additional copyright owner(s) to grant the rights defined in clause 2, (ii) the Article does not infringe any intellectual property rights (including without limitation copyright, database rights or trade mark rights) or other third party rights and no licence from or payments to a third party are required to publish the Article, (iii) the Article has not been previously published or licensed, (iv) if the Article contains materials from other sources (e.g. illustrations, tables, text quotations), Author(s) have obtained written permissions to the extent necessary from the copyright holder(s), to license to the Assignee the same rights as set out in clause 2 but on a non-exclusive basis and without the right to use any graphic elements on a stand-alone basis and have cited any such materials correctly;

b. all of the facts contained in the Article are according to the current body of science true and accurate;
c. nothing in the Article is obscene, defamatory, violates any right of privacy or publicity, infringes any other human, personal or other rights of any person or entity or is otherwise unlawful and that informed consent to publish has been obtained for all research participants;
d. nothing in the Article infringes any duty of confidentiality which any of the Author(s) might owe to anyone else or violates any contract, express or implied, of any of the Author(s). All of the institutions in which work recorded in the Article was created or carried out have authorised and approved such research and publication; and
e. the signatory (the Author or the employer) who has signed this agreement has full right, power and authority to enter into this agreement on behalf of all of the Author(s).

6. Cooperation
The Author(s) shall cooperate fully with the Assignee in relation to any legal action that might arise from the publication of the Article, and the Author(s) shall give the Assignee access at reasonable times to any relevant accounts, documents and records within the power or control of the Author(s). The Author(s) agree that the distributing entity is intended to have the benefit of and shall have the right to enforce the terms of this agreement.

7. Author List
After signing, changes of authorship or the order of the authors listed will not be accepted unless formally approved in writing by the Assignee.

8. Edits & Corrections
The Author(s) agree(s) that the Assignee may retract the Article or publish a correction or other notice in relation to the Article if the Assignee considers in its reasonable opinion that such actions are appropriate from a legal, editorial or research integrity perspective.

This is an automated e-mail; please do not reply to this account. If you have any questions, please go to our help pages.

Thank you very much.

Kind regards,

Springer Author Services

Article Details

Journal title	Article title
Acta Neurochirurgica	Quantitative Analysis of Flow Vortices: Differentiation of Unruptured and Ruptured Medium-sized Middle Cerebral Aneurysms
DOI	**Corresponding Author**
10.1007/s00701-020-04616-y	Jingfeng Jiang
Copyright transferred to	**Transferred on**
Springer-Verlag GmbH Austria, part of Springer Nature	Fri Oct 09 20:56:06 CEST 2020

Service Contacts

Springer Nature Customer Service Center

Tiergartenstr. 15-17
69121 Heidelberg
Germany
phone: +49 6221 345 0
fax: +49 6221 345 4229
customerservice@springernature.com

Springer New York, LCC

233 Spring Street
New York, NY 10013
USA
phone: +1 212 460 1500 or 800-SPRINGER
(Weekdays 8:30am - 5:30pm ET)
fax: +1 212-460-1700
customerservice@springernature.com

--
++
Jingfeng Jiang, PhD
Department of Biomedical Engineering
Michigan Tech University
Phone: 906-487-1943
Email: jjiang1@mtu.edu
++

Kevin Sunderland <kwsunder@mtu.edu> Fri, Oct 9, 2020 at 4:04 PM
To: Jingfeng Jiang <jjiang1@mtu.edu>

Yes I will. Thank you
[Quoted text hidden]
--
Kevin Sunderland, BS.
Graduate Student (PhD)
Department of Biomedical Engineering
Michigan Technological University

phone: 706-830-6854
email: kwsunder@mtu.edu